FMPoNe: Forward Model radiative transfer for Polarization Nephelometer: In low flux density planetary atmosphere

Master Thesis

Sukanth Kumar Karapakula Jaganath Rao 4514009

Technische Universiteit Delft

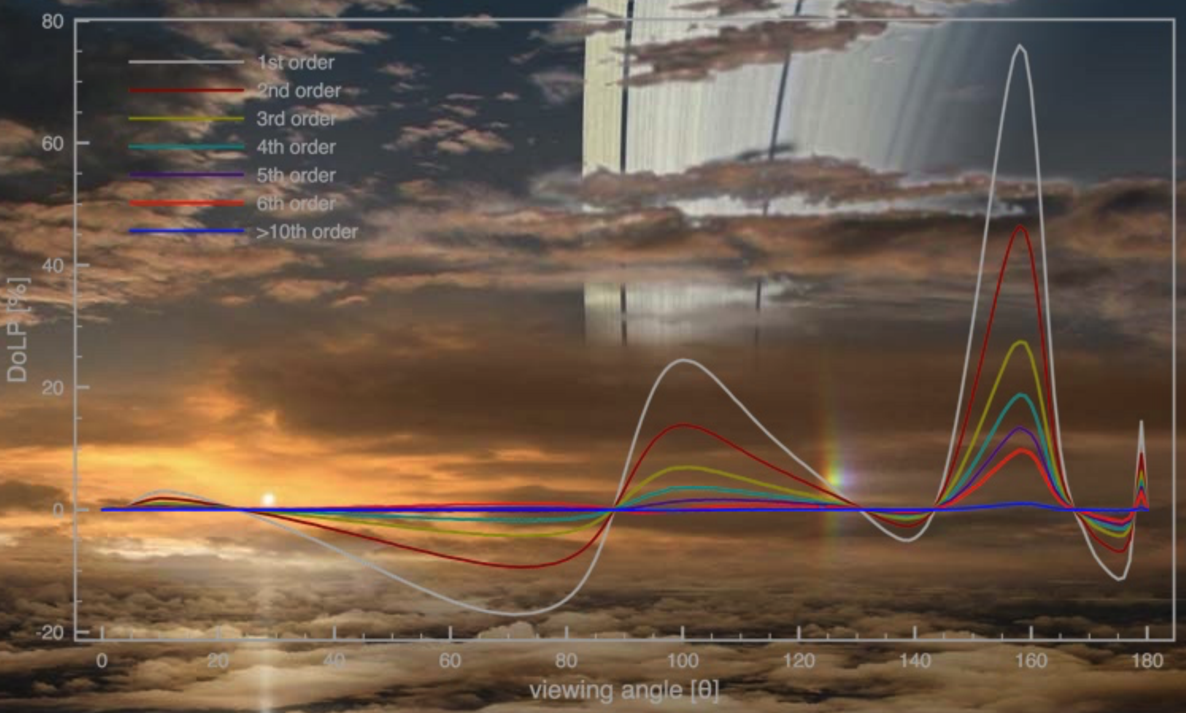

(c) Ron Miller

TU Delft
Delft
University of
Technology

Challenge the future

FMPoNe

Forward Model radiative transfer for Polarization Nephelometer: In low flux density planetary atmosphere

by

Sukanth Kumar Karapakula Jaganath Rao

to obtain the degree of Master of Science
at the Delft University of Technology,
to be defended publicly on Thursday March 29, 2018 at 09:30 AM.

Student number:	4514009	
Project duration:	Feb 1, 2017 – March 29, 2018	
Thesis committee:	Dr. D. M. Stam,	TU Delft, 1st supervisor
	Dr. Ir. J. M. Kuiper	TU Delft, 2nd supervisor
	Ir. B. T. C. Zandbergen	TU Delft

TU Delft

Acknowledgment

Sukanth Kumar Karapakula Jaganath Rao
Delft, March 2018

It is a genuine pleasure to write down my accelerating taught as my master thesis comes to an end. My journey as a master student at TU Delft was filled by varied experiences, sometimes the experience was filled with an adrenaline rush like a free fall in the sky, while at times it felt like a smooth glide in the air with a parachute on the back. The spaceflight masters have aided me to improve my skill sets on space systems, and also has motivated me further and has developed an eccentric interest towards astronomical instrumentation. It is only during my masters that I have enjoyed studying course, not every course but most of the courses were intriguingly accelerating for the mind and I have gained extensive knowledge on new topics that lead to the current research work.

The astronomical instrumentation had kept me captivated and hungry for more, which led me to take up a thesis topic that combined a part of science and engineering. The planetary sciences I and II courses fed this hunger on the science part of my quest, during these courses is where I was extensively introduced to the staggering experience and research conducted by Dr. Daphne Stam on exoplanets and did a short project report on understanding the asteroids orbits better with the aid of polarization property of light. The space instrumentation course on the other had quenched my thirst with engineering. With this motivation, I decided to a master thesis with Dr. Daphne on a polarization nephelometer for Saturn's atmosphere. The master thesis is the one I have enjoyed the most during my masters at TU Delft. I have congregated very good knowledge on radiative transfer and atmosphere modeling. I am able to realize the limitation on the science and as well the engineering part in space exploration. With the current thesis work, I have come to realize that I want to explore further with my career in an astronomical observation topic.

I would like to express my heartfelt thanks and gratitude to Dr. Daphne Stam my direct and daily supervisor. She has guided me with a pleasant heart and helped me through the atmosphere modeling. She gave me enough freedom and responsibilities to successfully complete the master thesis, and at the same time develop a forward model that could be used for any planetary atmosphere. I also would like to thank Vidhya Pallichadath for helping me with at times on instrumentation. I appreciate the discussion we had on system engineering and in general. I also express my extensive gratitude for Dr. Hans Kuiper, for space instrumentation course, and guiding me on engineering part of the thesis to develop and analyze the system characteristics for a preliminary study of the new measurement technique. Thanks to each of them again, I have stayed motivated in my thesis research and enjoyed during the complete project work.

It is my privilege to thank my parents for motivating me and stimulating me emotionally to cope with the stress that I personally had and overcome it, and helped me learn to enjoy my work. I especially like to thank my sister for believing in me and shaping me to realize my capabilities, and always motivating me to do cross-fit. It is because of my family that I have enjoyed doing engineering and learn the new culture and being with nature.

I would like to thanks all my friends at the TU, I really enjoyed making friends with varied nationalities learning their culture, food, and of-course some words from their language was really fun and made up to my other part of the life as a student. I also like to thank my friends at the gym who have tracked my progress through my masters and also have helped me stay very motivated to have a healthy body and a healthy mind. I am certain that our friendship shall be retained in one or the other way.

Executive Summary

In the search for understanding the formation and evolution of a solar system, terrestrial planets and any exoplanetary systems, the understanding of the evolution and formation of giant planet's play a crucial role. For this various studies of the atmosphere, gravitational fields, magnetic field of a planet is necessary. The primary goal here is in studying atmospheres, their physical and chemical processes governed by gases, clouds, and hazes are crucial for this understanding. This research focuses on developing a new technique to characterize aerosol particles using a nephelometer for any planetary atmosphere.

In this current research, a new technique is developed to visualize internal polarization field within an atmosphere from the incident solar flux. Here the internal field is evaluated for Saturn's and Venus's atmosphere. The current research is conducted in two parts, in the first part, an atmosphere radiative transfer model for Saturn and Venus is developed, following the radiative transfer model the internal polarization field is evaluated using Monte-Carlo technique. The second part of the research is to demonstrate the feasibility of the new instrument technique developed in first part with the aid of space system engineering. In the second part, the nephelometer instrument system throughput is analyzed, following which an SNR budget is evaluated to study the feasibility of new measurement technique with a nephelometer in Saturn's atmosphere.

From several fly-by and remote observation of Saturn, gives us a top-cloud topographical understanding of its atmospheric composition. There exists uncertainty with the composition of Saturn, as there is no in-situ data available yet. From several theoretical and experimental approach, three major layers are predicted in Saturn's atmosphere. These data are used for developing the current radiative transfer model. The radiative transfer model is developed from the molecular and aerosol optical thicknesses derived as a function of pressure and temperature. The optical thicknesses are obtained from complex refractive indexes of the particles predicted in the Saturn's atmosphere. Monte-Carlo technique is developed to evaluate the internal polarization field. For this a scatter probability phase function is developed that governs the photons movement within the atmosphere based on the optical thicknesses of the atmosphere. A similar approach is followed by Venus's model development.

In a measurement technique, the major contribution of losses is from the instrument itself. In the second part of the research, a system throughput analysis is done to evaluate the feasibility of the new technique developed in the current research for measuring the polarization field in a low flux density atmosphere. For this, an optical throughput is evaluated using a theoretical approach with a comparative trade-off study, following which the electrical throughput is evaluated theoretically and as well a comparative study is done with the commercially available detectors. With the aid of advancements in CCD technology that can measure at very low photon flux densities ($0.5e^{-}$/photon/pixel), the improvement in signal to noise ratio is evaluated for Saturn's atmosphere.

The forward model developed in the current research can be used to evaluate the internal polarization field of any planetary atmosphere. For which the composition, molecular and aerosol optical thicknesses are known and can be defined. The re-usability of the model is demonstrated in the current research, and the internal field for Saturn's and Venus's atmosphere is evaluated using the same forward model. From the SNR analysis, the direct measurement technique developed in this research, for Saturn's atmosphere demonstrates a possibility to derive the vertical structure up to 2[bar] pressure and for Venus's atmosphere at all altitudes as the available solar flux at this planet is 200 times more than that of Saturn.

List of Figures

List of Tables

Contents

1

Introduction

> If opportunity doesn't knock, build a door
>
> ***Milton Berle***

Introduction

In the search for understanding the formation and evolution of a solar system, terrestrial planet's and any exoplanetary systems, the understanding of the evolution and formation of giant planet's play a crucial role. The giant planet's are formed by collapsing of the giant gas and dust disc that was left after the Sun was formed. Key aspects to study for these giant planet's include composition and processes that occur within the atmosphere, their gravitational fields, magnetosphere, their ring systems if present, and system of moons. Here the primary goal is to study the atmospheres and their physical and chemical processes. The physical and chemical processes are governed by the composition of the atmosphere itself, such as gases, clouds, and hazes. To understand these compositions several scientific measurements have to be conducted both remote and/or in-situ. A nephelometer is one such measurement technique, that can characterize clouds and haze aerosol particles in any planetary atmosphere. This research focuses on developing a new technique to characterize aerosol particles using a nephelometer. For this development, a new forward model is developed that contains a planetary atmosphere model based on a scattering phase function and evaluates the polarization information that the instrument measures along the descent path of the probe as a function of the local horizontal plane.

1.1. Planetary atmosphere

A planetary atmosphere refers to gases that surround a planet. To understand a planetary atmosphere involves various aspects such as atmospheric temperature, pressure, structure and chemical composition and the various dynamic or chemical process within the atmosphere. The study of the planetary atmospheres within our solar system can be broadly classified into two categories based on the planet's distance to the sun. The planet's that are near to sun are called as terrestrial planet's and the planet's that are much further away usually outside the Earth's orbit are called as the giant planet's. The first group include planet's such as Mercury, Venus, Earth, and Mars, while the second group include Jupiter, Saturn, Uranus, and Neptune.

The terrestrial planet's were formed 4.6 billion years ago. These planet's were formed from the solar nebula which is a giant disk of gas and dust. The solar nebula also contained rocky solids, ice, and the gas, these aggregated and collapsed under gravity to form larger solid bodies as a course of time and formed the four terrestrial planet's. The larger rocky bodies accumulated smaller planetesimals bodies. The atmospheres were formed from the heating during accumulation, outgassing and vaporizing volatile substances at a lower temperature. The terrestrial planet's have volatile substances such as water, carbon, and nitrogen from the smaller planetesimal bodies. The atmospheric gases were released by large amounts into space mostly from the *high ultraviolet flux* from the younger Sun. The Sun's flux and intensity has changed over time and the atmosphere has evolved and changed due to oxidation, the total atmosphere mass and the gaseous amount has changed over time.

The formation of giant planet's is similar to that beginning of the terrestrial planet's. The formation of the giant planet's is not finished even after 4.6 billion years, they have not evolved as much as the terrestrial planet's, and the knowledge of the evolution of terrestrial planet's especially Earth is well understood from several scientific studies. The evolution of the giant planet's is very minimal in understanding. The gas giants Jupiter and Saturn were formed from the icy solids and the nebulae gas around the icy solids. Whereas the Uranus and Neptune are mostly formed of icy solids they grew too slow to accumulate or capture the nebulae gas. The giant planet's are of ice solids and no strong gravitational fields.

The formation of all these planet's followed a similar process, while some gases did escape the planet's while others were retained, these depend on the temperature and the surface gravity of those planet's. The flux or heat from the sun and the planet's distance to the sun affected what was retained. The formation of heat as the bodies collided and accumulated smaller bodies influenced the chemical reactions such as outgassing and vaporizing of volatile elements. These elements depended on the rock-forming minerals, these in-turn determines the composition of gases released in these process. The suns ultraviolet radiation intensity at these planet's determined what was retained and the influence decreased as the planet's distance increases. This makes it very interesting to study the atmosphere of the giant planet's to understand the planetary formation better than by studying the terrestrial planet's. The gas giants retained much of the lighter gases released during formation as the sun's ultraviolet radiation intensity decreases at the giant planet's which usually drive of the light gases. This principle is true with respect to Mercury the closest planet to the sun that has no atmosphere.

1.1.1. Clouds and Hazes

As the planetary atmospheres evolved the nature of these atmospheres is determined from other properties such clouds and hazes. The clouds and hazes present in the atmosphere have a variety of influences on the planet's atmosphere. The sun's flux that reaches these planetary atmospheres, part is reflected back to space, part is absorbed and a part is scattered by these clouds and hazes. The amounts reflected, scattered or absorbed are based on the composition of these clouds or hazes. The solar radiation distribution within the planetary atmosphere is also determined by the absorption and reflection by the gas particles. The radiation that reaches the surface after partial absorption and reflection heats up the surface and emits infrared radiation at longer wavelengths than the incoming radiation. This surface emission is partially absorbed or reflected that is determined by the atmosphere composition. The rotational motion of the planet's also influence the atmospheric processes. These factors highlight the need to study the planetary atmosphere, especially, the influence of clouds and hazes on different chemical, thermo-dynamical cycles, and radiative balance of the atmosphere.

The clouds and hazes are mostly composed of aerosols. Aerosols are suspended particles in a planetary atmosphere. These aerosols could be naturally occurring as generated from the volcanic eruptions, dust winds, sea salt. On Earth, they could also be human-made aerosols, such as ashes from burning forests, coal, oil and black carbon. These aerosols can absorb and scatter light. The aerosol composition increases or decreases the brightness of the clouds as perceived by the eyes. The aerosols affect the planet's climate both directly and indirectly as demonstrated in Figure 1.1. Directly by absorbing or by reflecting the Solar radiance into space. Indirectly by altering the properties of the clouds by decreasing the cloud precipitation efficiency (smaller particle size), as these aerosols act as cloud condensation nuclei (Twomey 1977, Kaufman et al. 2005) and by changing their optical thicknesses (albedo). There is also a semi-direct method where clouds burn-off aerosols by absorbing more heat. These direct and indirect influences of the aerosol particles affect the climate, hurricane genesis, biogeochemistry, radiation budgets and other dynamic processes of planetary atmospheres. The study of the aerosol is hence crucial to understand the complete chemical and dynamical process of a planetary atmosphere.

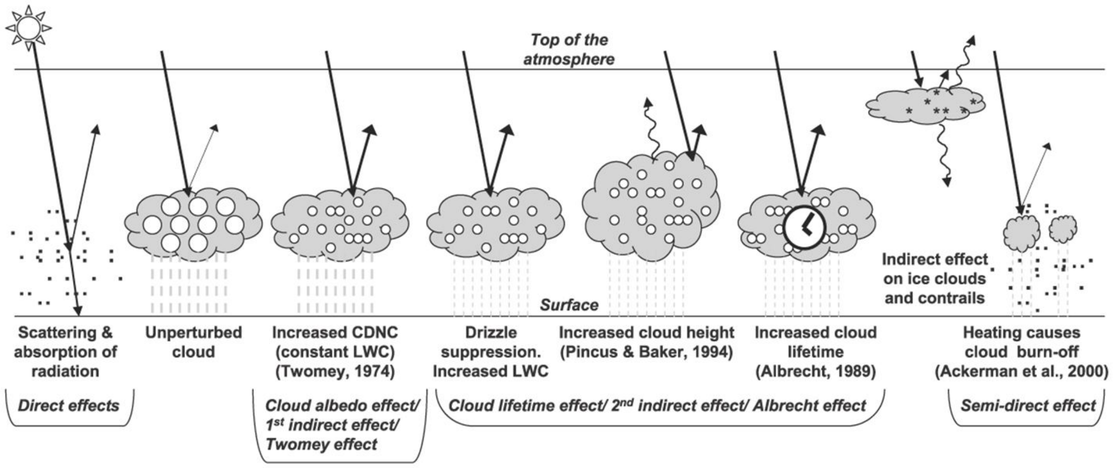

Figure 1.1: Aerosol direct, semi-direct and indirect affects on the planetary atmosphere climate. [9]

1.2. Remote versus In-situ observations

The planetary atmosphere studies require various observation to be done along the spatial and temporal changes. For this, it is required to conduct both remote and in-situ observation to have a complete picture. That is remote observation gives an analysis on a global scale and the in-situ measurement takes place at single or multiple locations. The advantages of an in-situ measurement are that the sampling rate is directed by the accessibility as the measurement can be done below and in the clouds, whereas the remote observations sampling rate is governed by the repeatability of the satellite cycles.

Aerosol characterization can be dated back to 1929, to a ground-based observation on earth of the direct/diffused sunlight conducted by Ångström, A. The paper outlines the spectral dependency of the extinction coefficient (absorption spectra) and the aerosol size using an empirical representation [10]. Later the aerosol particle size distribution was retrieved using spectral extinction coefficients and numerical techniques. Soon many studies led to the retrieval using spectral attenuation and scattering properties of aerosol particles to determine the size distribution. [Twomey and Howell, 1967[70] [69]; Yamamoto and Tanaka[77], 1969; Dave, 1971 [23]; Grassl, 1971[29]; Herman et al., 1971 [35]; King et al., 1978 [38]; Shaw 1979[62] and Nakajima et al.1983 [47]] are few of the studies conducted on retrieving the aerosol properties. All of these studies were conducted on the assumption of the aerosol as a spherical homogeneous particle and with a prior assumption of the refractive index.

There are several remote and a single in-situ observation performed on atmospheres of giant planet's to characterize their aerosol properties. These include the observations from the ground, space-borne telescopes and satellite fly-by's. In-situ observation of Jupiter's atmosphere is by the *Galileo* entry probe (Dec 7^{th}, 1995) the probe descended down to ~ 22 bars and the temperature at this pressure in Jupiter is 429 K, which is about 126 km below the one bar. The other remote or fly-by observation was done by the *New Horizons* mission that was destined to orbit Pluto and its moons, by Cassini, Pioneer, and by *Voyager* spacecraft. Whereas there are no in-situ observations conducted yet on the other gas giant Saturn. There are several fly-by's and remote observations conducted by *Cassini* spacecraft. There is an in-situ observation done on Titan, the biggest moon of Saturn, by *Huygens* probe (Jan 14^{th}, 2005) carried onboard the *Cassini* spacecraft. The *Huygens* probe entered Titan's atmosphere at 6 km/s. It had a controlled descent that took 2.5 hours down to the surface and the probe sent data during its descent and also extended to send data for 74 minutes after landing. This mission aided in understanding the atmospheric structure, optical thicknesses, composition, and winds of Titan. In general, the remote observations are conducted in all possible wavelength regions, namely, ultraviolet, visible and infrared regions. However, they are limited to observations of only the top layers of atmosphere down to few bars of pressure, depending on the optical thicknesses of hazes/clouds. The penetration of radio signal (radio occultation methods) is higher and can be extended to even lower layer and deeper pressure of few hundreds. To complete the big picture it is necessary to perform in-situ measurements also in the Saturn's atmosphere. *Hera* is an M-class mission that is planned to carry a single entry probe for in-situ observations in Saturn's atmosphere.

1.3. Nephelometer

There are several in-situ observation techniques for characterizing aerosol in a planetary atmosphere. Nephelometers are instruments that measure the density, size distribution, and refractive index of the suspended particles by measuring the aerosol light scattering properties. For terrestrial planet's, especially Earth, several in-situ measurements included nephelometer on-board, this includes, airborne, ground-based measurements. The Pioneer Venus's probes included two nephelometer experiments one placed on the large probe (sounder probe, day side), and the other on the smaller probe (night side probe). The nephelometer instrument requirements varied little for both the large and small probes, given the different criteria for the probe launch position into the atmosphere. For the giant planet's, a nephelometer experiment was part of the payload of the $Galileo$ entry probe. All these missions measured only the scattered flux intensity to derive the microphysical properties of the aerosol.

A nephelometer schematic developed by NOAA is shown in Figure 1.2. This schematic can be used as an example to understand the principle of a nephelometer that measures scattered flux to derive the microphysical properties of the aerosol. The scattering properties are determined by measuring the scattered light from aerosols. The working principle is that instrument measures the scattered flux of light over a distance, the extinction of light occurs due to scattering and absorption of light by the particles present in the compositions. The nephelometer presented in Figure 1.2 measures the scattered light at three different wavelengths red (700 nm), green (550 nm), and blue (450 nm).

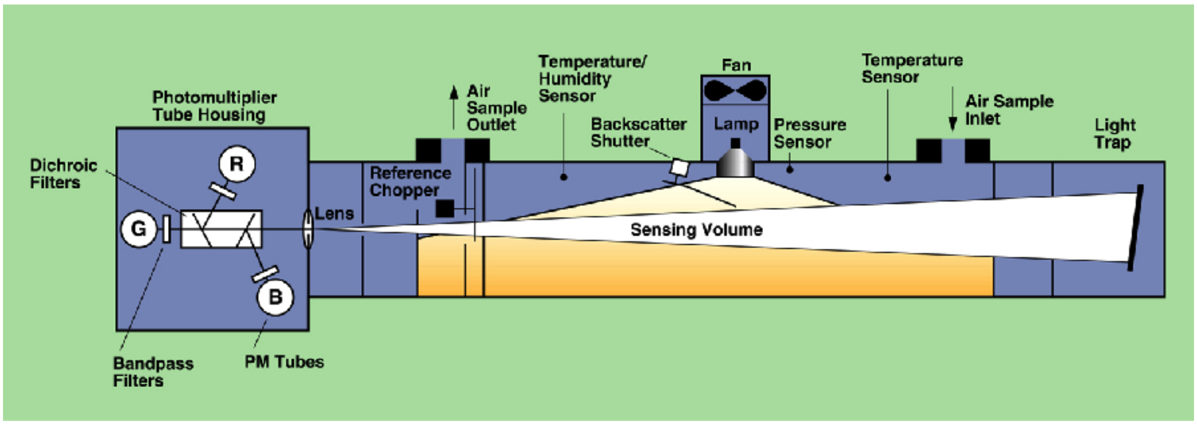

Figure 1.2: TSI 3563 Nephelometer schematic courtesy of TSI Incorporated. [3]

$$b_{ext} = b_{abs} + b_{sca} = \frac{ln\left(\frac{I}{I_0}\right)}{x} \tag{1.1}$$

where,
x = length of light path
I = Intensity of light after certain distance x
I_0 = Initial intensity of light
b_{abs} is the absorption coefficient, and can be further expressed as,
$b_{abs} = b^a_{abs} + b^m_{abs}$
b^a_{abs} = aerosol absorption coefficient, b^m_{abs} = gas absorption coefficient
b_{sca} is the scattering coefficient, and can be further expressed as,
$b_{sca} = b^a_{sca} + b^m_{sca}$
b^a_{sca} = aerosol scattering coefficient, and b^m_{sca} = gas scattering coefficient

The nephelometer here measures b_{scat} and b^m_{sca} and subtracts them to get the aerosol scattering coefficient b^a_{sca}. For measuring the b^m_{sca} the initial air sample is filtered to measure the scattering by gas particles. For the total absorption coefficient, the gas absorption coefficient b^m_{abs} is neglected. The equation derived by Middleton (1958) and Butcher and Charlson (1972) that governs the instrument presented in the schematic is used to evaluate the b_{scat} and further computation gives b_{abs}:

$$B = \frac{I_0}{y} * \frac{b_{scat}}{2I} \tag{1.2}$$

where,
y = vertical distance from light source to the sensor
B = flux of light detected by the sensor

1.3.1. Pioneer Venus's probe

The *Pioneer Venus's* probe measures the vertical profile of Venus's clouds and hazes at the four different locations chosen for the probe entry from an altitude of 63km to Venus's surface. Each of the four probes included a backscattering measurement nephelometer [54]. The nephelometer measurement reveals three cloud structures and identified in Figure 1.4 as upper, middle and lower clouds layers from the synthesis report for Venus's clouds [39]. The upper clouds layer is located in between 56-68 [km], the middle layers are located from 49-56 [km], and lower clouds layers are located below 49 [km]. The data from four probes are analyzed and the extinction coefficient for the cloud layers along the vertical structure measured at 175° (backscatter angle) is presented in Figure 1.4.

From the of the Pioneer Venus's nephelometer and Venera 9 results Figure 1.4. The upper cloud regions are characterized by a weak back-scattering signal. The middle clouds display stronger signal than the upper

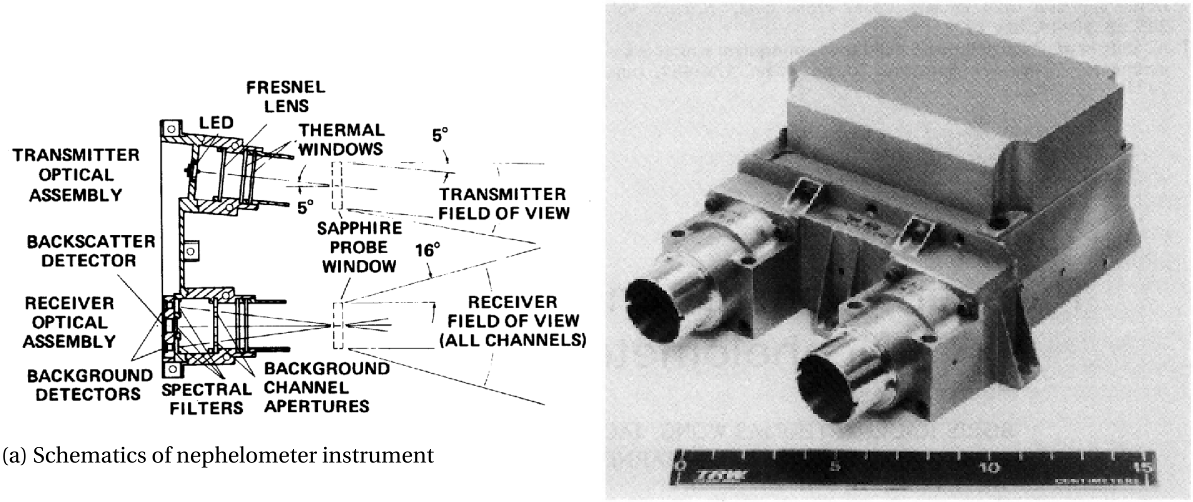

(a) Schematics of nephelometer instrument

(b) The Pioneer Venus Nephelometer instrument

Figure 1.3: Pioneer Venus's Probes- Nephelometer instrument[57]

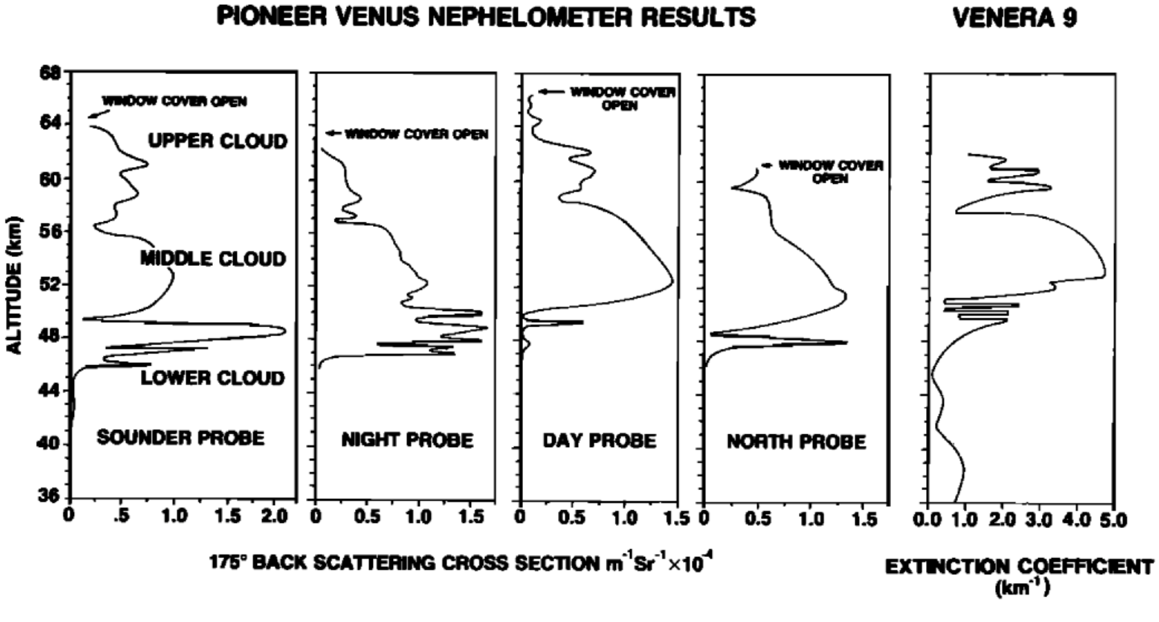

Figure 1.4: Scattering extinction coefficient for four region at 175° angle . [54]

clouds. In the lower layers, the clouds are much more layered, this can be seen with the extinction cross-sections in Figure 1.4 where a distinct peak appears at each of the layered clouds between 44-49[km].

The particle size distribution is obtained from the measured data of Large probe Cloud Particle Spectrometer (LCPS) onboard the sounder probe. The above extinction cross-sections from the scattering method are used for the particles between $0.5-5\mu m$ and imaging method used for larger particle sizes of $5-500\mu m$. The best-fit curve method is used to evaluate the aerosol composition by altering the refractive index (n) to get the best fit and determine the composition. The Venus cloud has a total optical thickness of 25-35 at the visible wavelength range. The upper cloud layer has a bimodal size distribution, and middle and lower cloud layers have trimodal size distribution [39]. The mode1 has an aerosol size in the range $0.1-0.5\mu m$ and a best-fit refractive index of 1.40-1.46 which is consistent with H_2SO_4. Using the intensity profile doesn't exclude the probability for other fits and permits many other species that could fit the refractive index profile. The mode2 has a size distribution of $1.8-2.8\mu m$, and a refractive index also in the range 1.40-1.46. For mode3 the size distribution is $6 - 9 \mu m$, and the real refractive index is unknown and probably in the range of 1.5-1.7.

1.3.2. Galileo entry probe

In-situ observation of Jupiter's atmosphere one of the giant planet's is by the *Galileo* entry probe (Dec 7^{th}, 1995) the probe descended down to ~ 22 bars and the temperature at this pressure in Jupiter is 429 K. The results from the Nephelometer experiment are summarized here from [56]. This paper presented the results of the vertical cloud structure of the $5 \mu m$ "hot spot " region and is well documented for 0.46-12 bar. Three distinct cloud regions were identified, the first region starts from 0.46-0.55 bar, a feeble portion of the predicted ammonia haze was determined and the cross section for the ammonia haze as a function of particle density N_0 is presented in Figure 1.6a and Figure 1.6b. The second region of clouds was from the 0.76-1.34 bar a dense particle structure was present and identified as the ammonium hydrosulfide cloud with the extinction cross-sections as shown in in Figure 1.6c and Figure 1.6d. There was a thin vertical layer determined at 1.65 bar a layer of cloud isolated from the earlier region and also the possibility of water condensation was predicted. The third region is from 1.9-4.5 bar has uncertainty in the structure and displayed weak identification features and an imprecise conclusion was drawn as the measured signal (scattered light) was very weak, as seen from the extinction cross-section Figure 1.6e and Figure 1.6f. The fig. 1.5 shows the determination of the particle size determination and the refractive index deduced from the extinction coefficient.

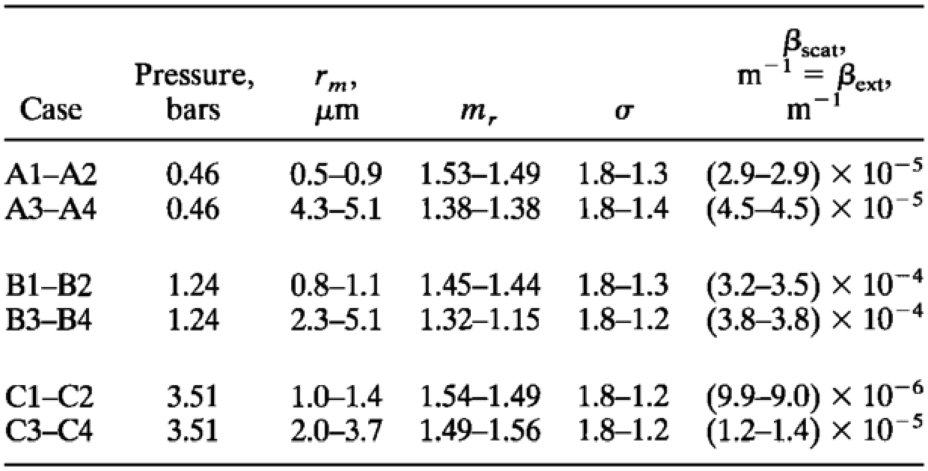

Case	Pressure, bars	r_m, μm	m_r	σ	β_{scat}, $m^{-1} = \beta_{ext}$, m^{-1}
A1–A2	0.46	0.5–0.9	1.53–1.49	1.8–1.3	$(2.9–2.9) \times 10^{-5}$
A3–A4	0.46	4.3–5.1	1.38–1.38	1.8–1.4	$(4.5–4.5) \times 10^{-5}$
B1–B2	1.24	0.8–1.1	1.45–1.44	1.8–1.3	$(3.2–3.5) \times 10^{-4}$
B3–B4	1.24	2.3–5.1	1.32–1.15	1.8–1.2	$(3.8–3.8) \times 10^{-4}$
C1–C2	3.51	1.0–1.4	1.54–1.49	1.8–1.2	$(9.9–9.0) \times 10^{-6}$
C3–C4	3.51	2.0–3.7	1.49–1.56	1.8–1.2	$(1.2–1.4) \times 10^{-5}$

Figure 1.5: Size distribution and refractive index using nephelometer data of Galileo probe for the three cloud layers of Jupiter, layer1 A1-A4, layer2 B1-B4, layer3 C1-C4 [56].

The Galileo probe included a multi-angle measurement of the scattered light, the scatter angles measured here are 5.82, 16.01, 40.00, and 70.00 deg for forward scatter and 178 deg for the backscatter angle. A schematic of the optical subsystem is shown in the Figure 1.7, as seen from the figure the optical setup has two channels the forward and backward scattering channel. The scattering volume is defined by the field of view of the detector and the source field intersection. The instrument uses pulsed solid-state laser light sources, and solid state scattered light detectors. The forward scattering detection is done using conical mirrors that extend outwards radially, the light scattered in the forward direction is reflected by these conical mirrors to be collected by the forward scattering channel detectors. In case of the backscatter, the source and the optical axis are placed parallel, the light scattered near the backscattering wide angle close to 180 deg is collected and measured. The backscatter measurement angle is fixed, the forward scatter can be measured at different angles, by fine-tuning the conical mirror position and changing the intersection with the scatter area as seen in Figure 1.7b. The deployable arm has heaters wires that run till the mirror, to obtain a constant temperature during the descent of the probe. The two scattering units or channels have grid-heated glass windows to protect the detector from thermal effects.

1.4. Polarization Nephelometer

A conventional nephelometer measures the intensity of light scattered by aerosol particles Equation (1.2), in general, the detector is placed at 90° to the light source. The scattered light is used to determine the extinc-

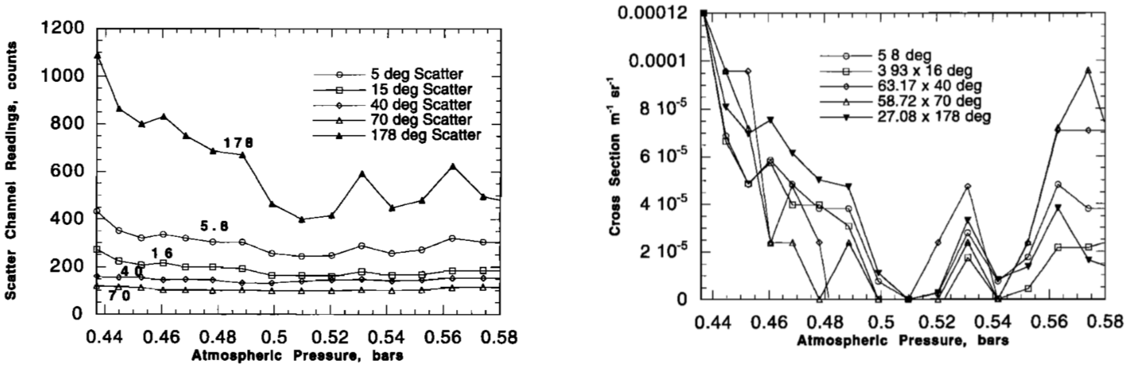

(a) Raw scatter channel readings at 0.42-0.58 bar

(b) cross sections at 0.42-0.58 bar, normalized to zero p=0.510 bar

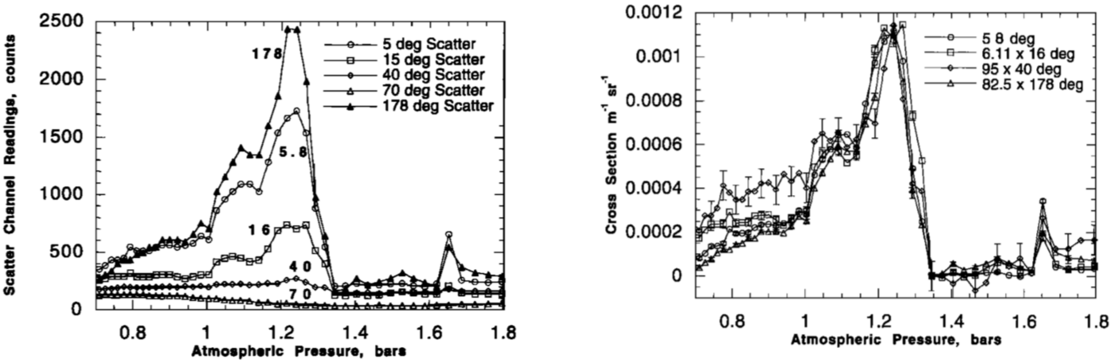

(c) Raw scatter channel readings at 0.7-1.8 bar

(d) cross sections at 0.7-1.8 bar, normalized to zero p=1.345 bar

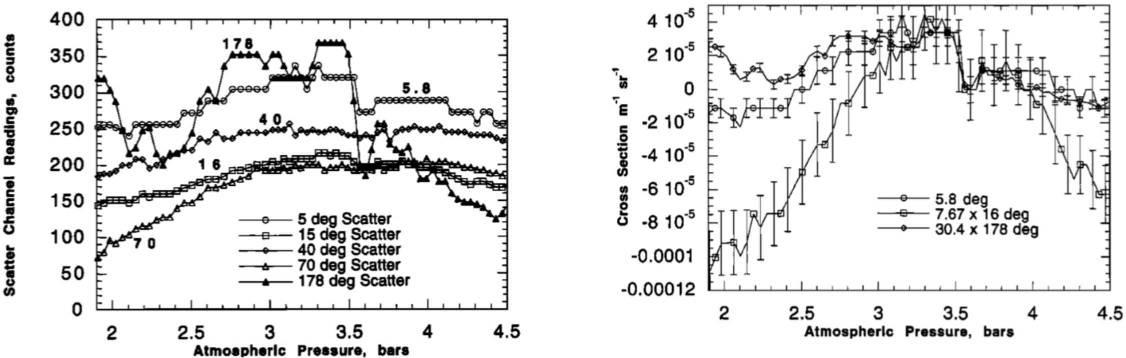

(e) Raw scatter channel readings at 1.9-4.5 bar

(f) cross sections at 1.9-4.5 bar, normalized to zero p=3.603 bar

Figure 1.6: Scattering channel cross sections $F(\theta) = N_0(d\Sigma/d\Omega)_\theta\ m^{-1}sr^{-1}$,here N_0 is the density of particles and $d\Sigma$ is the differential scattering cross-section for scattering from the incident beam into solid angle element $/d\Omega$ at scattering angle θ. for each channel measured at different regions derived from the scattering flux at the detector [56]

tion coefficients of the particle composition (gas+aerosol). In this method for finding the optical properties of the gas particles, a filtered air sample is measured initially as described in Section 1.3. The particle density is measured as a function of the reflected light, this reflected amount of light into a detector is based on the shape, size and refractive index of the particle composition. Then the particulate composition is derived from the intensity and spectral absorption lines and band by a best-fit method. This method is limited, when using the scattered intensity many compatible compositions fit the intensity profile. This method needs additional radiometric and spectroscopic measurements, to narrow down the composition that fits the measurement.

To overcome the ambiguity by just measurement of particle scattered intensity profile, polarization property of the light could be used. The spectral intensity such as color and thermal emission depends on the

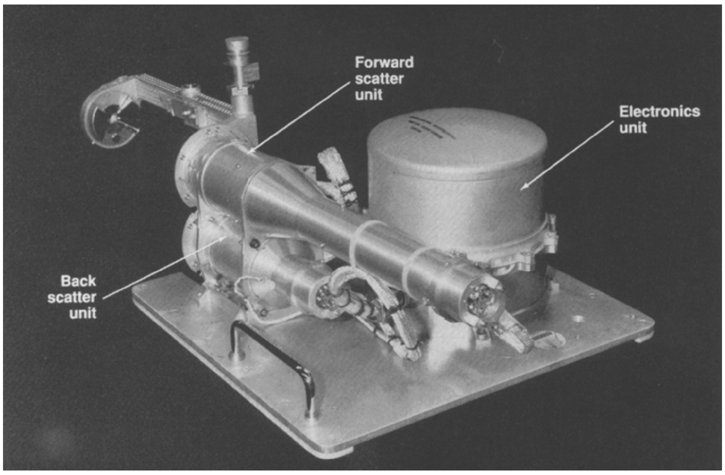

(a) The Galileo Nephelometer instrument

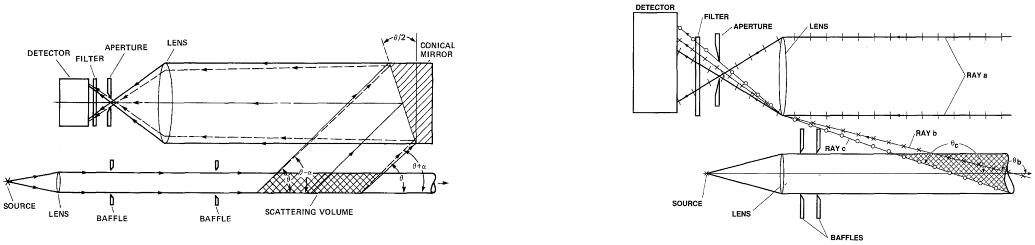

(b) Schematics of Galileo nephelometer instrument (forward scatter)

(c) Schematics of Galileo nephelometer instrument (back scatter)

Figure 1.7: Galileo Probe- Nephelometer instrument[55]

materials. The polarization is greatly influenced by the particle composition, shape, and roughness. It is shown that the polarization is applied for obtaining enhanced contrast. The application of polarization are many, for example, the study of composition of Venus's atmosphere by Hansen & Hovenier, 1974, obtained a definitive fit for particle size distribution and refractive index Figure 1.8 and concluded that Venus's clouds are composed of concentrated sulfuric acid from the spectral refractive index [31].

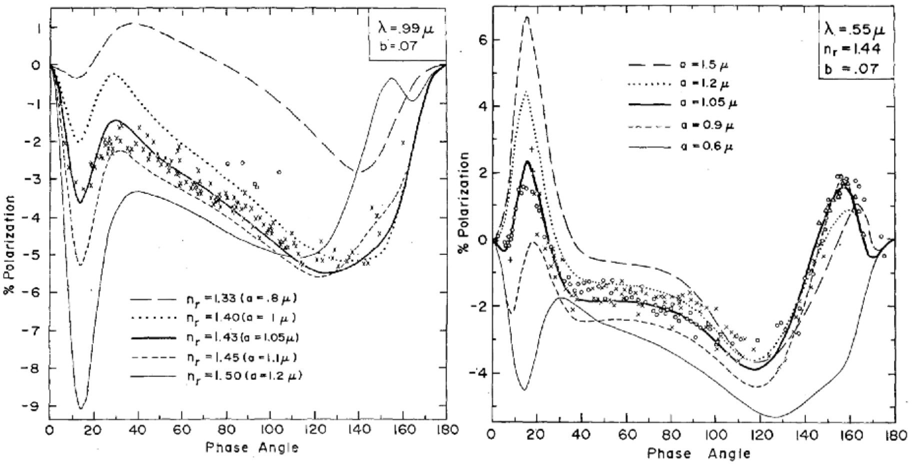

Figure 1.8: Venus's clouds composition derived from polarimetry (ground based measurement), degree of linear polarization at multiple phase angle and definitive model fit for (a) size distribution and (b) refractive indices [31]

The polarization information can be used for target decision, as shown in the Figure 1.9 the tank is in thermal equilibrium with its surroundings and cannot be distinguished from its background when just the scattered intensity is measured. Using the polarization information the tank can be easily discerned.

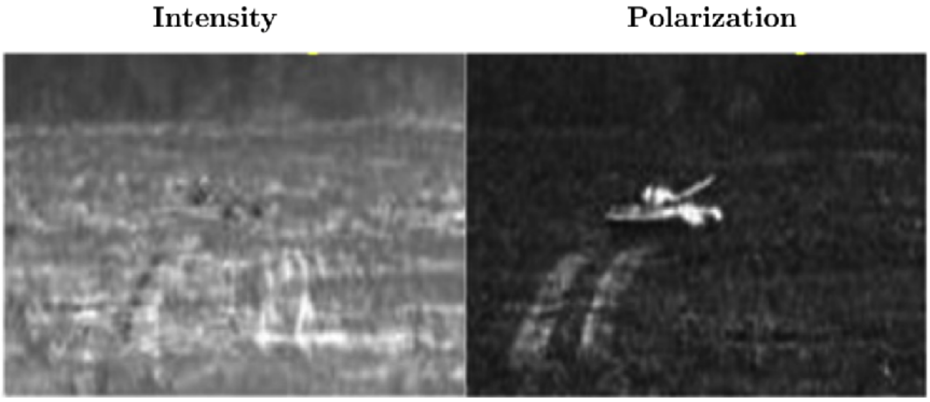

Figure 1.9: Tank in thermal equilibrium, imaged with an infrared camera in intensity and degree of linear polarization (courtesy: David Cenault, Polaris).

The application of polarization information is also found vastly in astronomy, the observation of a young star T-Tauri as shown in Figure 1.10 can be seen that observation using intensity information gives little information about the circumstellar disc, while a sensitive imaging using polarimetry reveals a vast circumstellar disc around the young star. There are also many other applications possible such as biomedical diagnostics. This application shows that the polarization information of light can overcome the ambiguities in composition determination that arise from using intensity profile measurement technique.

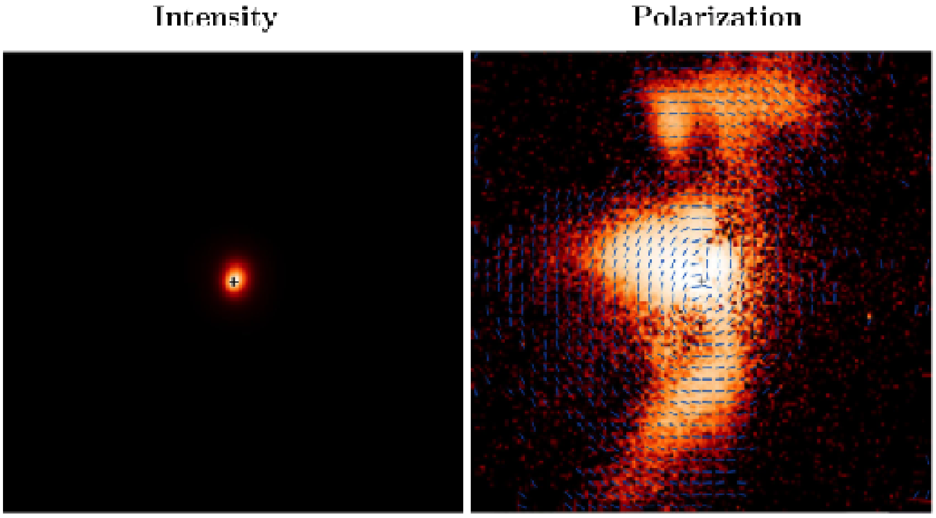

Figure 1.10: circumstellar disc that is visible when imaged for degree of linear polarization information and not visible when only intensity profile is measured.

Utilizing the polarization information namely the degree and angle of linear polarization from the particle scattered light can enhance the identification process of the particle composition, size, and shape (microphysical properties). A multi-angle, multi-spectral polarization measurement technique is required. The polarization information is very sensitive and when retrieving this information an instrument could induce or alter the actual polarization. To overcome the so-called instrumental polarization effect several polarization modulation techniques are developed. The polarization information can be represented in a vector form using Stoke's formalism Equation (1.3)

$$S = \begin{pmatrix} I \\ Q \\ U \\ V \end{pmatrix} = \begin{pmatrix} E_{x_0}^2 + E_{y_0}^2 \\ E_{x_0}^2 - E_{y_0}^2 \\ 2E_{x_0}E_{y_0}\cos\delta \\ 2E_{x_0}E_{y_0}\sin\delta \end{pmatrix} = \begin{pmatrix} \leftrightarrow + \updownarrow = \searrow + \nearrow = \circlearrowright + \circlearrowleft \\ \leftrightarrow - \updownarrow \\ \searrow - \nearrow \\ \circlearrowright - \circlearrowleft \end{pmatrix} \tag{1.3}$$

where, E_{x_0} and E_{y_0} are the electric field components along X and Y direction and the wave is travelling in Z direction. The δ is the phase delay of component Y with respect to X. The total intensity is represented by I, Q defines the intensity difference in vertical and horizontal polarization states, U defines the intensity difference at ±45° polarization states, V defines the intensity difference between right and left-handed circular polarization states (Collett E 2005).

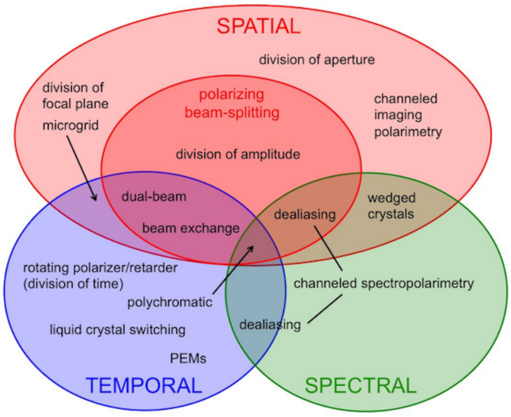

Figure 1.11: Venn diagram of polarization measurement/modulation domains. Venn diagram is from[64]

The polarization measurement can be done in a different domain, spatial, temporal, angular, spectral domain to name a few. There are three major types of modulation technique used for polarization measurement, spatial, temporal and spectral modulation. Different techniques that use each of these polarization measurement techniques is depicted as a Venn diagram in Figure 1.11.The efficiency of these polarization measurement techniques is described as how efficiently the Stoke's parameters are deduced from the scattered radiance:

- Spatial modulation technique - polarizing beamsplitters are used and the light is split into three beams to deduce the Stoke's parameters. For Stoke's Q the beam is split and measured at 0° and 90°, for Stoke's U ±45°.
- Temporal modulation technique - a rotating polarizer is used in front of a fixed polarizer to obtain all three of the Stoke's parameters.

Each of these measurement techniques is unique and introduces different effects on the deduced signal. To overcome this differential effect based on the measurement technique, a spectral modulation technique was developed by [Snik & Keller 2013 [65]].

- Spectral modulation technique - the full linear polarization is encoded onto its spectrum. The signal coming out of a special optical head is a sinusoidal signal with amplitude representing the degree of linear polarization and the phase represents the angle of linear polarization. In general, the optical head consists of an achromatic quarter-wave retarder, an athermal multiple-order retarder, and a polarizer. This spectral modulation technique has shown a polarimetric measurement accuracy of 2.0%. The current research uses this technique for modulating the polarization information.

1.5. Research Objective

The *Hera* mission is an M-class mission planned to deliver a single entry probe to characterize the vertical profile of the Saturn's atmosphere. The entry probe shall also carry a Nephelometer on-board for aerosol characterization. The *Hera* mission nephelometer instruments preliminary proposed design is to carry two modules, LOAC (Light Optical Aerosol Counter) to measure the size distribution of particles, and PAVO (Polarimetric Aerosol Versatile Observatory) to measure particle shape and composition [45]. The design of PAVO also considers to collect the sample within the instrument and carries a broad bandwidth light source onboard see Figure 1.12 to measure the single-scattered light. The scattered light is measured at 9 angles θ: 12deg (the same as for LOAC), 30, 50, 70, 90, 110, 130, 150 and 170° [45]. This proposed concept considers sample acquisition within the instrument and limiting the sample range that could be measured.

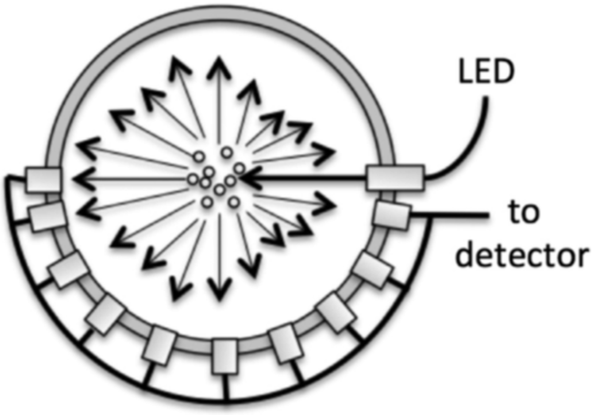

Figure 1.12: An artistic impression of the proposed nephelometer concept to *HERA* mission [45], that collects the sample within the instrument and carries a broad bandwidth light source on-board to measure the single-scattered light

As acquiring the sample within the instrument limits the sample concentration and/or range. The polarimetric technique advantages cannot be utilized to its full extent in this context with the proposed design for the *Hera* mission. The sample range is based on the efficiency of sample acquisition system, as for how efficient the in and outflow of the sample is designed. The sample acquisition could acquire particles or liquids that could block or contaminate the sampling region. The polarimetric method is developed to have enhanced contrast when the source sample is of greater distribution range a very good understanding of the aerosol composition can be derived. To measure a higher sample range, the alternate technique is to directly look at the atmosphere outside the entry probe and measure the composition. This technique can be used to derive the microphysical properties from the polarization information of the multiple scattered light inside a cloud or haze layer and along the descent of the probe. In the direct measurement technique, there is no need of carrying a source onboard, the natural sunlight acts as the source.

To realize the advantages of the direct measurement technique for low flux density planetary atmosphere requires a feasibility study. This brings us towards a step closer to defining the objective of this thesis research. There is an ambiguity to measure the state of polarization using naturally available sunlight in Saturn's atmosphere, as the flux intensity available at top of the Saturn's atmosphere is less, in the order of $\sim 14.91 W/m^2$. The core question of the research is to understand what is measured by a polarization nephelometer detector from a direct measurement technique in low in a low flux density atmosphere such as Saturn's atmosphere. As the measured flux is a convolution of the atmosphere phase function and the instrument transfer function. The derived objectives from the core question that can be defined for the invention cycle in this thesis are the characterization of Saturn's atmosphere model, followed by an instrument transfer function model. The main research question gives rise to several sub-question that needs to be answered, before approaching on a solution to the central research question.

- Central research question: What is the polarization flux at the detector from the direct measurement technique using the solar flux?
    - sub-question 1: How is the internal polarization field in a low flux density planetary atmosphere?
    - sub-question 2: What is the instrument feasibility in terms of Signal to Noise ratio at the detector for measuring the polarization information at low fluxes?

To answer the central research question, this research study shall formulate a new technique using a radiative transfer forward model and a nephelometer throughput signal to noise analysis. This model contains an atmosphere radiative transfer model governed by scattering phase function of a planetary atmosphere composition and evaluate the internal polarization field information that reaches the detector plane. This is followed by computing the convolution of instrument transfer function with the internal field data and perform a signal to noise analysis to demonstrate the feasibility of the new technique presented in this research. Following a brief introduction, In Chapter 2 the Stoke's formalism is introduced that is used to represent the polarization information of the scattered light, this is followed by a discussion on the spectral modulation technique that is used in the current research. In Chapter 3 the radiative transfer forward model developed for Saturn's and Venus's atmosphere is presented. In Chapter 4 the internal polarization fields evaluated from the forward model for Saturn's and Venus's atmosphere is discussed. In Chapter 5 a comparison study between the new technique developed in this research and the proposed concept to *HERA* are discussed.In Chapter 6 space system engineering approach is taken to develop an instrument transfer function for the new measurement technique developed in the current research and a feasibility analysis is performed for the new technique. The report ends with a conclusion on the feasibility study of the new technique developed using a radiative transfer forward model for polarization nephelometer in low flux density planetary atmosphere.

2

Spectropolarimetry

Most people say it is the intellect which makes a great scientist;
They are wrong: it is the character.

Albert Einstein

Introduction

The conventional nephelometer technique based on the intensity measurement alone to retrieve the microphysical properties of the aerosols is ambiguous and assumes a spherical particle shape. In Chapter 1 the advantages of using polarization information of the scattered light over the intensity measurement to retrieve the aerosol properties was briefly discussed. This chapter discusses a spectral polarimetry modulation technique used to increase the accuracy of measuring small polarization signals giving a polarimetry accuracy of 2.0%. This technique is combined with multi-angle observations to obtain an unambiguous retrieval of the aerosol microphysical properties. The multi-angle is obtained by using multiple fields of view. This can be extended to multi-spectral observation by using a broadband light source, either sunlight or a white light source. In this chapter, Stoke's formalism used for measuring the polarization information namely the degree and angle of linear polarization are discussed.

2.1. Stoke's Vector

The light intensity I is comprised of the sum of unpolarized and polarized light,

$$I = I_{unpol} + I_{pol} \tag{2.1}$$

The degree of polarization of a light is defined as the ratio of polarized light to total intensity $\left(\boldsymbol{I_{pol}/I}\right)$. This polarized part of the light is elliptically polarized and further this can be categorized as linear $\left(\boldsymbol{I_{lp}}\right)$ and circularly $\left(\boldsymbol{I_{cp}}\right)$ polarized light.

$$I_{pol} = I_{lp} + I_{cp} \tag{2.2}$$

Given a light beam with circular frequency $\boldsymbol{\omega}$ travelling in positive $\boldsymbol{z}$ direction. The electric field components along any two mutually perpendicular direction represented by unit vectors $\vec{\boldsymbol{r}}$ and $\vec{\boldsymbol{l}}$ is given by,

$$\begin{aligned} E_l(t) &= a_l e^{i(\omega t - kz - \epsilon_l)} \\ E_r(t) &= a_r e^{i(\omega t - kz - \epsilon_r)} \end{aligned} \tag{2.3}$$

where, **t** represents the time, **k** is the wave number, $\boldsymbol{a_l}$ and $\boldsymbol{a_r}$ are the amplitudes and $\boldsymbol{\epsilon_l}$ and $\boldsymbol{\epsilon_r}$ are the phases, the direction of propagation is along $\vec{\boldsymbol{r}} \times \vec{\boldsymbol{l}}$.

The Stoke's vectors can be derived from the time-averaged values of the electric field components. The Stoke's parameters could also be a superposition of sum of Stoke's parameters from independent waves. The total intensity measured along a particular direction making an angle $\boldsymbol{\Psi}$ along the direction vector $\vec{\boldsymbol{l}}$ [32],

$$I(\Psi, \varepsilon) = \frac{1}{2}\left[I + Q\cos 2\Psi + (U\cos\varepsilon + V\sin\varepsilon)\sin 2\Psi\right] \tag{2.4}$$

where, $\boldsymbol{\varepsilon}$ is the retardation factor of $\boldsymbol{E_r}$ with respect to $\boldsymbol{E_l}$

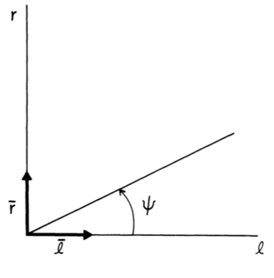

Figure 2.1: The total intensity of light measured along a particular direction making an angle $\boldsymbol{\Psi}$ with the $\vec{\boldsymbol{l}}$ direction [32].

The Stoke's vector evaluation using the traditional measurement technique,

$$S = \begin{pmatrix} I \\ Q \\ U \\ V \end{pmatrix} = \begin{pmatrix} a_r^2 + a_l^2 \\ a_r^2 - a_l^2 \\ 2a_r a_l \cos\delta \\ 2a_r a_l \sin\delta \end{pmatrix} = \begin{pmatrix} \leftrightarrow + \updownarrow = \text{⤡} + \text{⤢} = \circlearrowright + \circlearrowleft \\ \leftrightarrow - \updownarrow \\ \text{⤡} - \text{⤢} \\ \circlearrowright - \circlearrowleft \end{pmatrix} \tag{2.5}$$

where, $\delta = \epsilon_l - \epsilon_r$.

$\boldsymbol{I}$ is the total intensity, $\boldsymbol{Q}$ defines the intensity difference in vertical and horizontal polarization states, $\boldsymbol{U}$ defines the intensity difference at ±45° polarization states, $\boldsymbol{V}$ defines the intensity difference between right and left-handed circular polarization states (Collett E 2005). The intensity of various polarization states can be represented using the Stoke's parameters.

Intensity of the polarized light,

$$\begin{aligned} I_{pol} &= \sqrt{\left(Q^2 + U^2 + V^2\right)} \\ I_{lp} &= \sqrt{\left(Q^2 + U^2\right)} \\ I_{cp} &= V \end{aligned} \tag{2.6}$$

The degree of elliptical polarization and degree of linear polarization,

$$\begin{aligned} P &= \frac{I_{pol}}{I} = \frac{\sqrt{\left(Q^2 + U^2 + V^2\right)}}{I} \\ P_L &= \frac{I_{lp}}{I} = \frac{\sqrt{\left(Q^2 + U^2\right)}}{I} \end{aligned} \tag{2.7}$$

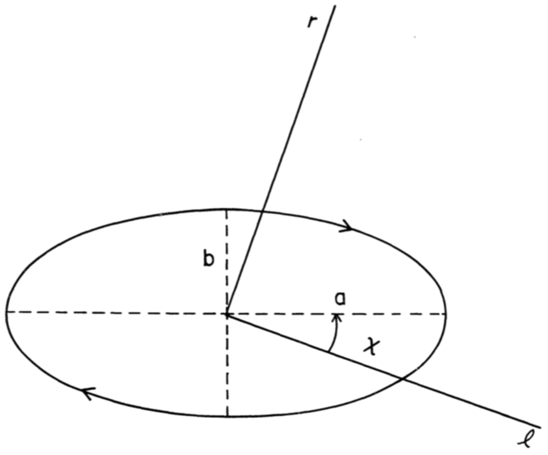

Figure 2.2: The polarization ellipse, with direction of propagation into the page, the shown rotation is a right-handed polarization [32].

The two electric fields integrated over time trace an ellipse as shown in Figure 2.2 and the ellipticity can be defined as $\mathbf{tan}\,\boldsymbol{\beta} = \pm\boldsymbol{b/a}$ (for details see [32]). Given a value of $\mathbf{tan}\,\boldsymbol{\beta} = \mathbf{1}$ means the light is right-handed circular polarized, $\mathbf{tan}\,\boldsymbol{\beta} = -\mathbf{1}$ means it is left-handed circular polarized and a value of $\mathbf{tan}\,\boldsymbol{\beta} = \mathbf{0}$ means the light is linearly polarized. The angle of polarization is the angle the major axis of the ellipse makes with the $\vec{\boldsymbol{l}}$ direction vector and is represented by $\boldsymbol{\chi}$ or in the simpler term it is the angle between the plane of polarization and plane of incidence.

$$\begin{aligned} \sin 2\beta &= \frac{V}{(Q^2 + U^2 + V^2)^{1/2}} \\ \tan 2\chi_L &= \frac{U}{Q} \end{aligned} \tag{2.8}$$

From the two values of $\boldsymbol{\chi}$ in the interval ($\mathbf{0} \leq \boldsymbol{\chi} < \boldsymbol{\pi}$) a value that brings $\mathbf{cos}\,\mathbf{2}\boldsymbol{\chi}$ to the same sign of $\boldsymbol{Q}$ has to be chosen.

2.2. Polarization measurement

Polarimetry is a sensitive remote observation technique for evaluating the optical properties of organic and inorganic compounds. The polarization state can be represented using the Stoke's parameters as discussed earlier. The linear polarization state can be determined as discussed in Section 2.1, given by the Stoke's parameters $\boldsymbol{I}\left(\leftrightarrow + \updownarrow\right)$, $\boldsymbol{Q}\left(\leftrightarrow - \updownarrow\right)$, $\boldsymbol{U}(\searrow - \nearrow)$, and for circular polarization $\boldsymbol{V}(\circlearrowright - \circlearrowleft)$. There are two modulation techniques that are available spatial and temporal modulation. In spatial modulation technique, the polarization states are obtained using four and in case only linear polarization is measured three beamsplitters is sufficient [32]. Each of the beamsplitters is placed in an orientation of 0°,90° (for determining $\boldsymbol{I}$ and $\boldsymbol{Q}$) and ±45° (for determining $\boldsymbol{U}$). Spatial modulation requires four different optical paths and detectors corresponding to the four polarization states that are measured or four different parts of an imaging array. With the temporal modulation method, the different polarization states can be measured using a rotating half-wave retarder in front of a fixed polarizer. This way all four polarization states are obtained sequentially as the retarder is rotated at different angles with respect to the optical axis of the fixed polarizer.

The spatial and temporal modulation techniques are sensitive to signal noise and system errors. Spatial modulation requires four different parts of an imaging array, for a precise measurement of polarization the four signals after the beamsplitter have to be differentially transmitted and aligned. Measuring 3 or 4 beams increases the size and mechanical complexity of the instrument. In the sequential measurement, the rotating retarder introduces differential effects such as time-variant effects of the source are introduced and due to the instrument pointing to varying optical properties of the atmosphere introduces spurious polarization signal. The rotating filter is an active component that requires additional power and control electronics, any vibration in the system would introduce a spurious polarization signal (see [63]). Beam exchange method includes the combination of spatial and temporal modulation, however, the instrument complexity and size are larger than the individual techniques combined [60]. In general, both the described modulation techniques are sensitive to random noise in each of the 3 or 4 individual measurements. The random noises pose a huge problem when the degree of polarization being measured is very low. Then the measured $\boldsymbol{Q}$ and $\boldsymbol{U}$ are mostly dominated by random noise.

In the following section, a different polarization modulation technique as a function of wavelength (multi-spectral) that is much less sensitive to above-mentioned differential effects is discussed. The instrument includes a fixed optical head configuration and encodes the polarization information onto a sinusoidal signal. This method is also called as channeled spectropolarimetry or polarimetric spectral intensity modulation. In this method, only linear polarization is evaluated and measures only 3 elements of the Stoke's vector $[I\ Q\ U\ 0]^T$.

2.2.1. Instrument Principle

The polarization nephelometer encodes the degree and angle of linear polarization of the light scattered by the sample particles into a sinusoidal signal. The degree of linear polarization is encoded as amplitude and angle of linear polarization is encoded into the phase of a sinusoidal signal. The polarization modulation is obtained using a special optical head to translate the scattered light and modulate it into two spectral modulated fluxes as defined by the equation Equation (2.11). The optical head consists of an achromatic quarter-wave retarder, followed by a chromatic multiple-order wave retarder and a polarizer. The quarter-wave retarders fast axis and the polarizer are oriented parallel, while the athermal multiple-order retarder axis is oriented at an angle of ±45° with respect to the optical axis of the other two components.

The Stoke's vector measurement using the spectropolarimetry (SPEX[71]) technique and the schematic of modulated signal $\boldsymbol{I_{\pm}(\Theta,\lambda)}$ is presented in Figure 2.3, the modulated signal is given by,

$$P_L(\lambda) = \frac{\sqrt{Q^2+U^2}}{I} \tag{2.9}$$

$$\chi_L(\lambda) = \frac{1}{2} arctan \frac{U}{Q} \tag{2.10}$$

$$I_{\pm}(\Theta,\lambda) = \frac{1}{2} I_0(\Theta,\lambda) \left[1 \pm P_L(\Theta,\lambda)\, cos\left(\frac{2\pi\delta(\lambda,T)}{\lambda} + 2\chi_L(\Theta,\lambda)\right)\right] \tag{2.11}$$

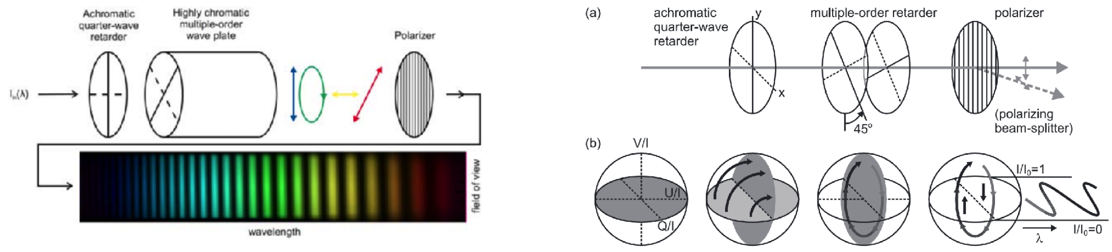

(a)

(b)

Figure 2.3: (a) SPEX instrument Optical head and working principle [71], (b) Schematic setup of the spectral modulator, (1) The solid and dashed lines represent the fast and slow axis respectively, (2) illustration of the modulation principle on the Pioncaré sphere[63].

The degree of linear polarization is given by (DoLP or $\boldsymbol{P_L(\Theta,\lambda)}$) and angle of linear polarization is (AoLP or $\boldsymbol{\chi_L(\Theta,\lambda)}$), the combined waveplate retardance is ($\boldsymbol{\delta\,(\lambda,T)}$), and the ± sign corresponds to the beam-splitter head. The above intensity is measured by the detector at the end of each of the two channels (I_+ and $I\_$). This intensity is a function of the scattering angle (Θ) and wavelength. The sum of the two modulated signal gives the total flux I. From the retardance term, it can be deduced that the modulation is not periodic with respect to wavelength. The retardance $\boldsymbol{\delta}$ should be chosen according to the spectral resolution that is required. The resolution of particle size distribution can be increased, by using a broad wavelength source light. Additional measurements are required to retrieve the information of the aerosols and incident source, for this the non-scattered light at 0° is measured to obtain the density of the sample (number of particles).

$$s_0\,(\Theta,\lambda) = I\,(\Theta,\lambda)\cdot t\,(\Theta,\lambda) \tag{2.12}$$

The intensity measured by the detector can be defined as a function of the modulated intensity $\boldsymbol{I_\pm}$ from the optical head and the transfer function $\boldsymbol{t}$ defined from the instrument losses and includes the transmission losses, analog to digital conversion losses, losses due to noise, the detector gain. This shall be for the individual detector placed at the scatter angle of interest. The polarization information provides better information about the microphysical properties of an aerosol over other methods that use intensity information. Spectropolarimetry technique encodes DoLP onto the amplitude and AoLP onto the phase of the modulating signal, giving a polarimetry accuracy of 0.2%. The aerosol properties can be derived from this detector data signal using the inversion algorithm similar to that by Di Noia et al. (2014)[25] applied for ground spectropolarimetric measurements. In the research [25] a neural network algorithm is used to retrieve the aerosol microphysical properties like effective radius and refractive index.

3

Radiative transfer forward model

No problem can be solved from the same level
of consciousness that created it.

Albert Einstein

Introduction

In the current research, to analyze the concept of polarization nephelometer to measure the polarization information under a very low flux density environment, such as giant planet's atmosphere, where the solar flux reaching the top of its atmosphere is less in the order of few (W/m^2), there is a need to understand the interaction of light in such environments and also the interaction with the instrument itself. For polarization nephelometer to derive the microphysical properties of atmospheric particles understanding the transverse nature of light is important. A numeric model is developed to understand the transverse nature of light and evaluate the internal radiation field in an atmosphere and this understanding is used to analyze the interaction of internal radiation with the instrument measurement. In this chapter, a new forward model is discussed on the interaction of sunlight and evaluating the internal field in an atmosphere and concludes with the method to evaluate the appearance of this internal field at the instrument plane. This model evaluates the internal field strength and the interaction of light namely the transverse nature using the Stoke's parameters as light is scattered in an atmosphere. Once the interaction of light in an atmosphere is modeled it can be used to evaluate the interaction at the nephelometer instrument interface which is discussed later in the Chapter 5 and Chapter 6.

In a forward radiative transfer model theoretical, experimental and observation data are utilized to construct an improved mathematical or numerical model to study various atmospheric sciences and processes. Currently, there exists no model that computes a polarization internal field on the interaction of light with the atmospheric particle in detail. There exist models based on the double-adding method which evaluates a cloud-top topography for a global field assuming horizontally homogeneous layer and computes the effective field as seen from outside the system and does not compute the internal field of light. This double-adding model computation is shown in Figure 3.1 it can be seen that the computation here evaluates effective field strength fractions that are reflected at the top and fraction that is transmitted downward and the rest of the field is deduced to be as scattered and/or absorbed according to Equation (3.1) more details can be obtained from [32]. This model was later extended by [*Hansen (1971a, b)*] and [*Hovenier 1971*] to include polarization evaluation of the scattered light.

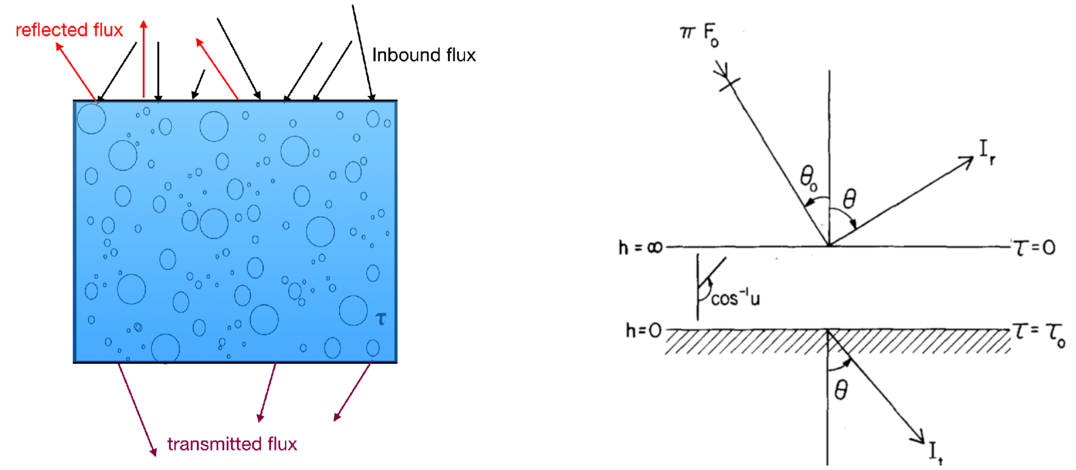

(a)

(b)

Figure 3.1: (a) The existing model evaluation of the atmosphere fields using a horizontally homogeneous layer, (b) Evaluation of the reflected and transmitted flux from zenith angle and optical thickness

$$\begin{aligned} \boldsymbol{I_r}(\mu,\phi) &= \mu_0 \boldsymbol{R}(\mu,\mu_0,\phi-\phi_0)\boldsymbol{F_0} \\ \boldsymbol{I_t}(\mu,\phi) &= \mu_0 \boldsymbol{T}(\mu,\mu_0,\phi-\phi_0)\boldsymbol{F_0} \end{aligned} \tag{3.1}$$

where $\boldsymbol{I_r}$ and $\boldsymbol{I_t}$ are the transmitted and reflected flux, and $\theta = \cos^{-1}\mu$, and for zenith angle of incidence at the top of the atmosphere $\theta_0 = \cos^{-1}\mu_0$, and μ is the cosine of angle with respect to the outward normal, + 1 (for the normal direction) to 0 (for the grazing direction) [32].

This brings the need to develop a model that computes the field internal to the system hence evaluating the internal field within clouds and haze layers. In the following section, the new radiative transfer forward model is discussed in detail. The model developed in this research shall compute the internal field of scattered and absorbed flux strengths as visualized in Figure 3.2 with a detailed photon path analysis. The atmosphere radiative transfer model can be classified into two parts, the first part is development of the atmospheric composition from optical properties of molecules and aerosols, and the second part is the development of a scattering probability phase function using the existing aerosol and molecular (gas) scattering matrix and compute the state of polarization for multiple scattering inside the atmosphere. The state of polarization is derived using Stoke's vector representation. The advantage of the new model developed in this research could be used to analyze the internal field (in-situ measurement) of any planetary atmosphere. In any case specific to that atmosphere structure the first part has to be individually developed and the second part of internal field evaluation shall remain the same for all cases.

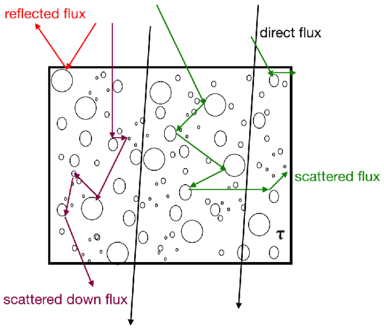

Figure 3.2: New forward model developed to compute the internal field in an atmosphere.

3.1. Forward Model Framework

As discussed the radiative transfer forward model consists of two parts, the first part is to model the atmosphere vertical structure from optical properties of the composition and second to compute the photon interaction in the atmosphere model and evaluate the internal field and polarization state using Stoke's vector. The atmosphere radiative transfer model consists of several layers and each layer is defined with certain optical properties derived from pressure, temperature, and composition of gas and aerosol in those layers. These optical properties constitute and construct a phase function that describes the photon-particle interaction in each layer. The Monte-Carlo technique is used to evaluate the scattering (position and direction) or photon transportation in the atmosphere and to compute the internal field. In the Figure 3.3 the development schema of the two parts of the forward model can be visualized, the first block shows how different layers are constructed and form a column with varying optical properties down the column, the second schema shows the internal field populated using the Monte-Carlo technique. In Figure 3.4 the forward scatter model software schema or flow design is shown:

3.1.1. Atmospheric radiative transfer model: Saturn

A standard atmospheric model is defined using pressure, density, and temperature as a function of altitude, these properties are related and governed by temperature profile. This is a simple method of atmospheric description without the consideration of complex chemical, thermodynamic and fluid dynamic cycles. Each layer is defined by certain optical properties, these properties depend on the composition of that layer and the particle column density $[\#/m^2]$. The optical properties are then used define the scattering phase function of these layers.

---

[1] Unified Modeling Language

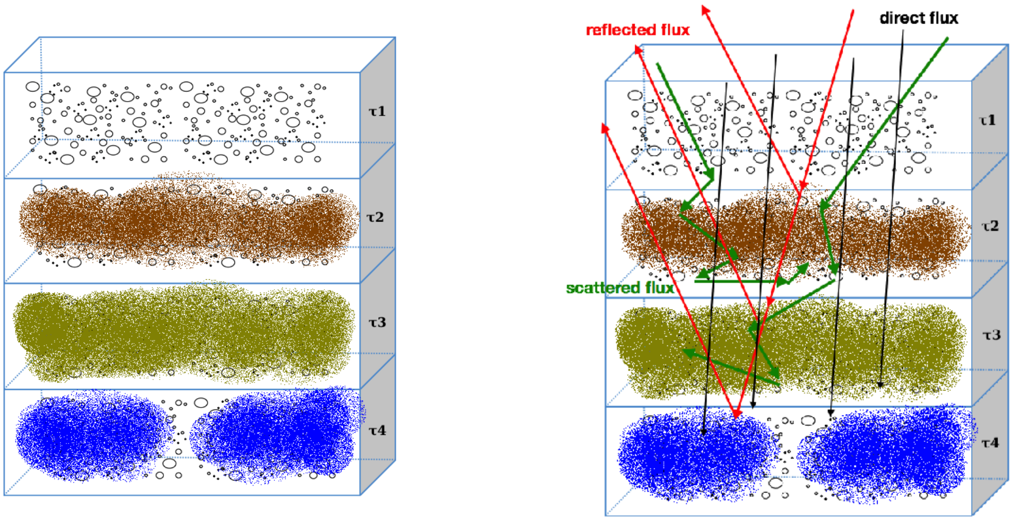

(a)

(b)

Figure 3.3: The forward model development schema a) Atmosphere model various layer properties are derived, b) The photon interaction using Monte-Carlo technique.

Saturn atmosphere model

Saturn's atmosphere has been studied by several flybys and remote sensing observations from Cassini and Hubble telescope. Without any in-situ probe measurements of the Saturn's atmosphere, it is difficult to understand the composition vertical structure of the lower layers due to a higher optical thickness of the upper cloud layers. For this, we have to rely on the data retrieved from remote observation using spectroscopy to quantitatively analyze its composition by developing several numerical models and laboratory experiments. The Figure 3.5a describes the presumed layer composition of gas giant's atmosphere as a comparison and Figure 3.5b describes Saturn's atmosphere from various observations. Saturn's atmosphere is mainly composed as of Hydrogen (H_2) and Helium (He) gases, From several observations, theoretical models, and experimental models its derived that small traces of Methane gas (CH_4), ammonia haze/clouds (NH_3), Phosphane (PH_3), and presumably Hydrogen Sulphide ice (H_2S) and water ice (H_2O) are present, but to validate these models remote sensing is insufficient, as lower layers of Saturn's atmosphere are present below the thick dense clouds. From several observation [30][18] the Saturn's atmosphere is predicted to have an ammonia haze layer in the stratosphere, and three main cloud layers in the troposphere, ammonia ice cloud (NH_3) at the top, and ammonium hydrosulfide ice cloud (NH_3SH) in between and a thick water ice cloud (H_2O) at the bottom as shown in the Figure 3.5b.

Model atmosphere definition

For the radiative transfer evaluation, the atmosphere is developed with each layer containing different gas, clouds and/or haze composition. The atmosphere model defined here has two top layers as stratosphere defined by hydrogen and helium gas and small traces of ammonia haze, with a particle size in the range of $0.1-0.3\mu m$. The troposphere is defined by the three cloud layers, ammonia ice cloud, ammonium hydrosulfide ice cloud and water ice cloud with a particle size in the range of $1-30\mu m$. The lowest layer is water ice in the frozen state particle size $> 30\mu m$. The mixing ratios of the gases by volume are as defined in Table 3.1. The gas mixture is taken to be composed of only Hydrogen and Helium for this simulation, as they form 98% of the gases found in Saturn, and Methane traces of 0.18% is used to simulate the methane absorption in the internal field. The graphical representation of the layers in a plane parallel model used for the simulation defined as a function of altitude is according to Figure 3.6:

Optical properties of Saturn's layers

The optical properties and the scattering matrices are needed to define the phase function of the layers in atmosphere model to compute the internal field and evaluate Stoke's vector. The optical properties are defined both for gas molecules and for aerosol, clouds or haze if present in those layers. The optical properties of the atmospheric model are defined in terms of the optical thickness ($b(\lambda)$) of the layer. The optical thickness is

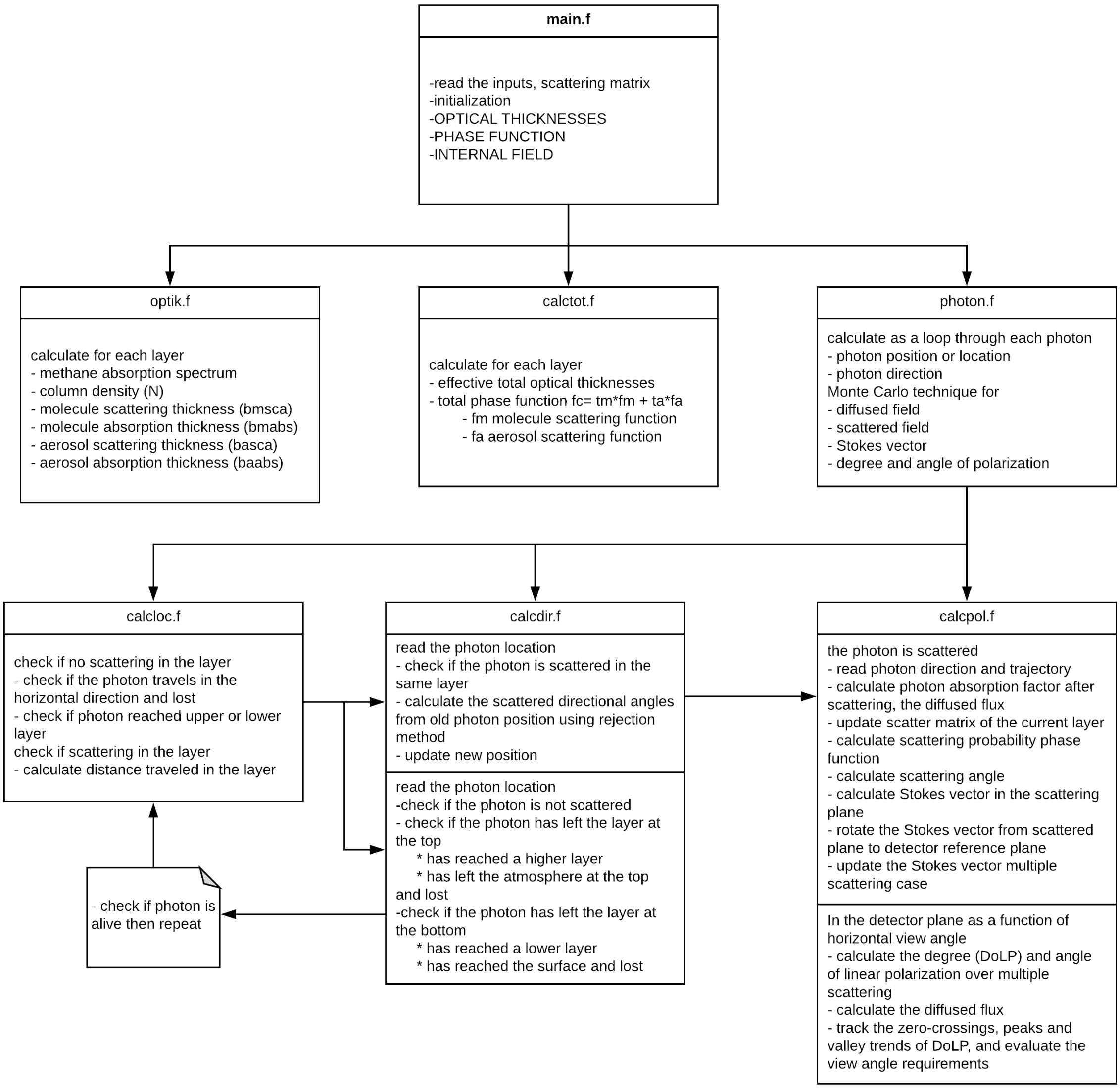

Figure 3.4: Forward model software schema and/or functional UML[1] chart.

governed by the column density ($\#/m^2$) and the total extinction cross section ($\sigma_{ext}(\lambda)$) for both the molecules and aerosol particles present in the layer. Further, the extinction cross-section can be defined as the sum of the absorption and scattering cross section of the particles. This is defined both for the gas molecules and the aerosol particles in each layer as discussed in the following sections.

The optical thickness of a layer is computed from the column density and the total extinction cross section as shown in Equation (3.2). These optical thicknesses are measured vertically,

$$\begin{aligned} b(\lambda) &= N\sigma_{ext}(\lambda) \\ b(\lambda) &= N_m\left[\sigma^m_{abs}(\lambda)+\sigma^m_{sca}(\lambda)\right]+N_a\left[\sigma^a_{abs}(\lambda)+\sigma^a_{sca}(\lambda)\right] \\ b(\lambda) &= b^m_{abs}(\lambda)+b^m_{sca}(\lambda)+b^a_{abs}(\lambda)+b^a_{sca}(\lambda) \end{aligned} \tag{3.2}$$

where, $b(\lambda)$ is the total extinction cross section,
N_m and N_a are the column densities of gas molecule and aerosol respectively,
σ^m_{abs} and σ^a_{abs} are the absorption cross sections of gas molecule and aerosol respectively,
σ^m_{sca} and σ^a_{sca} are the scattering cross sections of gas molecule and aerosol respectively

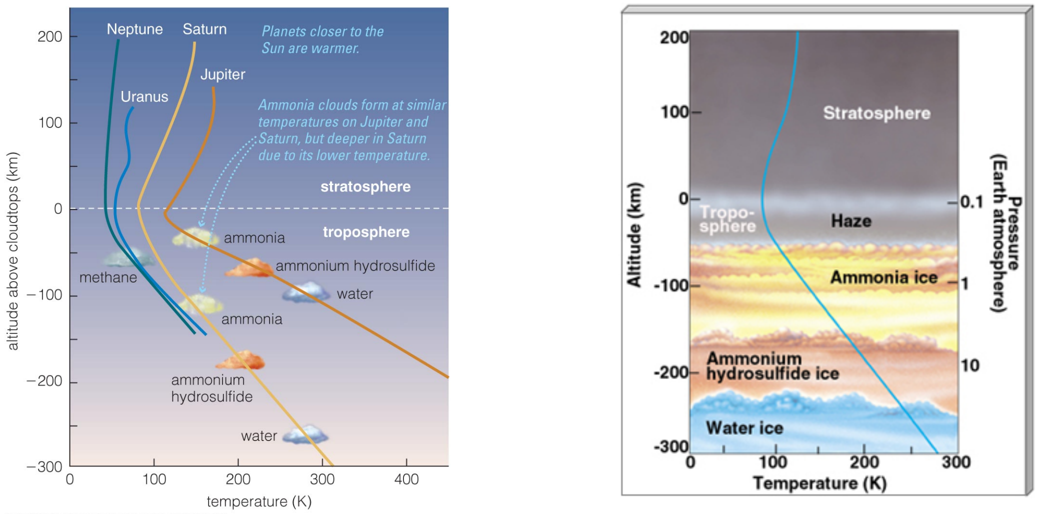

(a) Gas-Giants presumed atmospheric layer composition.

(b) Saturn's presumed atmosphere as a function of altitude [2].

Figure 3.5: Presumed atmosphere models of (a) Gas Giants and (b) Saturn's atmosphere as a function of altitude

Saturn's Atmosphere	
Atmospheric composition (by volume, Uncertainty)	
Major (%)	Hydrogen (H_2) 96.3% (2.4%)
	Helium (He) 3.25% (2.4%)
Minor (ppm)	Methane (CH_4) - 4500 (2000)
	Ammonia (NH_3) - 125 (75)
	Hydrogen Deuteride (HD) - 110 (58)
	Ethane (C2H6) - 7 (1.5)
Aerosols	Ammonia ice (NH_3)
	Ammonia hydrosulfide(NH_3SH)
	water ice (H_20)
Pressure towards the core	»1000 bar
Density at 1 bar	~0.19 kg/m3
Scale height	59.5 km
Temperature at 1 bar	134 K (-139 C)
Temperature at 0.1 bar	84 K (-189 C)
Wind speeds (surface)	Up to 400 m/s (30 degrees latitude) Up to 150 m/s (>30 degrees latitude)
Mean molecular weight	2.07 g/mol

Table 3.1: A summary of Saturn's atmosphere from fly-by and remote observations [Conrath et al. (1998) and Fletcher et al. (2007a)]

Gas column density
The column density for the gas molecules for each layer is evaluated using the hydrostatic equilibrium equation and the gas molecules mixing ratios of H_2(96.3%),He(3.25%), and CH_4(0.18%) are taken as shown in the Table 3.1.

$$N_m = \frac{P_{bottom} - P_{top}}{m \cdot g} \tag{3.3}$$

where P_{bottom} is the pressure at the bottom of the layer [Pa], P_{top} is the pressure at the top of the layer [Pa], m is the mass of gas composition [kg]', g is the local acceleration of gravity [m/s2].

$$m = \frac{\sum r_i M_i}{N_A} \tag{3.4}$$

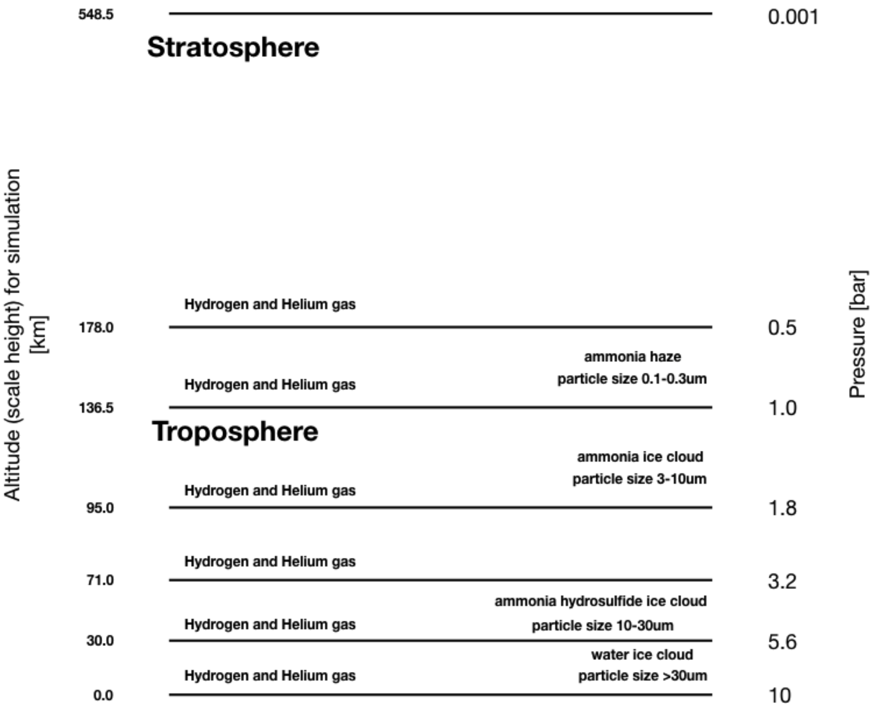

Figure 3.6: Saturn's atmosphere plane parallel model for scattering Monte-Carlo simulations.

where, r_i is the mixing ratio of a gas molecule [fraction *dimensionless*], M_i is the molar mass of the gas [kg/mol], N_A is the Avogadro number 1 mol = 6.022×10^{23} atoms

The pressures and temperature values are taken from *Stam et.al*, [67], (these model adapted the pressures from Lindal 1992, supplemented from 1.0 to 5.623 bars by data from West et al. 1986). Further, the pressure and temperature curve were interpolated assuming a dry adiabatic process to obtain temperature values down to 10 [bar]. The P-T curve for Saturn's atmosphere is as shown in the Figure 3.7. The column density of each layer is evaluated for both the gas and aerosol particles as a function of pressure and the results are presented in Table 3.2

layer	P_{top} [Pa]	P_{bottom} [Pa]	N_m [$\#/m^2$]	N_a [$\#/m^2$]	T_{bottom} [K]
1[1]	10^2	$0.5623 \cdot 10^5$	$2.729 \cdot 10^{30}$	0.0	112.7
2[2]	$0.5623 \cdot 10^5$	$1.0 \cdot 10^5$	$2.125 \cdot 10^{30}$	$1.647 \cdot 10^{29}$	134.8
3[3]	$1.0 \cdot 10^5$	$1.778 \cdot 10^5$	$3.777 \cdot 10^{30}$	$2.927 \cdot 10^{29}$	162.3
4[4]	$1.778 \cdot 10^5$	$3.162 \cdot 10^5$	$6.719 \cdot 10^{30}$	0.0	194.6
5[5]	$3.162 \cdot 10^5$	$5.623 \cdot 10^5$	$1.195 \cdot 10^{31}$	$3.086 \cdot 10^{29}$	233.3
6[6]	$5.623 \cdot 10^5$	$10.0 \cdot 10^5$	$2.125 \cdot 10^{31}$	$1.557 \cdot 10^{30}$	279.17

Table 3.2: Column number density for gas particles in Saturn's atmosphere model

---

[1] Layer 1 = gas layer (178-550km)

[2] Layer 2 = ammonia haze layer (136-178km)

[3] Layer 3 = ammonia ice cloud layer (95-136km)

[4] Layer 4 = no aerosol, gas layer (71-95km)

[5] Layer 5 = ammonia hydrosulfide layer (30-71km)

[6] Layer 6 = water ice cloud layer (0-30km)

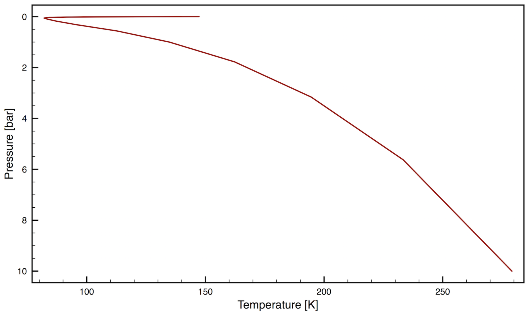

Figure 3.7: Pressure versus temperature curve for Saturn's atmosphere

Particle distribution

The ensemble of the particles is according to two-parameter gamma size distribution function Equation (3.5).

$$
\begin{aligned}
n(r) &= C \cdot r^{\left(\frac{1}{v_{eff}}-3\right)} \cdot e^{\left(\frac{-r}{v_{eff} \cdot r_{eff}}\right)} \\
C &= \frac{1}{\left(r_{eff} \cdot v_{eff}\right)^{\frac{1}{v_{eff}}-2}} \times \text{gammaln}\left(\frac{1}{\mathrm{v_{eff}}}-2\right)
\end{aligned}
\tag{3.5}
$$

where, r_{eff}, v_{eff} are the effective particle radius and variance of the size distribution, 'gammaln' is a gamma function that returns the value of the natural logarithm of the argument.

Molecular Scattering thickness

The molecular scattering cross sections for the gas particles are computed in a similar way defined in the paper [67], The molecular scattering cross section (σ_{sca}^{m}) is defined by the equation Equation (3.6) and the cross-sections are refractive indices dependent and in turn, the refractive index is wavelength dependent. The wavelength dependent refractive index (n_i) for Hydrogen is evaluated first using the dispersion curve equation (r_i) Equation (3.7) [15].

$$
\sigma_{sca}^{m}(\lambda) = \frac{24\pi^2}{N_L^2} \frac{\left(n^2-1\right)^2}{\left(n^2+2\right)^2} \frac{(6+3\delta)}{(6-7\delta)} \frac{1}{\lambda^4}
\tag{3.6}
$$

Where, n is wavelength dependent refractive index of gas particle,
N_L is the Loschmidt's number (1 amagat = $2.5474310^{25} m{-}3$ at 273.15 K and 1013.25 hPa),
δ is the depolarization constant and is kept at 0.02 for hydrogen and neglecting the wavelength dependence.

$$
\begin{aligned}
r_i &= 1 + A + \frac{AB}{\lambda^2} \\
n_i &= \frac{(r_i^2-1)^2}{(r_i^2+2)^2}
\end{aligned}
\tag{3.7}
$$

where the constants A and B are defined for hydrogen, A = 13.5810^{-5} and B= 7.5210^{-3} [15]

The molecular scattering thickness for individual layer composition is presented in the Figure 3.8a. It is seen from the optical thickness plot that the scattering cross section is very high at the lower wavelength region and decreases rapidly at a higher wavelength and turns close to zero at infrared wavelengths for most of the layers.

Stam et.al, [67] computed the molecular scattering thickness (b_{sca}^{m}) to decrease from 21.47 at $0.4\mu m$ to 0.51 at $1.0\mu m$ (at 5.623 [bar]) in Jupiter atmosphere. Similar results were obtained with the current research work for Saturn's atmosphere model, and obtained the molecular scattering absorption thickness to decrease from 22.62 at $0.4\mu m$ to 0.536 at $1.0\mu m$ (at 5.623 [bar]).

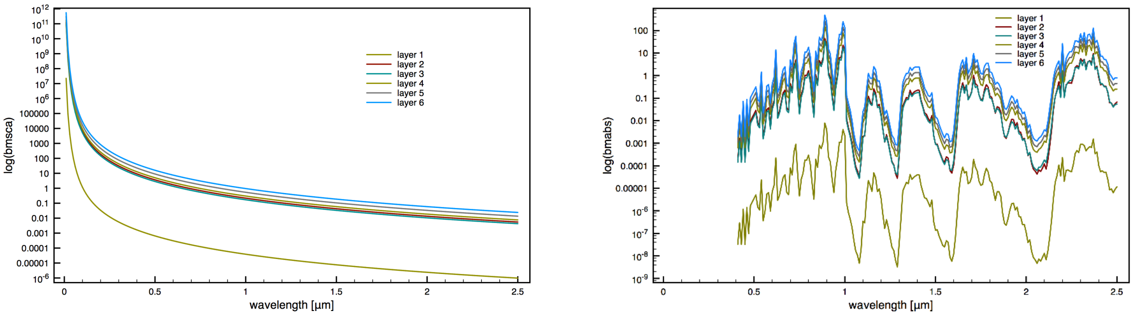

(a) (b)

Figure 3.8: (a) gas molecule scattering cross section (b^m_{sca}), (b) gas molecule absorption cross section (b^m_{abs}) for Saturn's atmosphere

Molecular Absorption thickness

$$b^m_{abs}(\lambda) = N_m\, \sigma^m_{abs}(\lambda) \tag{3.8}$$

The molecular absorption is highly influenced by the presence of methane in the Saturn's atmosphere, a potent greenhouse gas. The mixing ratio of the methane gas is taken as 0.18% like that of Jupiter atmosphere from [67] and the (b^m_{abs}) from Karkoschka are adapted to these values as described in the later sections Equation (3.9). The methane absorption's influence the infield flux in the near infrared wavelength region for the giant planet's. To compute the molecular absorption cross sections of methane over a wide wavelength range (0 - 2.5μm) the methane k distribution coefficients from Karkoschka and Tomasko (2010) are used.

The absorption line by line data is complicated to obtain for methane at the near-infrared region in order to model the spectra of these planet's. These line by line data analysis is complicated and as no database is available yet. In order to model the methane absorption in the near infrared wavelength regions, a band fit data model can be used and this is where the k-coefficients come to aid. In this k distribution, the band model parameters are fitted to measure transmission spectra of methane at the laboratory and recorded over various temperatures, pressures and path lengths appropriate to outer planet atmospheres. One such set of band model parameters (for self-broadening conditions only) is from Karkoschka and Tomasko (2010) and k- distribution parameters that were fitted to these data by Irwin et al. (1996). The band fitted k-table is represented and evaluated in $(km - amagat)^{-1}$ easier to have it in this units as the laboratory experiments are conducted with path lengths appropriate to those planet's. The current research defines the path length for absorption and scattering in $(\#/m^2)$ units. The path lengths from k-distribution are converted using the Loschmidt constant ($1amg = N_L = 2.687 \cdot 10^{25} m^{-3}$ at 273.15 K and 1013.25 hPa) to fit the values to our current forward model units. The methane absorption spectrum using the band fitted k-coefficients is shown in Figure 3.9. Following the methane absorption band fitted k-coefficients, the absorption cross sections for gas particles as a function of wavelength for 0.1 to 2.5μm are derived as shown in Figure 3.8b .

$$b^m_{abs} = \sum w_i \cdot \kappa_i(\lambda) \cdot \frac{N_m}{N_L} \cdot 10^{-3} \tag{3.9}$$

where, w is the mixing ratio of methane in each layer, $\kappa(\lambda)$ is the k-coefficient and, $N_m/N_L \cdot 10^{-3}$ is to convert the $(km - amagat)^{-1}$ to $(\#/m^2)$

The methane absorption and transmission spectrum for the Saturn's atmosphere are derived at different wavelengths for each layer and is presented in Figure 3.10d. A similar absorption spectrum was derived by Stam et.al, [67] for Jupiter's atmosphere up to the visible wavelength region. In this research similar technique is used to derive the methane absorption spectrum for Saturn and is further extended up to 2.5μm wavelength range using the previously mentioned band fitted k distribution-coefficients.

---

[1] Transmitted flux (TF) out of each layer (layers 1 - 5)

[2] Absorbed flux (AF) in each layer (layers AF 1 - 5)

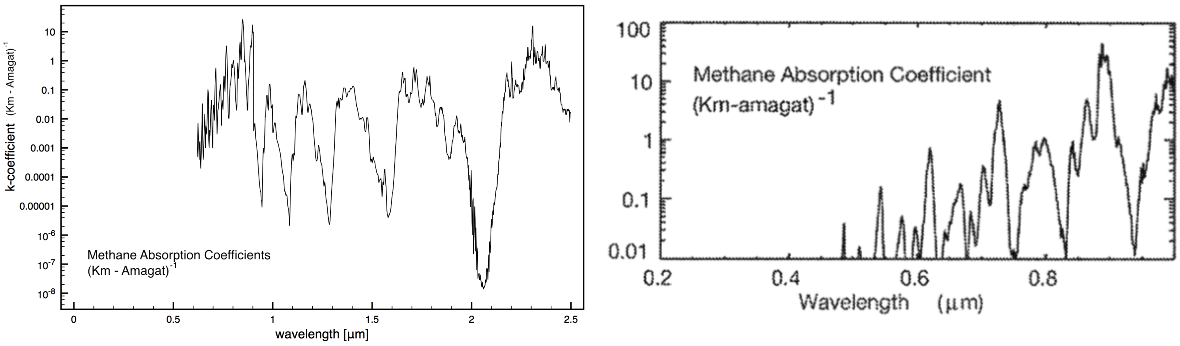

Figure 3.9: (a) Methane absorption spectrum band fitted k-coefficients from the current model for Saturn. (b) Methane absorption spectrum for wavelength $0 - 1.0 \mu m$ derived by West et, al using Karkoschka's table for Jupiter [73]

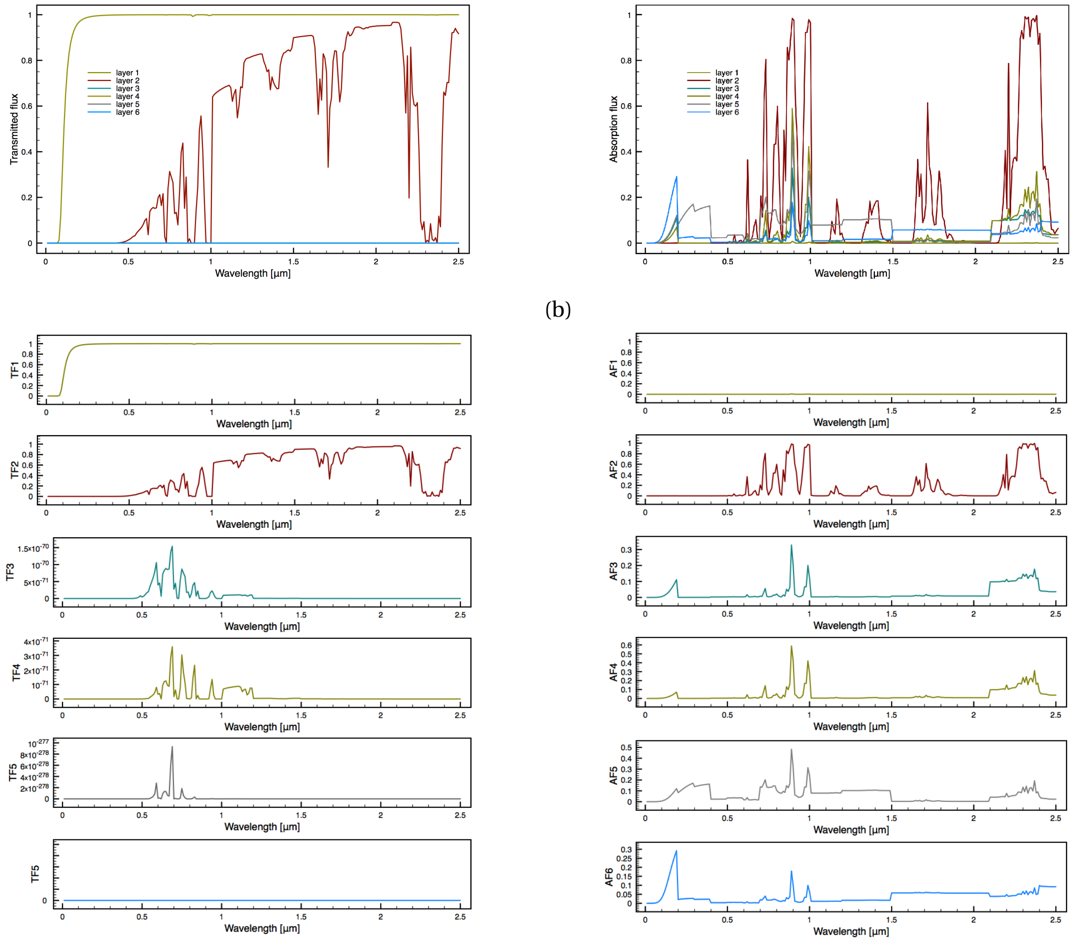

(a) (b)

(c) (d)

Figure 3.10: (a & c) and Saturn's atmosphere transmission flux (TF1-5)^{i} of each plane parallel layer , (b & d) absorption spectrum (AF1-5)^{ii} of Saturn's atmosphere at each layer

Aerosol Scattering and Absorption thickness

The optical thickness of the aerosol particles is user-defined. The aerosol optical absorption and scattering thicknesses are similar to the molecular optical thickness and are derived using the complex refractive index of the aerosol. In this research, scattering & absorption cross sections are derived based on the Meerhof Mie program [34].Wavelength, complex refractive index and particle size distribution (mean radius and variance) are the variables used by the Meerhof program and evaluates the scattering matrix from these parameters, this also include the extinction cross sections. These variables for Saturn's model are summarized in Table 3.3.

gases	**Hydrogen** (H_2)								**Helium (He)**								**Methane** (CH_4)							
Re(m)	1.000138 - 1.000135								1.00003484 - 1.00003469								1.0004259 - 1.0004360							
r_{eff} (in μm)	0.005–0.1 [μm] [52]								0.005–0.1 [μm] [52]								0.005–0.1 [μm] [52]							
v_{eff}	0.001								0.001								0.01							
Haze, cloud and aerosol particles																								
Wavelength (μm)	***0.1***	***0.2***	***0.3***	***0.4***	***0.5***	***0.6***	***0.7***	***0.8***	***0.9***	***1.0***	***1.3***	***1.6***	***1.9***	***2.2***	***2.5***	***2.8***	***3.1***	***3.4***	***3.7***	***4.0***	***4.3***	***4.6***	***4.9***	***5.0***
ammonia haze [43]																								
Re(m)	1.54	1.792	1.505	1.449	1.439	1.428	1.423	1.418	1.412	1.420	1.408	1.406	1.403	1.402	1.393	1.313	1.458	1.428	1.409	1.406	1.398	1.394	1.385	1.385
abs(Im(m)) ($\times 10^{-5}$)	550.4	0.001592	0.002387	0.02109	0.028	0.034	0.03963	0.043	0.05	0.0507	0.05817	0.1857	0.2402	39.79	49.74	694.0	2125	130.5	58.95	61.21	69.2	12.66	318.3	318.3
r_{eff} (in μm)	0.3 [μm] (particle distribution 0.1-1[μm])																							
v_{eff}	0.1 ± 0.01																							
ammonia ice cloud [43]																								
Re(m)	1.54	1.792	1.505	1.449	1.439	1.428	1.423	1.418	1.412	1.420	1.408	1.406	1.403	1.39	1.38	1.33	1.5	1.47	1.46	1.46	1.45	1.45	1.45	1.45
abs(Im(m)) ($\times 10^{-3}$)	55040	0.1592	0.2387	2.109	2.8	3.4	3.963	4.3	5.0	5.07	5.817	18.57	24.02	4.03	1.44	7.21	30.8	6.86	1.51	2.50	0.124	1.47	0.292	0.292
r_{eff} (in μm)	5 [μm] (particle distribution 1-10[μm])																							
v_{eff}	0.02																							
ammonium hydrosulfide ice cloud amorphous [37]																								
Re(m)	2.236	2.237	2.238	2.239	2.24	2.238	2.236	2.234	2.242	2.235	2.23	2.2	2.2	2.2	2.2	2.18	2.12	2.19	2.82	2.58	2.51	2.5	2.42	2.48
abs(Im(m)) ($\times 10^{-3}$)	1.2	1.1	1	0.4	0.2	0.1	0.6	0.8	0.4	1.0	1.8	0.01	0.01	0.329	0.303	3.04	79.1	537.0	297.0	33.1	0.684	0.246	5.66	0.944
r_{eff} (in μm)	10 [μm] (particle distribution 10-30[μm])																							
v_{eff}	0.1																							
water haze/ice cloud [72]																								
Re(m)	1.4032	1.3938	1.3339	1.3194	1.3130	1.3094	1.3069	1.3049	1.3032	1.3015	1.2961	1.2893	1.2780	1.2620	1.2258	1.0850	1.4409	1.5053	1.4005	1.3620	1.3414	1.3460	1.3347	1.3290
abs(Im(m)) ($\times 10^{-6}$)	312730	0.015	0.0055	0.0027	0.0019	0.0057	0.029	0.134	0.42	1.62	13.2	353.65	410.8	265.0	925.0	30154	581630	38722	7196.7	9622.6	17578	26888	12995	12000
r_{eff} (in μm)	30 [μm] (particle distribution >30[μm])																							
v_{eff}	0.1																							

Table 3.3: Mie scattering matrix input variables for Saturn's atmosphere, where Re(m) and Im(m) are real and imaginary parts of refractive index, r_{eff} (in μm) is the effective particle radius, and v_{eff} is effective variance of the particle size distribution (dimensionless).

The extinction cross sections for the aerosol particles are presented as a function of wavelength for each layer in Figure 3.11

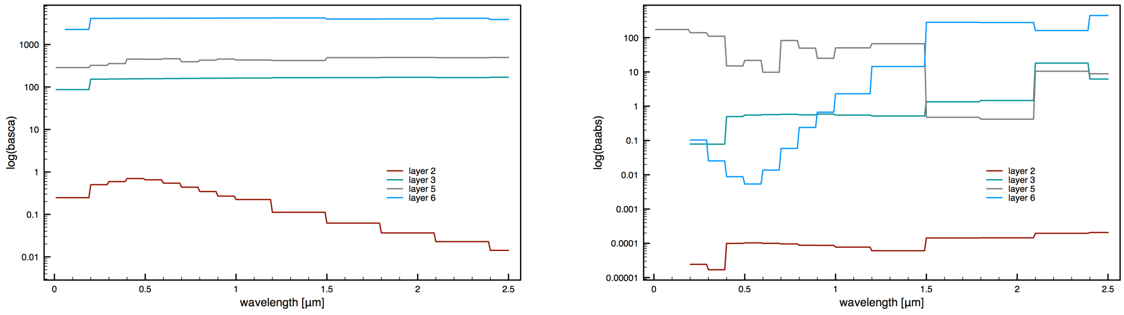

(a) (b)

Figure 3.11: (a) aerosol scattering cross section (b^a_{sca}), (b) aerosol absorption cross section (b^a_{abs}) for Saturn's atmosphere

Single scattering albedo

From the molecule and aerosol scattering thickness, the single scattering albedo can be derived according to Equation (3.10).

$$a = \frac{b^m_{sca} + b^a_{sca}}{b^m_{sca} + b^m_{abs} + b^a_{sca} + b^a_{abs}} \tag{3.10}$$

Single scattering albedo is the ratio of scattering efficiency to the total extinction efficiency. A value of one means the photon flux attenuates due to scattering and a value of zero means the attenuation is due to absorption. The single scatter albedo for the atmosphere model in this research is presented in the Figure 3.12

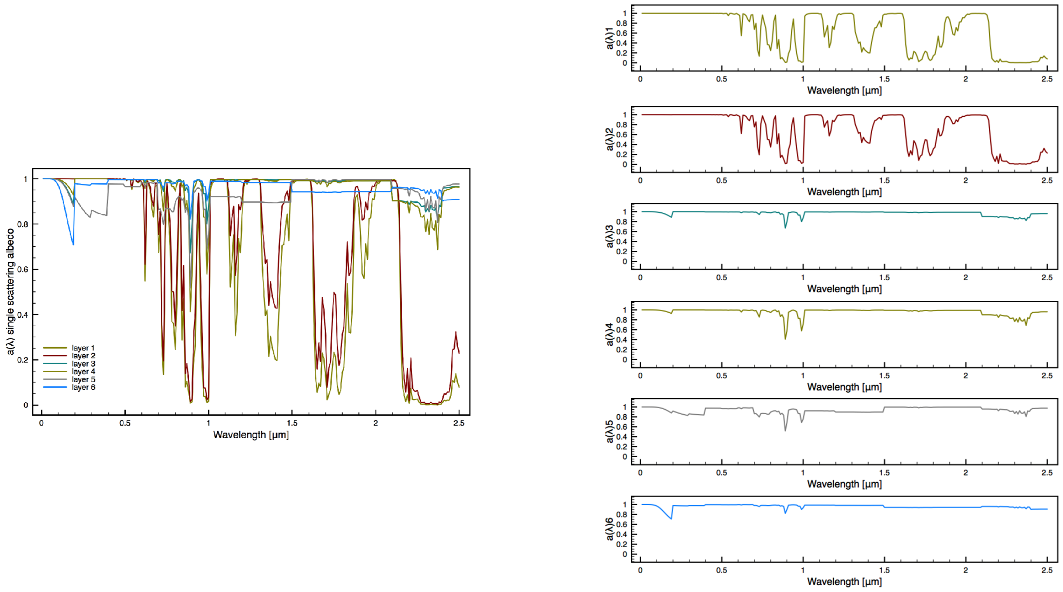

(a)

(b)

Figure 3.12: Saturn's atmosphere single scatter albedo ($a(\lambda)$) for each layer

Total Phase function

Scattering matrices are introduced here before moving ahead with the evaluation of the internal field.There are three types of atmospheric scattering that are possible, Rayleigh scattering, Mie-scattering only for the spherical particles and non-selective/geometric scattering. The type of scattering can be related to the particle size ($2\pi R$) in comparison to the incident wavelength (λ) defined by Equation (3.11).

$$k = \frac{2\pi R}{\lambda} \tag{3.11}$$

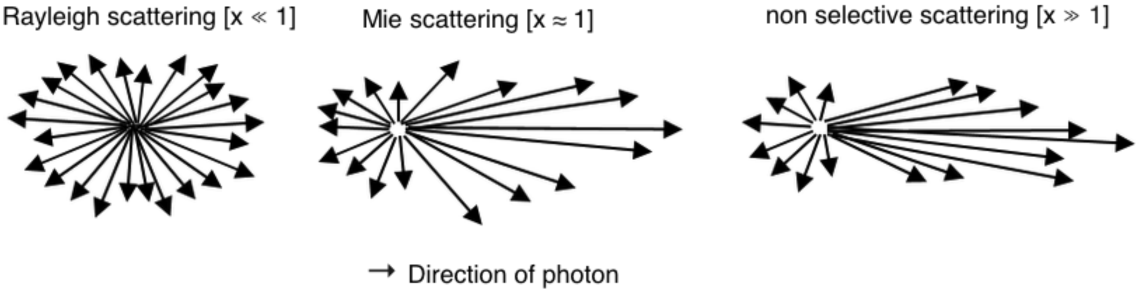

Figure 3.13: 1. Rayleigh scattering $k \ll 1$ 2. Mie scattering $k \approx 1$ 3. Non selective scattering $k \gg 1$.

Rayleigh scattering is due to the gas molecules in the atmosphere and is the simplest form of scattering, this type of scattering occurs when $k \ll 1$. Mie-scattering is for only spherical particles and this type of scattering occurs when $k \approx 1$. The third type of scattering occurs at the lower layers of the atmosphere where the particle size is much higher than the incident wavelength, the scattering is independent of the wavelength, this type of scattering occurs when $k \gg 1$. Aerosols are the highest contributors to scattering, the aerosol can be defined by naturally occurring dust, volcanic eruptions, and black carbon from man-made as in Earths atmosphere. The clouds appear white or brighter due to scattering, the cloud-aerosol particles if larger in size to the incident wavelength, the cloud-aerosol scatters all wavelength and hence appear white.

Scattering matrices define all states of polarization possible for a scattering event, it forms a general phase matrix for scattering aerosols. That is the scattering matrix defines the relation between the initial and final state of a scattering event in the physical system. The scattering matrix is generally used to interpret the multi-angle and multi-spectral behavior of the particle during scattering.

$$F(\Theta) = \begin{bmatrix} F_{11}(\Theta) & F_{12}(\Theta) & F_{13}(\Theta) & F_{14}(\Theta) \\ F_{21}(\Theta) & F_{22}(\Theta) & F_{23}(\Theta) & F_{24}(\Theta) \\ F_{31}(\Theta) & F_{32}(\Theta) & F_{33}(\Theta) & F_{33}(\Theta) \\ F_{41}(\Theta) & F_{42}(\Theta) & F_{43}(\Theta) & F_{44}(\Theta) \end{bmatrix} \tag{3.12}$$

The Meerhof program is used to evaluate the scattering matrices of a sample of homogeneous spherical particles of varying radii using a two-parameter gamma size distribution function Equation (3.5).

The scattering matrix consists of 16 elements F_{ij} with i, j=1..4 (see [24] for more). The elements of the matrix depend on the physical properties, such as effective particle size variance, complex refractive index of the scattering element and the wavelength of radiation [34]. The scattering angle defines the direction of interest and scattering intensity of the particle oriented in this direction. For isotropic and spherical particle's the matrix elements further reduce with $F_{11} = F_{22}$ and $F_{33} = F_{44}$[33]. The Stoke's parameter $\pm Q$ is defined by the upper block elements of the matrix and the conversion to circular polarization from linear polarization at ±45° is defined by the lower block elements of the scattering matrix. The degree of linear polarization for unpolarized incident light is defined by $-F_{12}/F_{11}$.

$$F(\Theta) = \begin{bmatrix} F_{11}(\theta) & F_{12}(\theta) & 0 & 0 \\ F_{12}(\theta) & F_{22}(\theta) & 0 & 0 \\ 0 & 0 & F_{33}(\theta) & F_{34}(\theta) \\ 0 & 0 & -F_{43}(\theta) & F_{44}(\theta) \end{bmatrix} \tag{3.13}$$

The scattering matrix is normalized according to:

$$\frac{1}{4\pi} \int_0^{4\pi} F_{11}(\Theta, \lambda)\, d\Omega = 1 \tag{3.14}$$

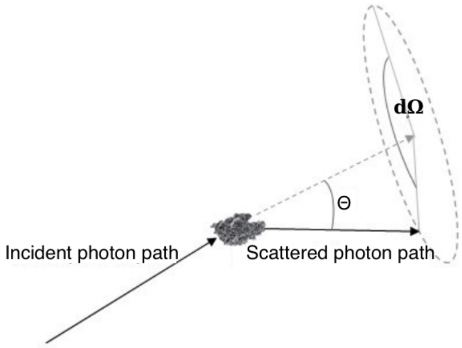

Figure 3.14: Scattering angle and solid angle represented in the scattering plane [20].

with Θ being the scattering angle and $d\Omega$ being the solid angle see Figure 3.14. The above equation can also be represented as:

$$\frac{1}{\pi}\int_0^{\pi} F_{11}\left(\Theta,\lambda\right)\sin\Theta d\Theta = 1 \tag{3.15}$$

The total phase function for each layer is defined using the optical thickness of molecule and aerosol present in that layer according to Equation (3.16).

$$\begin{gathered} F_C = \tau_M F_M + \tau_A F_A \\ \tau = b^m_{sca} + b^m_{abs} + b^a_{sca} + b^a_{abs} \\ \tau_M = \frac{b^m_{sca}}{\tau},\ \ \tau_A = \frac{b^a_{sca}}{\tau} \end{gathered} \tag{3.16}$$

where, F_M and F_A are the molecular and aerosol scattering matrix

For the layers with more than one aerosol type the scattering matrices shall be combined according to Equation (3.17).

$$\begin{gathered} F_{A_{tot}} = \tau_{A1} F_{A1} + \tau_{A2} F_{A2} \\ \tau_A = b^{a1}_{sca} + b^{a2}_{sca} \\ \tau_{A1} = \frac{b^{a1}_{sca}}{\tau_A},\ \ \tau_{A2} = \frac{b^{a2}_{sca}}{\tau_A} \end{gathered} \tag{3.17}$$

where, F_{A1} and F_{A2} are the aerosol 1 and aerosol 2 scattering matrix in that layer

3.1.2. Atmospheric radiative transfer model: Venus

The Venus's atmosphere had been elaborately studied by the Pioneer Venus's mission, Pioneer descent probes, and Venera mission. Venus's atmosphere has a 92 bar pressure and a temperature of 737 K at the bottom-most layer and has very thick clouds of a sulfuric acid solution in the 45-70Km altitude range, as can be seen from the vertical structure of Venus's atmosphere in Figure 3.15a. The Venus's atmosphere is mostly composed of carbon dioxide (96%) and Nitrogen (3.5%) also other traces of gas are found but form less than 0.01%, A summary of the Venus's atmosphere deduced from various grounds based observations, remote sensing, in-situ measurements at Venus's from pioneer mission, pioneer descent probes, and Venera descent probes is presented in Table 3.4

Venus's Atmosphere	
Atmospheric composition (near surface, by volume)	
Major (%)	Carbon dioxide (CO_2) 96.5%
	Nitrogen (N_2) 3.5%
Minor (ppm)	Sulphur dioxide (SO_2) 150
	Argon (Ar) 70
	Water (H_2O) 20
	Carbon monoxide (CO) 17
	Helium (He) 12
	Neon (Ne) 7
Surface pressure	92 bar
Surface density	~65 kg/m3
Scale height	15.9 km
Total mass of atmosphere	~ 4.8×10^{20} kg
Average temperature	737 K (464 1C)
Diurnal temperature range	~0
Wind speeds (surface)	0.3–1.0 m/s (surface)
Mean molecular weight	43.45 g/mol

Table 3.4: A summary of Venus's atmosphere from Pioneer and Venera descent probes [68]

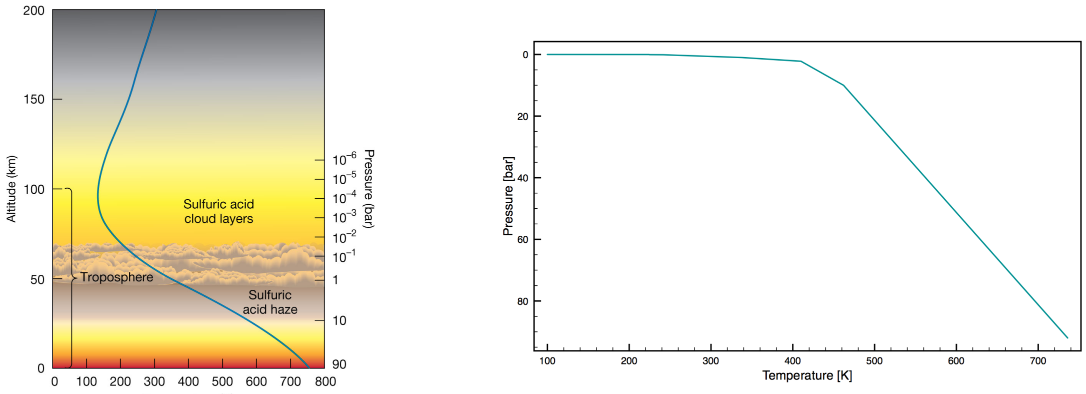

(b)

(a)

Figure 3.15: Venus's atmosphere a) Venus's vertical atmosphere structure. [adapted from: [4]], b)Pressure versus temperature curve for Venus's atmosphere.

Optical properties of Venus's layers

The optical properties of Venus's atmosphere are reasonably well known from the remote and in-situ observations with Venus's multiprobe missions. The plane-parallel atmosphere is as defined in Figure 3.16, the clouds are mostly composed of sulfuric acid H_2SO_4 solution, the clouds have a composite structure in the troposphere, and are mainly classified as Upper haze at 65-70 [km], upper cloud at 60-65 [km], middle cloud

layer	P_top [Pa]	P_bottom [Pa]	N_m [$\#/m^2$]	N_a [$\#/m^2$]	P_bottom [K]
1	1	$0.019 \cdot 10^5$	$2.53 \cdot 10^{27}$	$6.75 \cdot 10^{27}$	224
2	$0.019 \cdot 10^5$	$0.07 \cdot 10^5$	$6.8 \cdot 10^{27}$	$3.33 \cdot 10^{27}$	225
3	$0.07 \cdot 10^5$	$0.1 \cdot 10^5$	$4.002 \cdot 10^{27}$	$1.96 \cdot 10^{27}$	242
4	$0.1 \cdot 10^5$	$1 \cdot 10^5$	$1.2 \cdot 10^{29}$	$5.88 \cdot 10^{28}$	338
5	$1 \cdot 10^5$	$2.2 \cdot 10^5$	$1.6 \cdot 10^{29}$	$7.84 \cdot 10^{28}$	410
6	$2.2 \cdot 10^5$	$10.0 \cdot 10^5$	$1.04 \cdot 10^{30}$	$5.1 \cdot 10^{29}$	462
7	$10.0 \cdot 10^5$	$92.0 \cdot 10^5$	$1.094 \cdot 10^{31}$	$2.92 \cdot 10^{31}$	736

Table 3.5: Column number density for gas particles in Venus's atmosphere model

at 50-60 [km], lower cloud at 40-50 [km], and lower sulfuric acid haze at 30-40 [km] [39].

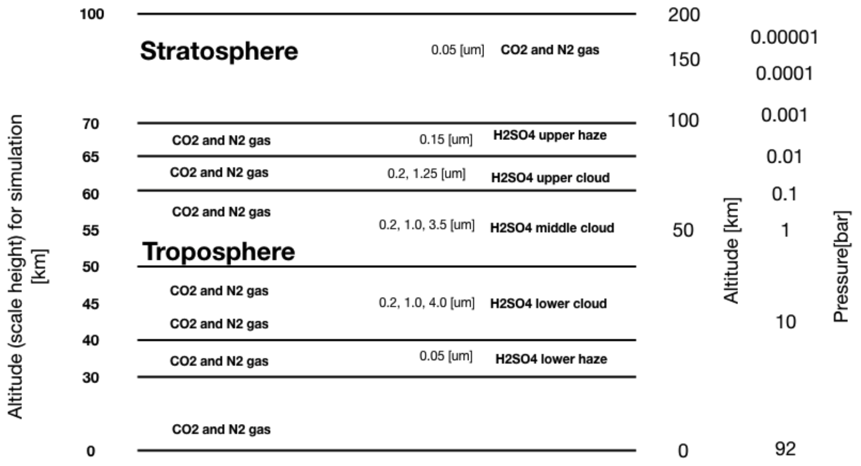

Figure 3.16: Venus's atmosphere plane parallel model as a function of altitude.

Molecular Scattering thickness

The optical thickness of each layer is taken for the simulations that are deduced from the Pioneer Venus's experiment by Knollenberg et.al [39] and are presented in Table 3.6 at 630nm wavelength . The CO_2 absorption spectrum is very minimal in the visible wavelength region in which our nephelometer measures, and hence are neglected for the current research. In the current research, the layers with aerosols the molecular optical thickness (b^m_{sca}) are considered negligible, the molecular scattering is evaluated as described in Equation (3.6) and the molecular scattering cross sections for Venus are presented in Figure 3.17 , and layer with just gas particles the aerosol optical thickness (b_{aer}) is negligible.

Aerosol Scattering and Absorption thickness

The extinction cross sections for the aerosol particles in Venus's atmosphere are presented as a function of wavelength for each layer in Figure 3.11 evaluated based on the Meerhof Mie program for scattering matrix, and the Table 3.7 variable used for the Venus's atmosphere to generated these phase function and optical properties.

According to Knollenberg the aerosol or cloud particle composition broadly classified into 3 modes, with mode 1 comprising of just H_2SO_4 particles, mode 2 contains H_2SO_4 + contamination, here contamination means the presence of other chemical species as direct condensates that contribute largely to the total mass in that layer, and mode 3 contains H_2SO_4 + contamination + crystal, here these are predicted to be sulfates or chloride crystals deduced from the best fit method of refractive index. From the observed data of the cloud

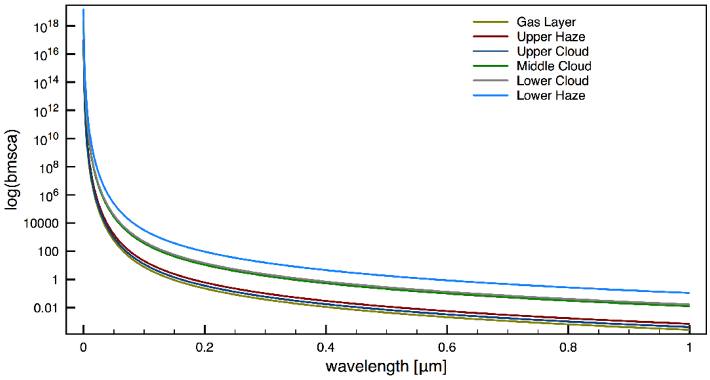

Figure 3.17: Venus's atmosphere, gas molecule scattering cross sections b^m_{sca} as a function of wavelength.

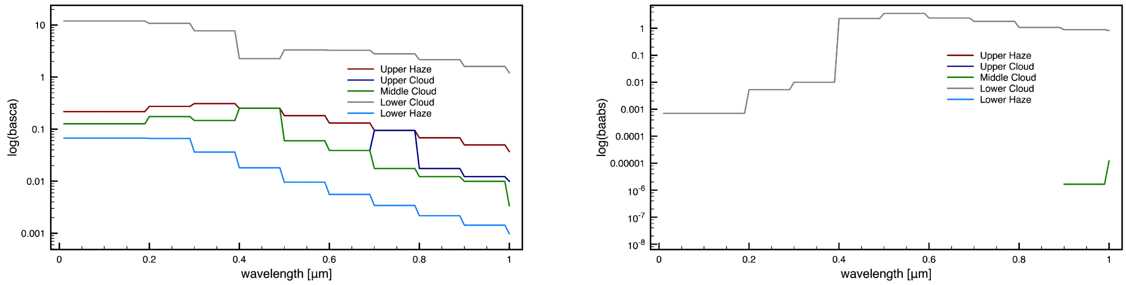

(a)

(b)

Figure 3.18: (a) aerosol scattering cross section (b^a_{sca}), (b) aerosol absorption cross section (b^a_{abs}) for Venus's atmosphere

Optical properties of Venus's atmosphere layers from Knollenberg et.al [39]				
	b^m_{sca}	b^m_{abs}	b_{aer}	a_{aer}
Stratosphere (70-100 [km])	0.01	0.0	0.01	0.1
Troposphere				
Upper haze and cloud (65-70 [km]) sulfuric acid haze	0.0017	0.0	8.5	0.1
Upper cloud (60-65 [km]) sulfuric acid cloud	0.0047	0.0	5.23	0.1
Middle cloud (50-60 [km]) sulfuric acid cloud	0.0027	0.0	8.35	0.1
Lower cloud (40-50 [km]) sulfuric acid cloud	0.08	0.0	4.87	0.1
Lower Haze (30-40 [km]) sulfuric acid cloud	0.11	0.0	1.36	0.1
Clear CO_2 (0-30 [km]) sulfuric acid cloud	4.5	0.0	0.001	0.1

Table 3.6: Optical properties for Venus's aerosol and gas particles as a function of altitude at 630 [nm] wavelength range [39]

particle size spectrometer and the major composition in all modes is taken to be (75%) as H_2SO_4.

where a_{aer} is the albedo of the particles in the layer and is defined as the ratio of back scattered flux to the total incident solar flux of that layer according to Equation (3.18)

$$a_{aer} = \frac{F_u}{F_s} \tag{3.18}$$

F_u is the back scattered flux and F_s is the incident solar flux

gases	**Carbon dioxide** (CO_2)								**Nitrogen** (N_2)							**Sulfur dioxide** (SO_2)						
Re(m)	1.0004462 - 1.000435								1.0002970 - 1.00029							1.3396						
r_{eff} (in μm)	0.005–0.01 [μm]								0.005–0.01 [μm]							0.005–0.01 [μm]						
v_{eff}	0.001								0.001							0.001						
Haze, cloud and aerosol particles [40]																						
Wavelength *(μm)*	***0.1***	***0.2***	***0.3***	***0.4***	***0.5***	***0.6***	***0.7***	***0.8***	***0.9***	***1.0***	***1.5***	***2.0***	***2.5***	***3.0***	***3.5***	***4.0***	***4.5***	***5.0***	***5.5***	***6.0***	***6.5***	***7.0***
H_2SO_4 **complex refractive index (mode 1 , mode 2 cloud droplets)**																						
Re(m)[49] [53]	1.48	1.467	1.459	1.443	1.434	1.433	1.432	1.430	1.428	1.427	1.412	1.396	1.368	1.264	1.436	1.4464	1.4458	1.42	1.403	1.39	1.36	1.336
abs(Im(m))($\times 10^{-5}$)[49] [53]	0.0	0.0	0.0	0.0	0.0	0.0	0.0	0.00587	0.0197	0.0867	7.85	83.7	211.0	10000	20000	12000	9500	6000	5600	5800	7000	6500
Crystals (water ice, chlorine*) [72] **1.2 - 2.0 (based on different crystalline forms) * (*= in this research water ice crystals are used)**																						
Re(m)	1.4032	1.3938	1.3339	1.3194	1.3130	1.3094	1.3069	1.3049	1.3032	1.3015	1.2916	1.2740	1.2258	1.0392	1.4549	1.3620	1.3403	1.3290	1.3004	1.2970	1.3202	1.3194
abs(Im(m))($\times 10^{-3}$)	312.73	0.0	0.0	0.0	0.0	0.0	0.0	0.0	0.0	0.0	0.0006	0.0016	0.00093	0.4296	0.0164	0.0096	0.0287	0.012	0.0216	0.0649	0.05593	0.05558
Upper haze (H_2SO_4)																						
r_{eff} (in μm)	0.2 [μm] (particle distribution 0.1-0.4[μm])																					
v_{eff}	0.1																					
Upper clouds ($H_2SO_4 + contamination$) **(bimodal)**																						
r_{eff} (in μm)	0.175 [μm] (particle distribution 0.4-2[μm])																					
v_{eff}	0.1																					
Middle cloud ($H_2SO_4 + contamination + crystals$) **(trimodal)**																						
r_{eff} (in μm)	0.15 [μm], 1.25 [μm] (contamination), 3.5 [μm] (crystals)																					
v_{eff}	0.1																					
Lower cloud ($H_2SO_4 + crystal$) **(trimodal)**																						
r_{eff} (in μm)	0.1 [μm], 1.0 [μm] (contamination), 4.0 [μm] (crystals)																					
v_{eff}	0.1																					
Lower haze (H_2SO_4)																						
r_{eff} (in μm)	0.1 [μm]																					
v_{eff}	0.1																					
pre-cloud layers (H_2SO_4) **(bimodal)**																						
r_{eff} (in μm)	0.15 [μm], 0.4 [μm] (contamination)																					
v_{eff}	0.1																					

Table 3.7: Mie scattering matrix input variables for Venus's atmosphere, where Re(m) and Im(m) are real and imaginary parts of refractive index, r_{eff} (in μm) is the effective particle radius, and v_{eff} is effective variance of the particle size distribution (dimensionless).

3.1.3. The internal field

Previously atmosphere properties are introduced, following which the optical thicknesses of the molecule and aerosol are derived. Further, in this section, a photon path is traced along the different layers of the atmosphere to understand and compute the internal field using the forward model. The photon path tracing algorithm flow-chart is presented in the Figure 3.19.

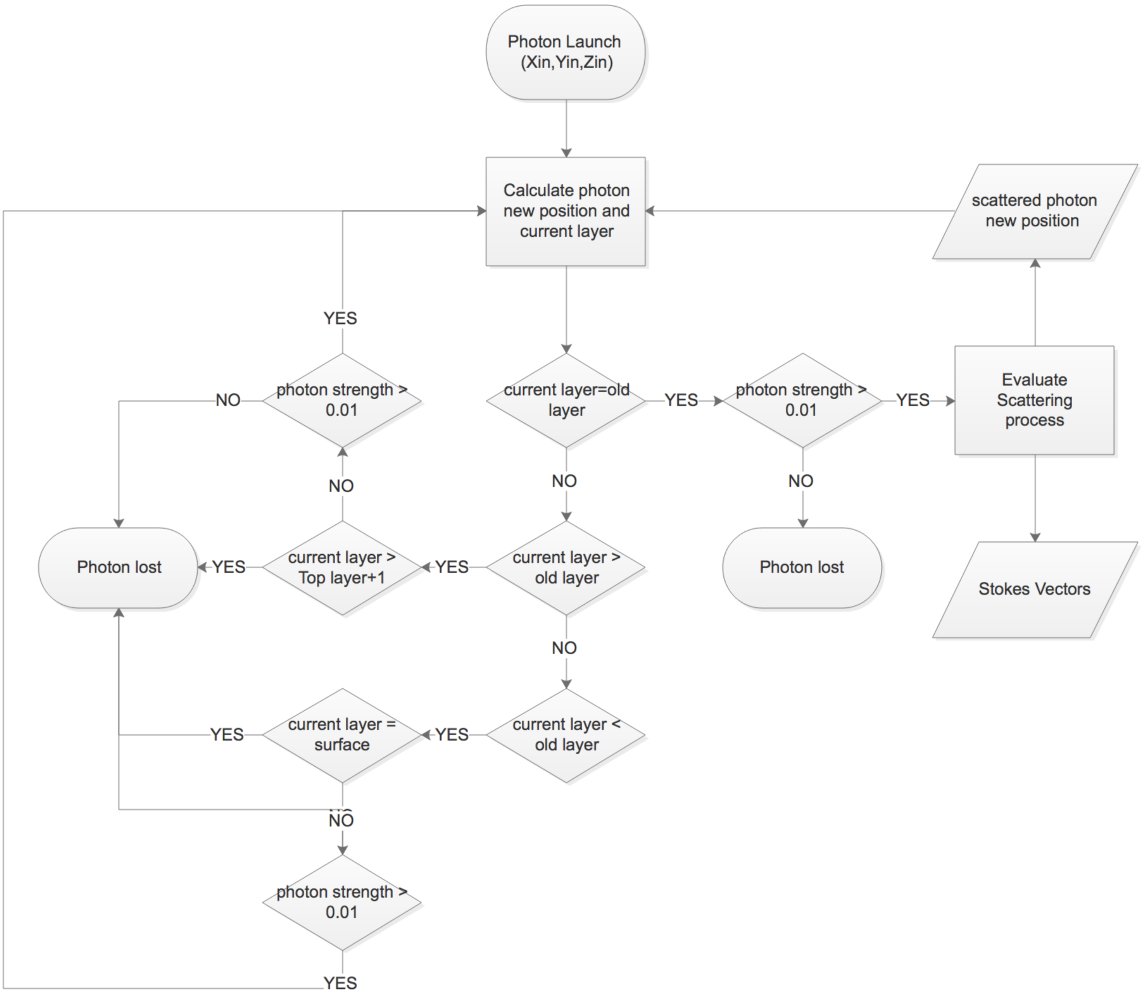

Figure 3.19: Photon path tracing algorithm flow chart

The photon is launched at the top of the atmosphere. The probability phase function and earlier defined atmosphere optical thicknesses makes the decision of what percentage of the incident photon is reflected, transmitted, scattered or absorbed. The new position of the photon is calculated, the photon is reflected if the photon new position is in the higher layers. The photon is transmitted if the photon new position is in the lower layers. The photon is scattered if the new position is in the same layer. The internal field or linear polarization information is measured during this photon transportation/scattering process.

The state of polarization of photon transported in the simulation has to be traced from the launch till the photon flux decreases to zero. The state of polarization is represented with respect to the scattering plane. This demands a reference system to track the changes in polarization state along the scattering process. The state of polarization as the light is scattered through a scattering media can be tracked using different techniques, *meridian plane MC*, algorithm defined by Chandrasekhar and Kattawar [20]. Chandrasekhar had envisioned such a reference system for Rayleigh scattering, tracking the photon polarization state along the scattering event in terms of the scattering plane and the meridian plane. In the current research, this technique is implemented, where the state of polarization is always represented in terms of the meridian plane.

The other two methods are *Euler MC* described by Bartel *et al.* [12], which uses the Euler angles, and the third method is *quaternion MC* [58], uses quaternion rotation coordinate system.

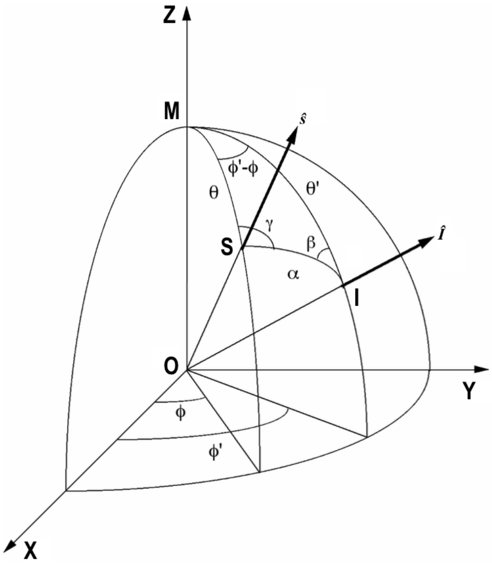

Figure 3.20: Meridian plane. the photon incident direction $\hat{I}$ and scattered direction $\hat{S}$

The geometry for *meridian plane MC* technique is according to Figure 3.20. The geometry is a unit sphere with the direction of the photon before and after the scattering event represented as I (incident) and S (scattered). The direction of the photon can be defined by two angles in the meridian plane, first is the elevation angle (θ), gives the angle between incident photon and Z-direction [(θ') angle between the scattered photon and Z-direction]. The second angle is ϕ, an angle between the meridian plane that contains the incident photon and X-Z plane [ϕ' angle between the meridian plane that contains the scattered photon and X-Z plane]. The photon directions is tracked by defining the unit vectors $\hat{I}$ (incident) and $\hat{S}$ (scattered), elements of the unit vectors are represented using the direction cosines $[u_x,u_y,u_z]$. The meridian plane is determined using the direction cosines and the Z-axis. From the unit sphere, MOI represents the incident meridian plane and MOS represents the scattered meridian plane. After the scattering, the new direction cosines are determined using the unit direction $\hat{S}$ and the Z-plane. The Stoke's vector is tracked using the transformation matrices and is represented with respect to the scattered meridian plane.

STEP 1: Photon Launch

In our Monte Carlo simulation, every iteration is to track a single photon through multiple scattering till it diminishes. The state of polarization at end of each scattering process is represented relative to the meridian plane,

- *STEP 1a:* The photon is launched at (0,0,Z), and the initial meridian plane is defined as ($\phi = 0$), that is X-Z reference plane according to Figure 3.21. The direction cosines for this launch co-ordinate becomes $[u_x,u_y,u_z]$=[0,0,1]

- *STEP 1b:* The Stoke's parameters during the launch specified with respect to the meridian reference plane is S = $[I\ Q\ U\ V]'$. In our research the incident light is assumed to be the sun light, since sun light is unpolarized the Stoke's parameters can be defined as S = [1 0 0 0]' with respect to the X-Z plane

STEP 2: Photon transported

The scattering event usually changes the photon traveling direction. In this research, Monte Carlo technique is used for the initial photon travel direction. The photon propagates a distance ΔS using a pseudo-random number (R) generated in the interval (0,1)

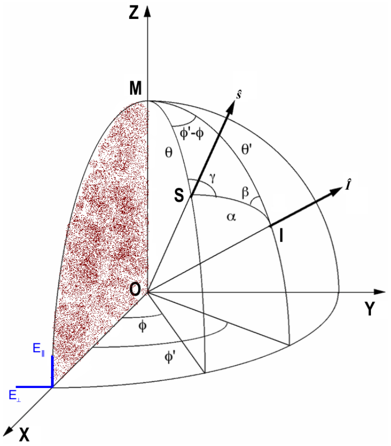

Figure 3.21: At photon launch the polarization state is represented with respect to the X-Z meridian plane

$$\begin{aligned} \Delta s &= \frac{ln(R)}{e(nlay)} \\ e(nlay) &= \frac{b(nlay)}{z(nlay+1) - z(nlay)} \end{aligned} \tag{3.19}$$

where e(nlay) is the effective extinction depth as a function of altitude for the current layer the photon is present, (z(nlay+1)-z(nlay)) is the layer thickness. The direction cosines along with the propagation distance computed above give the new photon position according to:

$$\begin{aligned} x' &= x + u_x \Delta s \\ y' &= y + u_y \Delta s \\ z' &= z + u_z \Delta s \end{aligned} \tag{3.20}$$

The ΔS evaluated so gives the photons new position, and says if the photon is reflected, transmitted (leaves the layer) or scattered (stays in the same layer)

STEP 3: Photon absorption

After each scattering, the photon intensity reduces as a function of the optical thicknesses of the media (absorption). This is tracked in the multiple scattering processes using a weighted factor (W) defined as the factor of absorption from single scattering albedo (a) of the current layer the photon is traveling in. This is similar to evaluating the diffuse flux in the layer. The single scattering albedo of the layer decides the photon extinction percentage after each scattering.

$$\begin{gathered} W_{new} = W_{old} \cdot a(nlay) \\ \begin{bmatrix} I_{new} \\ Q_{new} \\ U_{new} \\ V_{new} \end{bmatrix} = \begin{bmatrix} I_{old} \cdot W_{new} \\ Q_{old} \cdot W_{new} \\ U_{old} \cdot W_{new} \\ V_{old} \cdot W_{new} \end{bmatrix} \end{gathered} \tag{3.21}$$

Diffuse radiation (W_{new}) is the radiation that undergoes single or multiple scattering by the atmospheric composition and later reaches the bottom layer. According to Valko (1966), the diffuse radiation intensity depends on several factors, such as sun's position, scattering due to gas molecules and aerosols, vapor particles, extinction coefficient, the albedo of the surface (if present), as well as clouds extinction coefficient. The diffuse flux that is due to clouds and/or hazes is shown in the fig. 3.22, when the light reaches a certain point in the cloud it is scattered, absorbed or reflected, if it is scattered only once before reaching the viewpoint it is called single scattering, usually, the light is scattered multiple times before reaching the viewpoint as shown in Figure 3.22 for the multiple scatter case.

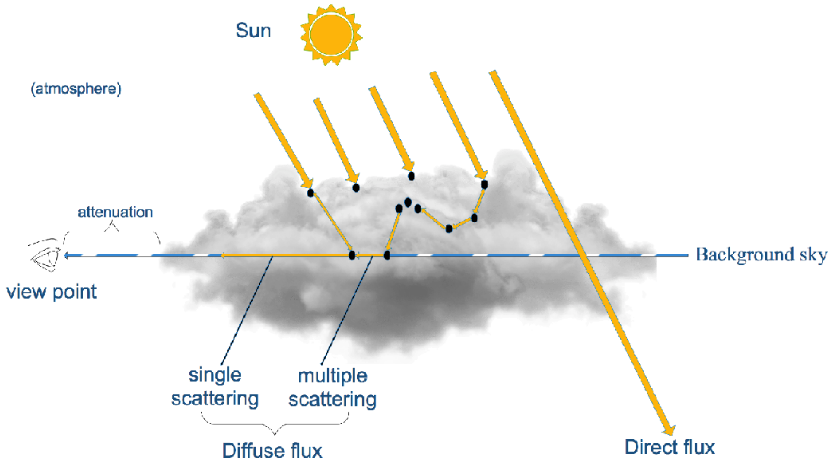

Figure 3.22: Internal field from the diffuse flux in the clouds

The radiation budget for each atmosphere layer developed earlier in Section 3.1.1 is evaluated and presented here. The budget represents the fraction of the total incident radiation that is either scattered, absorbed or reflected from each layer. The flux budget evaluation is governed by the solar zenith angle ($\mu = \cos\theta_0$ Figure 3.1b) and total optical thickness (τ Equation (3.16)) and the scattering phase function according to:

- The fraction of the solar beam transmitted through a layer of optical thickness τ:

$$F_{trans} = e^{-\frac{\tau}{\mu}} \tag{3.22}$$

- The fraction of the solar beam reflected back:

$$F_{refl} = (1 - e^{-\frac{\tau}{\mu}})a(\lambda)\beta(\lambda) \tag{3.23}$$

- The fraction of the solar beam absorbed within the layer:

$$F_{abs} = (1 - e^{-\frac{\tau}{\mu}})(1 - a(\lambda)) \tag{3.24}$$

- The fraction of the solar beam scattered in the layer:

$$F_{sca} = (1 - e^{-\frac{\tau}{\mu}})a(\lambda)(1 - \beta(\lambda)) \tag{3.25}$$

- The total fraction of the solar beam transmitted downward the layer:

$$F_{down} = e^{-\frac{\tau}{\mu}} + (1 - e^{-\frac{\tau}{\mu}})a(\lambda)(1 - \beta(\lambda)) \tag{3.26}$$

$\beta(\lambda)$ is the upscatter fraction [74][26], the fraction of the inbound radiance that is backscattered to the upper hemisphere. This factor can be evaluated using the angular distribution of the phase function over the scattering angle according to Equation (3.27).

$$\beta(\lambda) = \frac{\int_{\pi}^{2\pi} F(\Theta) sin\Theta d\Theta}{2\int_{0}^{\pi} F(\theta) sin\theta d\theta} \tag{3.27}$$

where $\Theta = \frac{\pi}{2} + \theta + \theta_z$ and θ_z is the solar zenith angle, and $F(\theta)$ is the total scattering phase function Equation (3.16). When the $\theta_z = 0$ the upscatter fraction corresponds to the simple backscatter ratio b according to:

$$b = \frac{\int_{\pi/2}^{\pi} F(\theta) sin\theta d\theta}{\int_0^{\pi} F(\theta) sin\theta d\theta} \tag{3.28}$$

The radiation budgets evaluated using earlier equations are schematically presented in Figure 3.23a, the total flux transmitted to the lower layers is the sum of downward scattered light and the directly transmitted light. The transmitted total flux for each layer from the current research is presented in Figure 3.23b. It is observed from the current research model that the total flux transmitted below the ammonia ice cloud layer is close to zero. The average diffuse flux is integrated along the horizontal view plane and represented as a function of the altitude. The results of the diffuse flux evaluation are discussed in section 4.1.

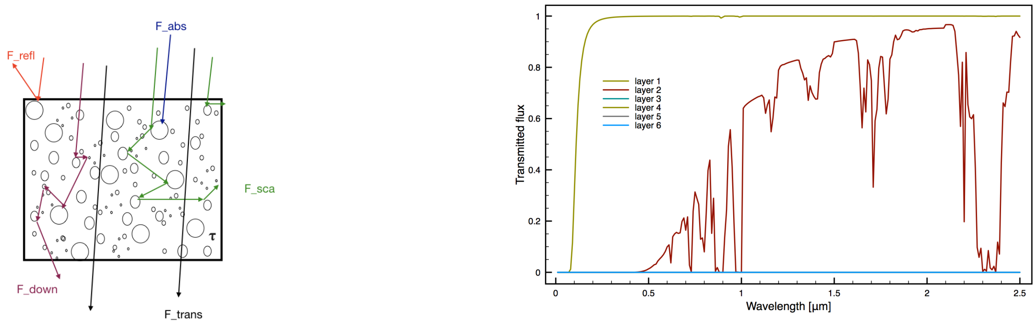

(a)

(b) The effective transmission including downward scattered flux when all the layers are stacked upon as discussed in the plane parallel model

Figure 3.23: (a) schematic presentation of various optical paths that occur within a layer, and (b) The effective downward transmission that included downward scattered flux and direct transmitted flux for each layer

STEP 4: Rejection Method

The rejection method is used to derive the scattering angle (Θ) and angle of rotation (Ψ) into the scattering plane, from the scattering probability function. The scattering phase function shall determine the state of polarization of the scattered photon.
In case of unpolarized incident light, the Stoke's parameter is defined by $[1,0,0,0]^T$, and the scattering probability phase function is then given by Equation (3.29)

$$P(\Theta) = F11(\Theta) I_0 \tag{3.29}$$

If the incident light is polarized (multiple scattering) the Stoke's parameter is defined as $[I_0, Q_0, U_0, 0]^T$, and the scattering probability phase function is defined by the Equation (3.30)

$$P(\Theta, \Psi) = F_{11}(\Theta) I_0 + F_{12}(\Theta)[Q_0 \cos(2\Psi) + U_0 \sin(2\Psi)] \tag{3.30}$$

where F_{11} and F_{12} are the elements from the scattering matrix. In the rejection method, a pseudo-random number is generated for each of the angles Θ_R in the interval (0,π), Ψ_R in the interval (0,2π) and a random number for phase function P_R is generated between (0,1). The criteria to accept these random values generated is P(Θ_R,Ψ_R) ≤ P_R, if the criteria are true, then the Θ_R and Ψ_R are accepted as a solution, otherwise, the process is repeated until this condition is met. When the incident photon is unpolarized, the phase function reduces to P(Θ) = $F_{11} I_0$, and the probability phase function is similar to the case of single scattering.

From the accepted values of Θ_R and Ψ_R, the state of polarization is evaluated using the total phase matrix (F_CEquation (3.16)) and the incident photon polarization state as described in Section 3.1.3

STEP 5: Scattering and Rotation Matrices

The Scattering matrices give a multi-angle multi-spectral relation of all states of polarization before and after a scattering event in the scattering plane. Scattering plane is defined as the plane that contains the incident photon and the scattered photon according to Figure 3.24. In this step to evaluate the Stoke's parameters in the scattering plane, a rotation is performed from meridian plane to the scattering plane, then Stoke's parameter is evaluated using the scattering matrices, and as a final step, a rotation is performed back to the meridian plane from the scattering plane.

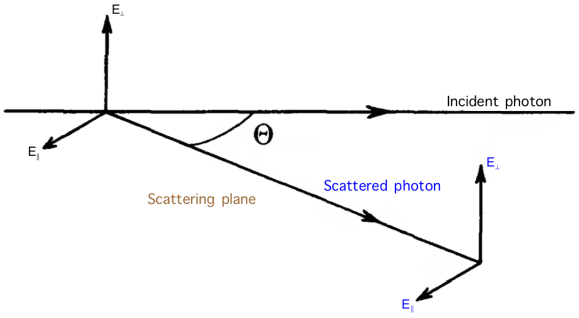

Figure 3.24: Scattering plane, and field components are represented with respect to the scattering plane as either ∥ or ⊥ to the scattering plane.

- *Rotation of the meridian reference frame onto the scattering plane:*
  The Stoke's vector of the incident photon is initially represented in the incident photon plane according to Figure 3.25a. To rotate the incident photon Stoke's vector to the scattering plane, the vector is rotated counterclockwise by an angle Ψ, the rotation matrix $R(\Psi)$ is defined according to

$$R(\Psi) = \begin{bmatrix} 1 & 0 & 0 & 0 \\ 0 & \cos(2\Psi) & \sin(2\Psi) & 0 \\ 0 & -\sin(2\Psi) & \cos(2\Psi) & 0 \\ 0 & 0 & 0 & 1 \end{bmatrix} \tag{3.31}$$

  This brings the Stoke's vector from MOI (incident photon) plane to the MSI (scattering) plane

- *Scattering event at an angle:* Θ
  In the scattering plane, the scattering angle Θ is obtained from the rejection method Section 3.1.3 and the scattering matrix elements evaluated at this scattering angle are used to evaluate the new polarization orientation. The scattering matrix is multiplied by the previously rotated Stoke's vectors and the new Stoke's vector for the scattered photon is obtained in the scattering plane reference according to Figure 3.25b

$$M(\Theta) = \begin{bmatrix} F_{11}(\Theta) & F_{12}(\Theta) & 0 & 0 \\ F_{12}(\Theta) & F_{11}(\Theta) & 0 & 0 \\ 0 & 0 & F_{33}(\Theta) & F_{34}(\Theta) \\ 0 & 0 & -F_{34}(\Theta) & F_{33}(\Theta) \end{bmatrix} \tag{3.32}$$

  The scattering angle Θ and rotation angle Ψ, is used later to update the direction cosines for the scattered photon direction

- *Rotation from the scattered plane to the meridian reference plane:*
  The new evaluated Stoke's parameter for the scattered photon is represented according to Figure 3.25c. The Stoke's vector is rotated back to the meridian plane with a rotational angle (-γ). This rotation angle

is evaluated using the updated direction cosine for the photons new direction as defined by Equation (3.37) in Section 3.1.3. The rotation matrix $R(-\gamma)$ is according to:

$$R(-\gamma) = \begin{bmatrix} 1 & 0 & 0 & 0 \\ 0 & \cos(2\gamma) & -\sin(2\gamma) & 0 \\ 0 & \sin(2\gamma) & \cos(2\gamma) & 0 \\ 0 & 0 & 0 & 1 \end{bmatrix} \tag{3.33}$$

- The final Stoke's vector after the scattering event in the reference meridian plane is according to:

$$S_{scat} = R(-\gamma)\ M(\Theta)\ R(\Psi)\ S_{inc} \tag{3.34}$$

STEP 6: Update direction cosine and evaluate rotation angle γ

As a final step for the next photon scattering event (in multiple scattering) the direction of the scattered photon is updated. The trajectory is updated for the photon along the next scattering direction. The new direction cosines are represented as $\mathbf{\hat{u}}$. This is evaluated using the scattering angle Θ and the rotation angle Ψ, and the current direction cosines are represented as $[u_x, u_y, u_z]$, this gives the new direction cosines according to

In case the value of the direction cosine element along z-direction $|u_z| \approx 1$:

$$\begin{aligned} \mathbf{\hat{u}}_x &= \sin\Theta\cos\Psi \\ \mathbf{\hat{u}}_y &= \sin\Theta\sin2\Psi \\ \mathbf{\hat{u}}_z &= \cos\Theta\frac{u_z}{|u_z|} \end{aligned} \tag{3.35}$$

In all other cases of u_z:

$$\begin{aligned} \mathbf{\hat{u}}_x &= \frac{1}{\sqrt{1-u_z^2}}\sin(\Theta)\left[u_x u_y\cos(\Psi) - u_y\sin(\Psi)\right] + u_x\cos(\Theta) \\ \mathbf{\hat{u}}_y &= \frac{1}{\sqrt{1-u_z^2}}\sin(\Theta)\,[u_x u_z\cos(\Psi) - u_x\sin(\Psi)] + u_y\cos(\Theta) \\ \mathbf{\hat{u}}_z &= \sqrt{1-u_z^2}\ \sin(\Theta)\cos(\Psi)\left[u_y u_z\cos(\Psi) - u_x\sin(\Psi)\right] + u_z\cos(\Theta) \end{aligned} \tag{3.36}$$

The rotation angle γ is used to obtain the Stoke's vector in the meridian reference plane from the scattering plane for the new scattered position. The angle γ is evaluated according to Equation (3.37) provided by Hovenier [36]:

$$\cos\gamma = \frac{-u_z + u_z\cos\Theta}{\pm\sqrt{\left(1-\cos^2\Theta\right)\left(1-u_z^2\right)}} \tag{3.37}$$

STEP 7: Photon Life

The above steps are repeated until one of the boundary conditions are reached. The photon is traced along its multiple scattering events until the photon flux decreases, where the extinction is checked as a weighted factor given by the absorption coefficients as evaluated in Section 3.1.3. The other boundary case is if the scattered photon new location is outside the defined top or bottom layers that is Z>Z_{top} [km] or Z=0 [km]. In either case, there is no photon left and the last known Stoke's vector is rotated one final time onto the plane that contains the detector. The detector frame rotation is defined by the angle (φ) and the rotation matrix $R(\varphi)$. The final Stoke's parameters as seen by the detector is given by S_D. These give the internal field with respect to the detector plane.

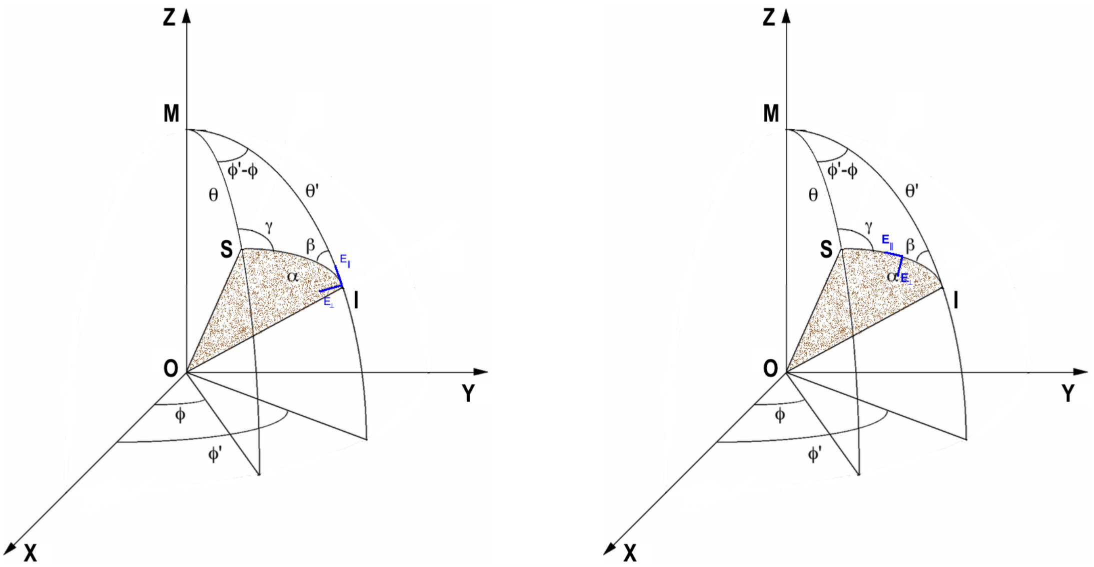

(a) S_{inc} (b) $S' = R(\Psi)\ S_{inc}$

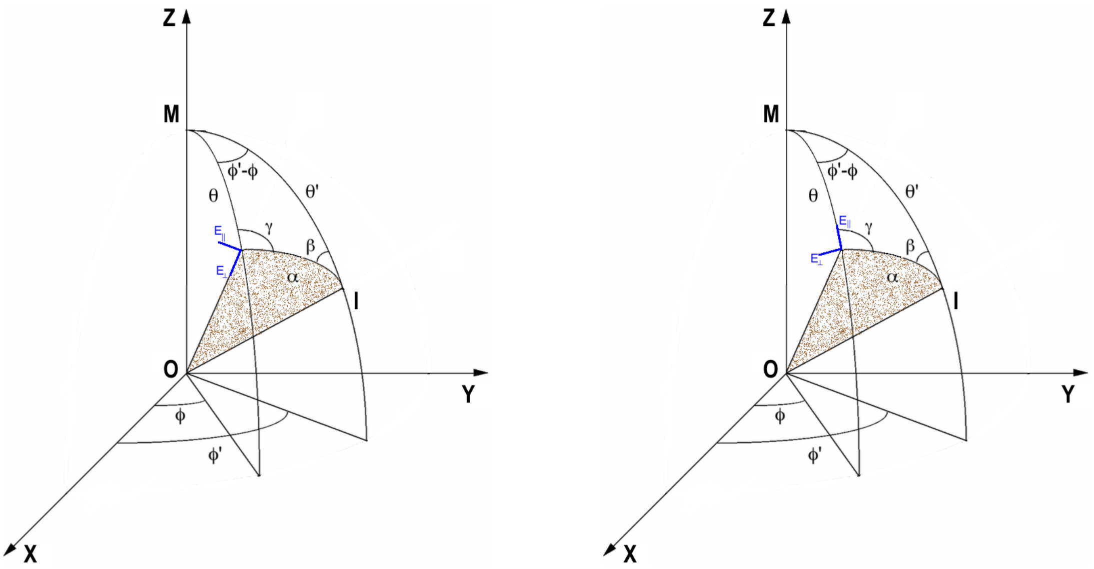

(c) $S" = M(\Theta)\ R(\Psi)\ S_{inc}$ (d) $S_{scat} = R(-\gamma)\ M(\Theta)\ R(\Psi)\ S_{inc}$

Figure 3.25: Scattering and Rotation matrices to evaluate the Stoke's vector in new scattered photon direction

$$\begin{aligned} \varphi &= -\tan^{-1}\left(\frac{u_y}{u_x}\right) \\ S_D &= R(\varphi)\ S_{scat} \end{aligned} \tag{3.38}$$

The degree and angle of linear polarization are evaluated using this method, and the results from the forward model are discussed in Chapter 4.

4

Forward Model Results

> A day on Saturn lasts 10 hours,
> Just like Saturday and Sunday on Earth.
>
> ***:)***

Introduction

For the forward model described in Chapter 3 the results are obtained for the internal field and polarization information retrieval, and these results are discussed for Saturn's and Venus's atmosphere models in this chapter. The results for diffuse flux in general (otherwise specified) are plotted as a function of the altitude and the solar zenith angle. For this, the detector is assumed to be descending along the zenith axis of the meridian reference frame, with the viewing direction (integrated over 0 to π) along the horizontal plane of the descent profile. All notations start with the initial meridian reference plane as X-Z plane. For evaluating the degree and angle of linear polarization, the Stokes formalism is used. This is done as a function of the view angle 0 to π and as the detector is moved along the zenith axis towards the bottom in the meridian reference frame.

4.1. Diffuse flux evaluation

The solar radiance F_p available at the planet can be evaluated according to Equation (4.3). The solar luminosity is evaluated assuming a black-body radiation. For this, black-body radiation with unit area and a temperature of 5800[K] is assumed, and using the Stefan-Boltzmann equation the radiation luminosity is evaluated according to Equation (4.1).

$$\begin{aligned} S_S &= \sigma T_{sun}^4 \\ S_S &= (5.67 \times 10^{-8}\ Wm^{-2}K^{-4})(5800K)^4 \\ S_S &= 63 \times 10^6 [Wm^{-2}] \end{aligned} \tag{4.1}$$

This black-body radiation luminosity is then extended to the Sun's radiation area according to Equation (4.2)

$$\begin{aligned} L_S &= S_S 4\pi r_s^2 \\ L_S &= 63 \times 10^6 \cdot 4\pi \cdot (695.7 \cdot 10^6)^2 \\ L_S &= 3.832 \times 10^{26}\ W \end{aligned} \tag{4.2}$$

where, L_S is the solar luminosity emitted by the Sun, r_s[m] is the mean radius of the Sun

$$F_p = \frac{L_S}{4\pi d_p^2}\ [W/m^2] \tag{4.3}$$

where, F_p $[W/m^2]$ is the solar radiance at a heliocentric distance d_p [m] from the Sun.

The solar radiance available at the planet's, considering the mean distances from the Sun gives a total flux for Venus's as 2614.37 $[W/m^2]$ (@ $d_p = 108 \times 10^6 [km]$) and at Saturn the total flux is 14.91 $[W/m^2]$ (@ $d_p = 1.43 \times 10^9 [km]$). The total flux is converted to the number of photons that illuminate a unit area per second. This conversion is also necessary as the photon density is required to evaluate the number of electrons generated at the detector and the signal to noise ratio budget. Each photon at a specific wavelength has a distinct quantum or energy according to Equation (4.4).

$$\begin{aligned} E_p &= \frac{hc}{\lambda} \\ N_p &= \frac{F_p}{E_p} \end{aligned} \tag{4.4}$$

$$N_p = F_p \cdot \lambda \cdot 5.03 \times 10^{15} [1/(m^2 \cdot s)]$$

where λ [nm] is the wavelength of interest. From this the total number of photons considering a wavelength of $0.7[\mu m]$ (in the visible wavelength region, the region of interest (0.4 to $1.0[\mu m]$) for studying the

	Saturn	Venus's
Mean distance from Sun (d_p)	$1.43 \cdot 10^{12}$[m]	$108 \cdot 10^{9}$[m]
Mean Solar radiance(F_p)	14.91 [W/m^2]	2614.37 [W/m^2]
Avg. number of Photons	$5.25 \cdot 10^{19}$ [$m^{-2}s^{-1}$] $1-8 \cdot 10^{19}$ [$m^{-2}s^{-1}$] ($@\lambda = 0.1-1.0\mu m$)	$9.2 \cdot 10^{21}$ [$m^{-2}s^{-1}$] $1-14 \cdot 10^{21}$ [$m^{-2}s^{-1}$] ($@\lambda = 0.1-1.0\mu m$)

Table 4.1: Solar radiance at the planet's with mean orbital distances

aerosols for Saturn's atmosphere). The number of photons per unit area per second for Saturn is obtained as $N_{S_p} = 5.25 \times 10^{19}$ photons, and for Venus's $N_{V_p} = 9.2 \times 10^{21}$ photons. The different parameters for each of the atmospheres, Saturn and Venus's are summarized in Table 4.1

4.1.1. Diffuse Flux at Saturn's atmosphere

The diffuse flux is evaluated as described earlier in Chapter 3. The results are tabulated for different Solar zenith angles at a step value of 10°. The diffuse fluxes are evaluated at different wavelengths. The following observations can be inferred about the diffuse flux plot obtained from the forward model.

Figure 4.1 and Figure 4.2 shows the percentage diffuse flux to the total incident solar flux at various zenith angles ($0° < \theta_z < 90°$) at increments of 10° as a function of the altitude. Most of the diffuse flux is from scattering in the cloud layers. The diffuse flux is dependent on the position of the detectors with respect to the Sun (solar zenith angle). The diffuse flux is higher in the lower layers when the sun is at the highest in the sky (solar zenith $\theta_z = 0°$). At solar zenith angle $\theta_z = 0°$ the diffuse flux in the lower layers is maximum, in the order of 16% at $\lambda = 0.6\mu m$ and 10^{-4}% at $\lambda = 1.0\mu m$ as seen in Figure 4.1. Whereas, the diffusion in the upper layers at this solar zenith angle ($\theta_z = 0°$) is 0.13% at $\lambda = 0.6\mu m$ and $4 \cdot 10^{-4}$% at $\lambda = 1.0\mu m$ as seen in Figure 4.2.

The penetration of the solar radiance decreases as the Sun reaches the horizon, decreasing the number of photons available at the lower layers, and increasing the photons available in the upper layer that is scattered as seen in Figure 4.2. When the Sun is at the horizon (taking $\theta_z = 80°$) the diffusion in the lower layers is 2% at $\lambda = 0.6\mu m$ and 0 at $\lambda = 1.0\mu m$ as seen in Figure 4.1. Whereas, the diffusion in the upper layers at this solar zenith angle ($\theta_z = 80°$) is 0.27% at $\lambda = 0.6\mu m$ and 0.002% at $\lambda = 1.0\mu m$ as seen in Figure 4.2.

As the Sun reaches the horizon from the highest point in the sky (θ_z changes from $0° \rightarrow 80°$), the diffuse flux increases in the upper layers from 0.13% → 0.27% $@\lambda = 0.6\mu m$ and from $4 \cdot 10^{-4}\% \rightarrow 0.002\%$ $@\lambda = 1.0\mu m$. At the same time the diffuse flux decreases in the lower layers from 16% → 2% $@\lambda = 0.6\mu m$ and from $10^{-4}\% \rightarrow$ 0 $@\lambda = 1.0\mu m$

Diffuse flux as a function of Wavelength at Saturn's atmosphere

The solar flux [W/m^2] reaching a planet's outer atmosphere varies as a function of wavelength. The photons that reach the atmosphere undergoes certain factor of absorption which varies as a function of wavelength and based on the composition of the atmosphere. On Earth, the solar flux at the top layer of the atmosphere and the direct flux density [W/m^2] at the sea level is shown in the Figure 4.3. The direct flux reaching the bottom depends on the wavelength and this is due to absorption and scattering or diffusion of flux in the atmosphere.

In the forward model developed for the current research, a methane absorption spectrum for each layer was evaluated as described in Section 3.1.1. The diffuse flux in these layers also governs the total radiation that shall reach the bottom of the atmosphere. The simulation results for the diffusion due to aerosol and

---

[1] Layer 1 = gas layer (178-550km)

[2] Layer 2 = ammonia haze layer (136-178km)

[3] Layer 3 = ammonia ice cloud layer (95-136km)

[4] Layer 4 = no aerosol, gas layer (71-95km)

[5] Layer 5 = ammonia hydrosulfide layer (30-71km)

[6] Layer 6 = water ice cloud layer (0-30km)

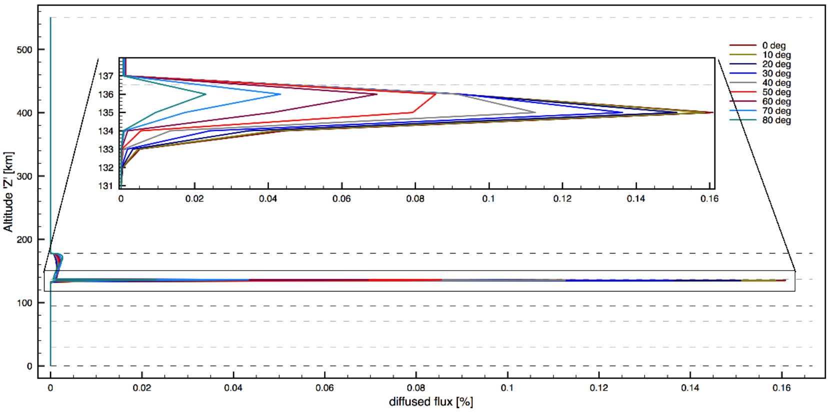

(a) @$\lambda = 0.6\mu m$

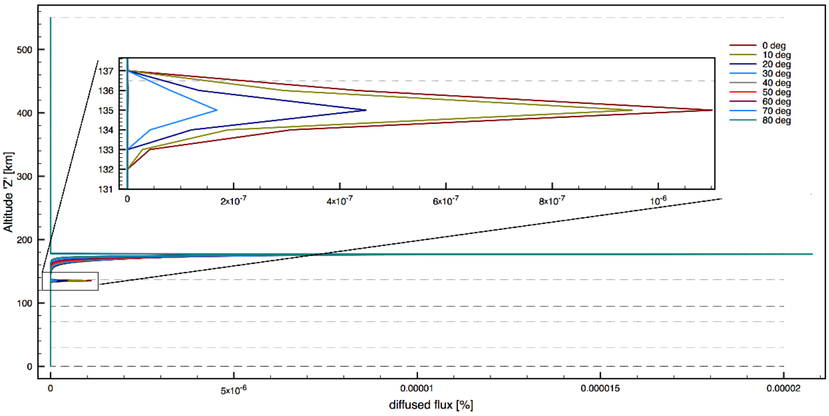

(b) @$\lambda = 1.0\mu m$

Figure 4.1: Diffuse flux as a function of solar zenith angle ($0^\circ < \theta_z < 90^\circ$) at increments of 10° in lower layers of Saturn @$\lambda = 0.6\mu m$ and @$\lambda = 1.0\mu m$. Higher diffuse flux in lower layer at $\theta_z = 0^\circ$

molecule scattering in each layer are shown in Figure 4.4. The average diffusion is 0.12% ($0 - 0.6\mu m$) in the ammonia haze layer (layer2 in the model) and 0.15% ($0.4 - 2.5\mu m$) in the ammonia ice clouds layer (layer3 in the model), in the lower layer (layer3-6) the diffusion is zero, as no photon or a very small number of photon reach these layers due to absorption, scattering and reflection in the upper layers.

It can be observed from the forward model that the diffuse flux is higher in the layers with haze or cloud particles and has less or no diffuse flux in the layers that contains only the gas molecules. The gas molecule scattering is high at small ($0.1 - 1.0\mu m$) wavelengths and the aerosol scattering present in the clouds and hazes is higher at higher wavelengths ($1.0 - 2.5\mu m$), which is evident from the scattering thickness evaluated in Chapter 3.

The polarization nephelometer instrument for Saturn aims to measure the aerosol microphysical properties in the visible wavelength region. From the diffuse flux plot Figure 4.4, it can be seen that the available diffuse flux density is less in the visible region, in case no source is carried on-board it shall be really optimistic to measure the aerosol properties for all the layers. However, measuring the ammonia haze and ammonia ice cloud properties from the natural diffuse flux might be possible as these layers display the highest diffusion at small wavelengths.

4.1.2. Diffuse Flux at Venus's atmosphere

The diffuse flux at Venus's is evaluated in a similar procedure to that of Saturn. The Venus's atmosphere receives Solar radiance (number of photons per [m^{-2}]) a factor of 10^6 higher than the Saturn's atmosphere. The diffuse flux is also higher indeed in Venus's atmosphere. The diffuse flux as a function of solar zenith angle at $\lambda = 0.7\mu m$ & $\lambda = 1.0\mu m$ is shown in Figure 4.5 and Figure 4.6. The diffusion flux is very high in the top cloud

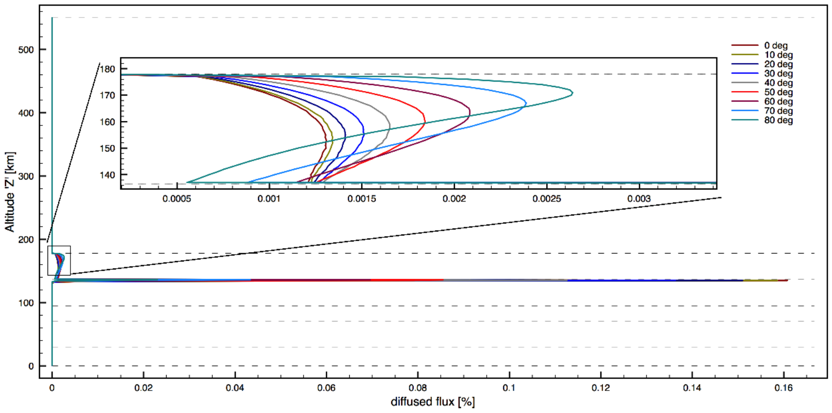

(a) @$\lambda = 0.6\mu m$

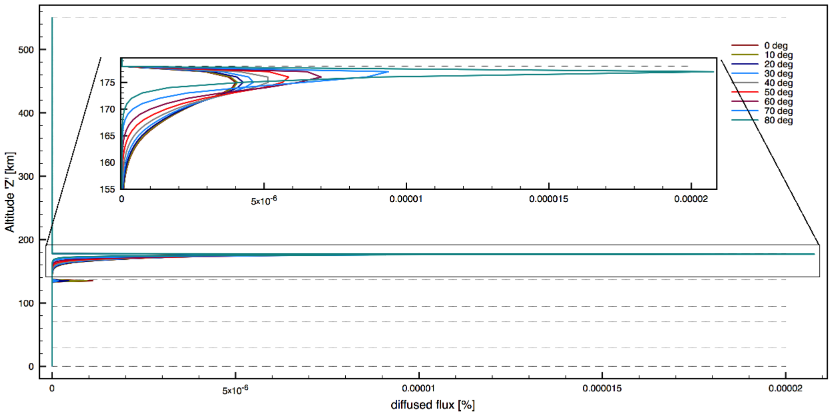

(b) @$\lambda = 1.0\mu m$

Figure 4.2: Diffuse flux as a function of solar zenith angle ($0^\circ < \theta_z < 90^\circ$) at increments of 10° upper layers of Saturn @$\lambda = 0.6\mu m$ and @$\lambda = 1.0\mu m$, Higher diffuse flux in upper layers as Sun reaches the horizon $\theta_z = 80^\circ$

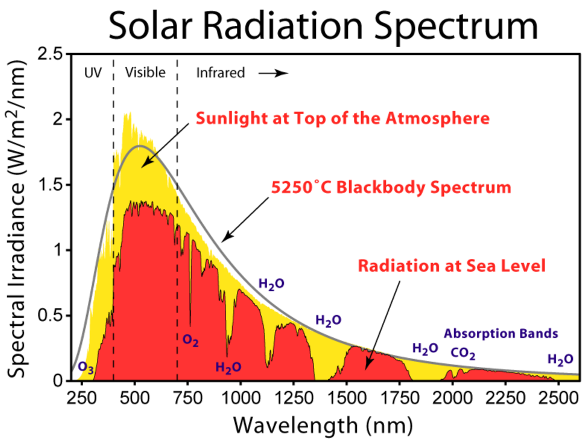

Figure 4.3: Absorption spectrum for Earth [image source:[7]]

regions (the upper layers).

Figure 4.5 and Figure 4.6 shows the percentage diffuse flux to the total incident solar flux at various zenith angles ($0^\circ < \theta_z < 90^\circ$) at increments of 10° as a function of the altitude. At solar zenith angle $\theta_z = 0^\circ$ the diffusion in the lower layers is maximum of 6.9% at $\lambda = 0.6\mu m$ and 6.6% at $\lambda = 1.0\mu m$ as seen in Figure 4.5. Whereas, the diffusion in the upper layers at this solar zenith angle ($\theta_z = 0^\circ$) is 4.2% at $\lambda = 0.6\mu m$ and 4.3% at $\lambda = 1.0\mu m$ as seen in Figure 4.6.

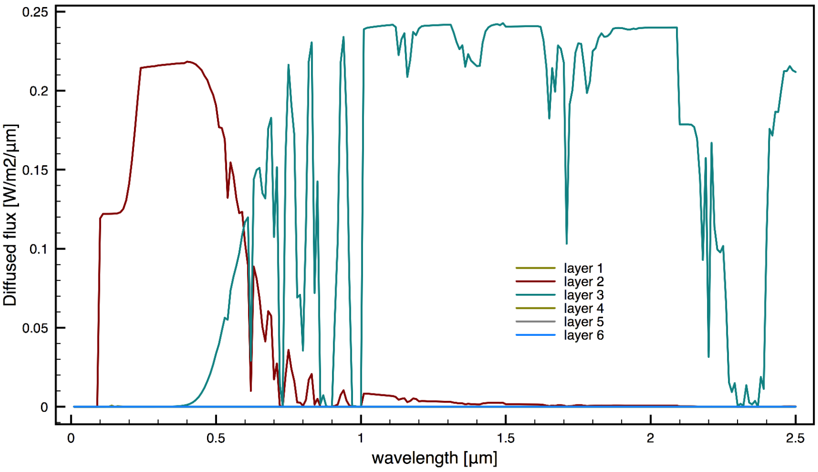

Figure 4.4: The average diffuse photon density flux $[W/m^2/\mu m]$ as a function of wavelength for each layer for Saturn.

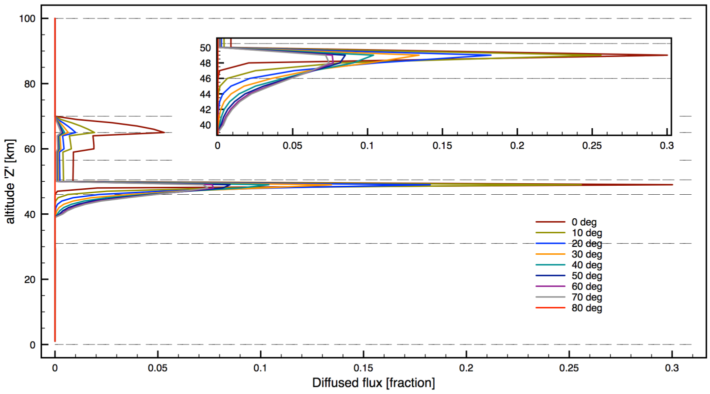

(a) @$\lambda = 0.6\mu m$

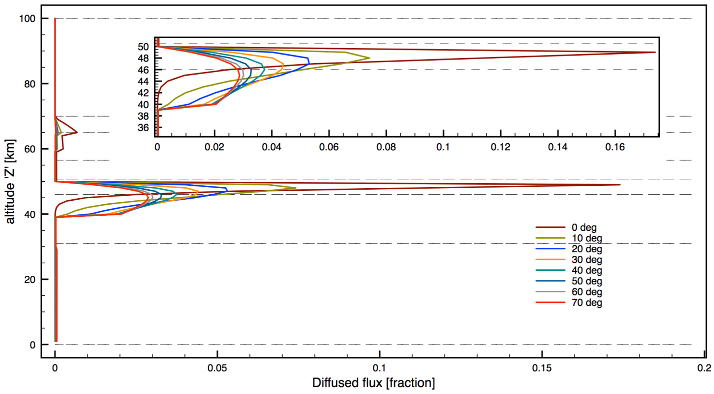

(b) @$\lambda = 1.0\mu m$

Figure 4.5: Diffuse flux as a function of solar zenith angle $(0° < \theta_z < 90°)$ at increments of 10° in lower layers of Venus @$\lambda = 0.6\mu m$ and @$\lambda = 1.0\mu m$. Higher diffuse flux in lower layer at $\theta_z = 0°$

As the Sun reaches the horizon the total diffuse flux in all the layers reduce, however, the lower layer see's a higher reduction in the diffuse flux than the upper layers. As seen from the Figure 4.5 and Figure 4.6. When the Sun reaches the horizon from the highest point in the sky (that is θ_z changes from $0° \rightarrow 80°$), the diffuse flux in the lower layer reduce from, from 30% → 7.0% @$\lambda = 0.6\mu m$ and from 17.4% → 2.87% @$\lambda = 1.0\mu m$. At the same time the diffuse flux in the upper layers changee from 5.3% → 0.29% @$\lambda = 0.6\mu m$ and from

0.6% → 0.02 @$\lambda = 1.0\mu m$.

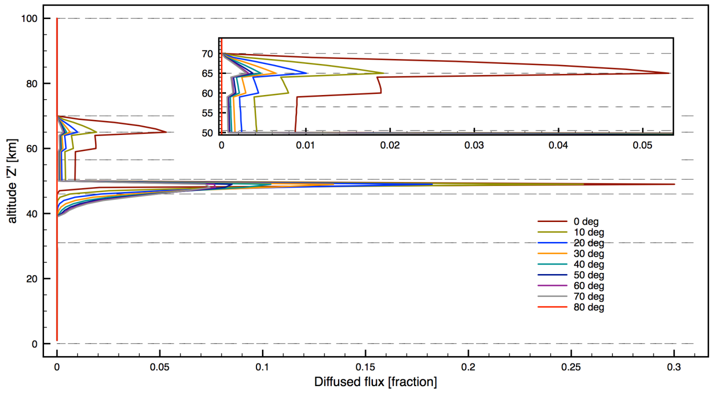

(a) @$\lambda = 0.6\mu m$

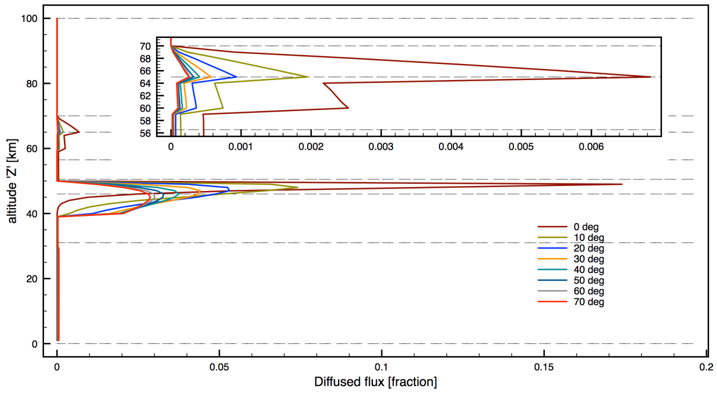

(b) @$\lambda = 1.0\mu m$

Figure 4.6: Diffuse flux as a function of solar zenith angle ($0^\circ < \theta_z < 90^\circ$) at increments of 10° upper layers of Venus @$\lambda = 0.6\mu m$ and @$\lambda = 1.0\mu m$, Higher diffuse flux in upper layers as Sun reaches the horizon $\theta_z = 80^\circ$

Diffuse flux as a function of Wavelength at Venus's atmosphere

For Venus's atmosphere the diffuse flux is sufficient enough and the direct measurement nephelometer concept presented in this research can profile the aerosol properties for all the layers of Venus using this natural sunlight. From the Figure 4.7 it is seen that the diffusion is of higher percentage in the middle cloud regions. The Venus synthesis report from [39] also speculated the same from the Pioneer Venus probe data.

4.2. Internal field evaluation

The state of polarization of the scattered light is required to determine the microphysical properties of the aerosol and haze particles. The nephelometer modulates the polarization information into a sinusoidal wave as discussed in Chapter 2. In the data retrieval during the post-processing, a demodulation technique is used to retrieve the polarization information. The forward model evaluates the polarization information in terms of Stokes vector. Following this, the Stokes vector is converted to the degree and angle of linear polarization as discussed in Chapter 2.

4.2.1. Saturn's polarization field

The forward model has been used to evaluate the attenuation in the degree of polarization for various scattering orders. This shall be used to estimate the possible scatter orders until which the degree of polarization can be easily discerned. The attenuation of the degree of polarization is traced for the ammonia ice cloud layer

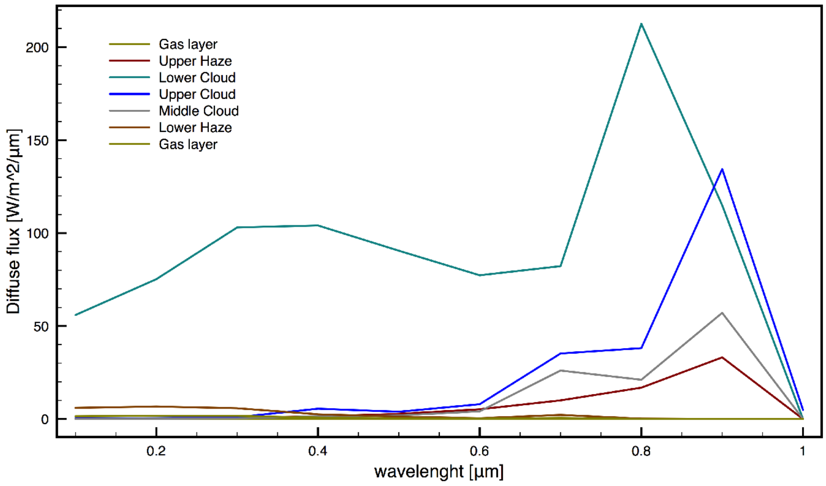

Figure 4.7: The average diffuse photon density flux $[W/m^2/\mu m]$ as a function of wavelength for each layer for Venus.

for several scatter orders by integrating the measurement over different solar zenith angles and is shown in fig. 4.8 for $\lambda = 1.1\mu m$. It can be observed from the forward model that the degree of polarization evaluated from diffuse flux follows the same trend or pattern over several scattering orders.

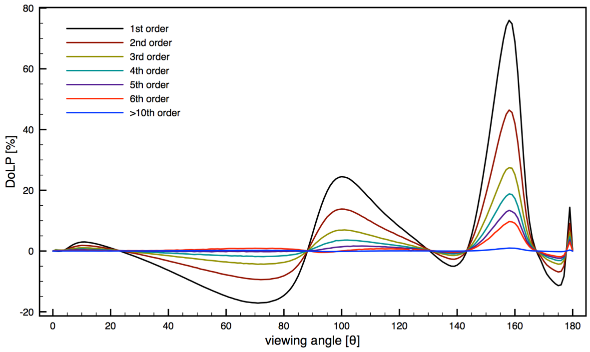

Figure 4.8: Degree of linear polarization as a function of viewing angle from the forward model integrated over different solar zenith angles for ammonia ice cloud layer (@$\lambda = 1.1\mu m$)

The polarization nephelometer can discern the particle microphysical properties if the degree of polarization retains its resolution as a function of viewing angle over multiple scatterings. This means that instrument must be able to learn and differentiate the peaks and zero-crossing of the degree of polarization, this also means that a lower signal to noise precision value is sufficient. The degree of polarization remains constant after a certain number of scatters or in another case the degree of polarization attenuates completely to zero over multiple scattering due to reducing flux density. The degree of polarization as a function of viewing angle is shown for different cloud layers at $\lambda = 1.0\mu m$ in Figure 4.17. It can be observed that the zero crossing points shall remain the same, but the degree of linear polarization P_l reduces over multiple scattering for specific particle composition and the wavelength at which it is measured. The zero-crossing of the degree of polarization P_l never change with respect to the view angle, If the direction of the reference axis is rotated by an angle Θ after scattering, the intensity I and the circular polarization Stoke's vector V are unchanged according to Equation (4.8). The values of Q and I are relatively changed, however the term $(Q^2 + U^2)$ remains unchanged and hence the degree of linear polarization P_l $(\sqrt{Q^2 + U^2}/I)$ also remains unchanged. The flattening in P_l with the increasing order is due to absorption leading to reduced photon flux after each scattering.

$$\begin{bmatrix} I' \\ Q' \\ U' \\ V' \end{bmatrix} = \begin{bmatrix} 1 & 0 & 0 & 0 \\ 0 & \cos(2\Theta) & \sin(2\Theta) & 0 \\ 0 & -\sin(2\Theta) & \cos(2\Theta) & 0 \\ 0 & 0 & 0 & 1 \end{bmatrix} \begin{bmatrix} I \\ Q \\ U \\ V \end{bmatrix} \tag{4.5}$$

$$Q' = Q\ \cos(2\Theta) + U\ \sin(2\Theta) \tag{4.6}$$

$$U' = -Q\ \sin(2\Theta) + U\ \cos(2\Theta) \tag{4.7}$$

$$Q'^2 + U'^2 = Q^2 + U^2 \tag{4.8}$$

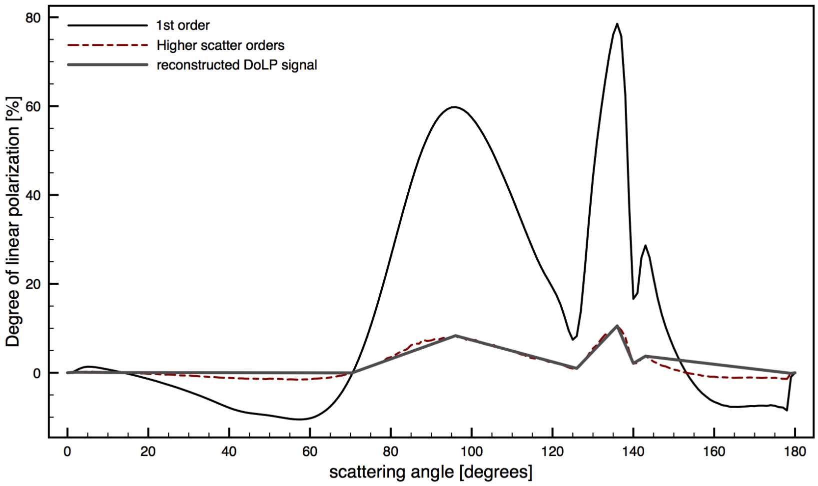

Figure 4.9: Degree of linear polarization reconstructed from the zero crossings and peak amplitudes by measuring at 9 scatter angles (2,13,70,96,126,136,140,143,180 [degrees]) for ammonia haze at $\lambda = 1\mu m$

By measuring these zero crossing, peaks and valley amplitudes it shall be possible to deduce the particle composition, even with the higher scatter orders, given that there is sufficient flux to measure in those layers. The degree of polarization (black line) shows the single scatter order reference, and the colored line shows the multiple scattering predictions from the forward model. The Figure 4.9 shows how a reconstruction could be possible by just measuring the zero crossings and the peak or valley amplitudes for higher orders that occur at specific scattering angles that are measured.

- NH3 Haze layer- This aerosol layer diffuse large percentage of the solar flux Figure 4.4, the degree of polarization can be easily distinguished for higher scattering orders using the forward model. In the model higher scatter orders are determined when the degree of linear polarization P_l is completely flattened. In the atmosphere the scattering includes all scatter orders, for this current model the degree of linear polarization per scatter orders is evaluated. At certain scatter order the photon flux reduces to zero or the state of P_l is fixed and this is termed as highest scatter order.

- NH3 Ice layer- The diffuse flux available is very low and particles have low single scattering albedo. The forward model evaluated that the prediction is possible for few scatter orders (<3) and attenuated to zero for higher orders

- In the lower layers, the diffuse flux is very low and averaging the results produced a huge noise in evaluating the degree of linear polarization for the single scatter case and attenuating to zero for all other scatter orders

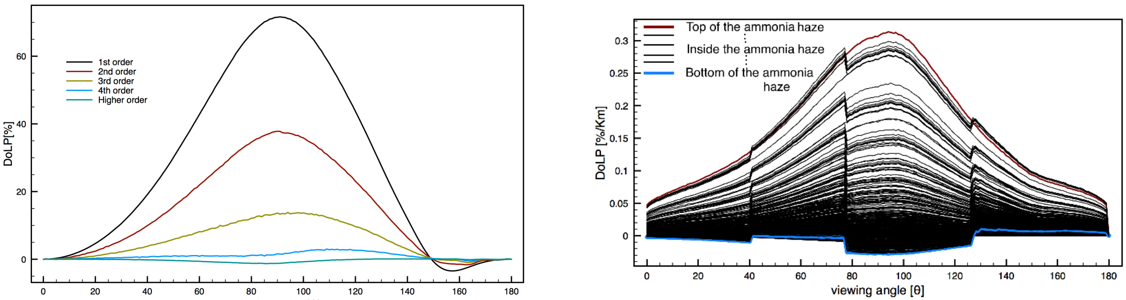

(a)

(b)

Figure 4.10: State of linear polarization for ammonia haze layer of Saturn's model atmosphere at $\lambda = 0.6\mu m$. (a) degree of linear polarization averaged per scatter order over the haze layer, (b) degree of linear polarization as measured from inside the ammonia haze layer for higher scatter orders

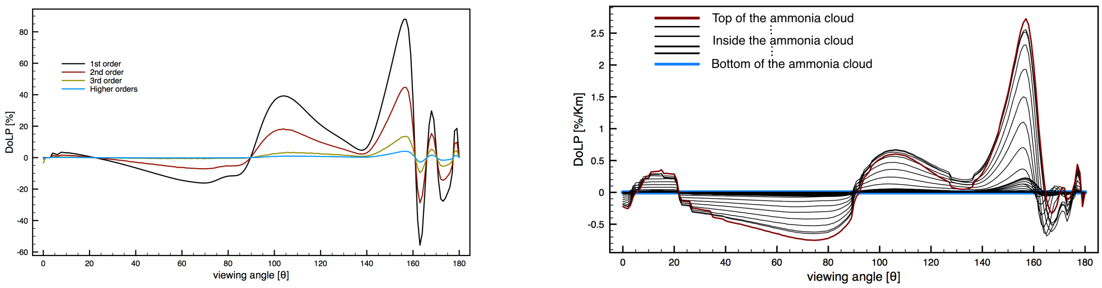

(a)

(b)

Figure 4.11: State of linear polarization for ammonia ice cloud layer of Saturn's model atmosphere at $\lambda = 0.6\mu m$. (a) degree of linear polarization averaged per scatter order over the ammonia cloud layer, (b) degree of linear polarization as measured from inside the ammonia ice cloud layer for higher scatter orders

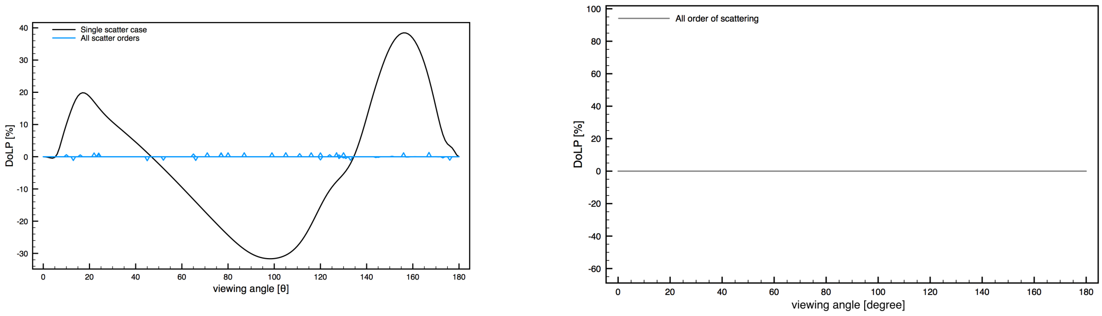

(a)

(b)

Figure 4.12: State of linear polarization for (a) ammonia hydrosulfide cloud layer and (b) other lower layer. of Saturn's model atmosphere at $\lambda = 0.6\mu m$.

From the forward model understanding, it can be deduced that with the lower precision of measurement the peaks can be easily distinguished alongside by measuring the zero crossing points, which stay constant over multiple scatter orders. This lower precision value can be used to obtain the integration time to have a good signal to noise ratio (say SNR=10). The relation between the precision for measuring the polarization information and number of photons required is given by the equation $e(Q/I) = e(U/I) = \sqrt{2/N}$. Hence for a precision of say 1% to measure the required polarization the number of photons required shall be 20000 photons per measurement and for a precision of say, 5% in DOLP the photons required is 800 per measurement, which is also the signal to noise ratio required for this precision. The attainable SNR and the integration times required are derived in Chapter 6.

The degree of polarization attenuation over multiple scattering for the ammonia ice cloud layers @$\lambda = 0.6$ and $1.6\mu m$. The degree of polarization evaluated from the forward model display signal noise @$\lambda = 0.6\mu m$ for higher orders, this is due to the lower diffuse flux available at this wavelength (see:Figure 4.4) in the ammonia ice cloud layer (layer 3 in the model), and the simulation falls short of the required samples to have a smooth signal.

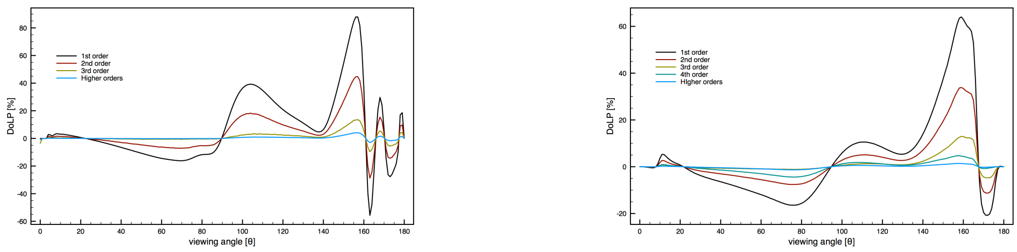

(a) @$\lambda = 0.6\mu m$

(b) @$\lambda = 1.6\mu m$

Figure 4.13: Degree of linear polarization for ammonia ice cloud layer of Saturn's model atmosphere @$\lambda = 0.6$ and $1.6\mu m$

The degree of polarization for ammonia ice cloud layer for a single scattered case for different wavelength is plotted in the Figure 4.14a. The DoLP signal constructed @$\lambda = 0.4\mu m$ is noisy given that the diffuse flux at this wavelength in the ammonia ice layer is very less $0.01[W/m^2/\mu m]$ (see Figure 4.4). The degree of linear polarization also changes as a function of wavelength for the same particle composition as shown in the case of multiple scattering as seen in Figure 4.14b, the diffuse flux is 0.1 $[W/m^2/\mu m]$ @ $\lambda = 0.6\mu m$, giving a noisy signal and $0.24[W/m^2/\mu m]$ @ $\lambda = 1.6\mu m$ giving a more smooth signal.

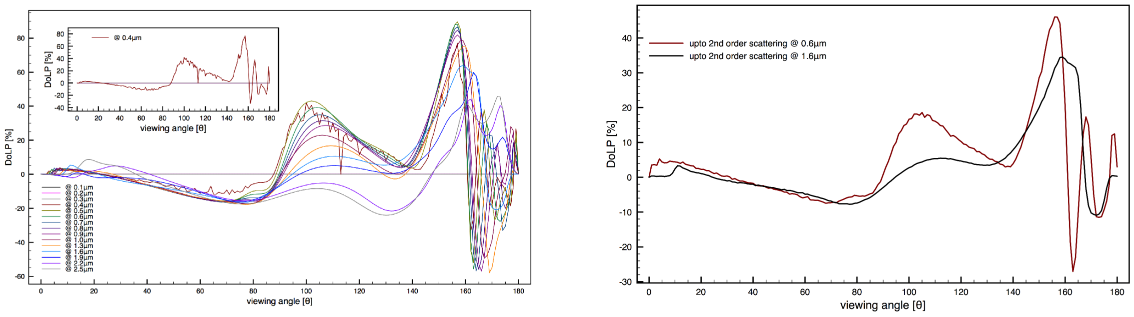

(a)

(b)

Figure 4.14: Degree of linear polarization for ammonia ice cloud layer single scattering order (a) Over all wavelengths $[0.1-2.5\mu m]$ and (b) multiple scatter displays noisy signal @$\lambda = 0.6\mu m$, that is due to the limited diffuse flux available @$\lambda = 0.6\mu m$ in comparison to the flux @$1.6\mu m$

It can be observed from the Figure 4.17 that the higher order scattering return to zero. The evaluation from the forward model returned that the scattered flux is attenuated highly within few scatter events, and the degree of polarization decreases to zero. However, form the model it is also derived that reconstruction from multiple scattering processes with zero-crossing reference points and measuring the peaks, it shall be possible to deduce the particle composition by correlating the measured data to the database generated at different scatter orders from the forward model.

The degree of linear polarization for the ammonia ice clouds is shown for certain viewing angles determined by the forward model for reconstruction of the signals as a function of wavelength in Figure 4.15 for single and multiple scattering. The percentage of polarization measured reduces with each scattering event.

The degree of linear polarization measured gives more information on the microphysical properties in comparison to just measuring the intensity profile as a function of viewing angle as shown from the forward model and is presented in Figure 4.16, the left side plots (a) represent the degree of polarization measured

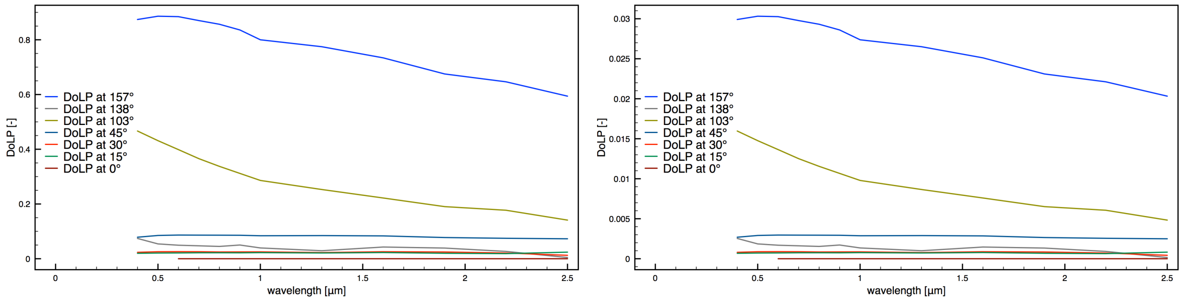

(a) Single scatter case

(b) Multiple scattered case

Figure 4.15: DoLP as a function of wavelength (a) Single scatter case and (b) multiple scattering order for the ammonia haze layer at viewing angles of 0°, 15°, 30° , 45° , 103°, 138°, 157°

inside a cloud or haze layer, and the right side plots (b) show the intensity profiles measured inside a cloud or haze layer.

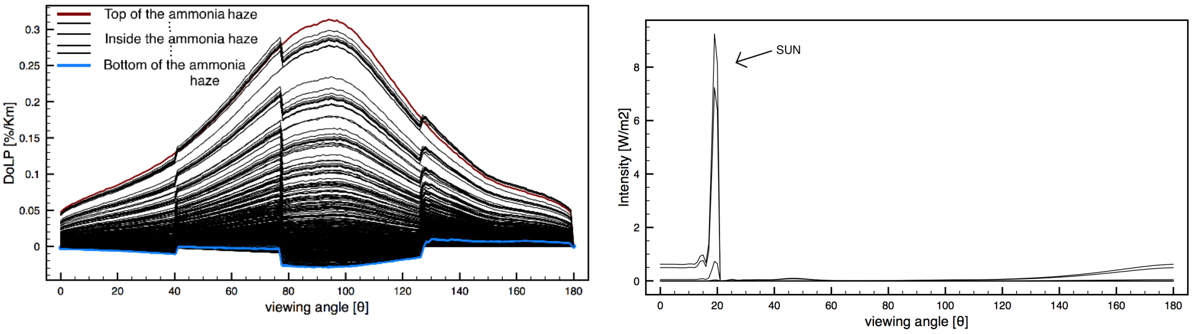

(a) Degree of linear polarization inside the ammonia haze layer

(b) Intensity profile inside the ammonia haze layer

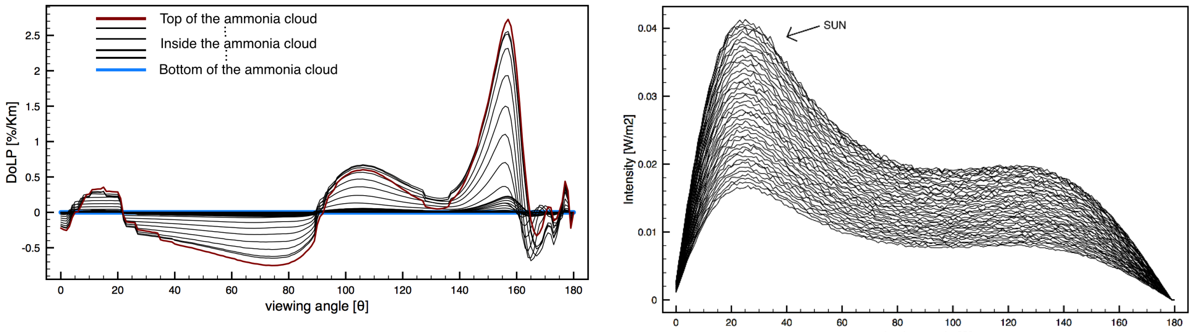

(c) Degree of linear polarization inside the ammonia ice cloud layer

(d) Intensity profile inside the ammonia ice cloud layer

Figure 4.16: Comparison of Degree of linear polarization versus the intensity profile measured inside a cloud or haze layer for Saturn's atmosphere.

4.2.2. Venus's polarization field

From Venus's model developed in Section 3.1.2, the state of polarization is evaluated using the forward model. The results are similar to the observations from the Saturn model simulation. This demonstrates the adaptability of the forward model to any planetary atmosphere and evaluates the internal field.

- Upper sulfuric acid haze: from the diffusion flux evaluated in Section 4.1.2, the flux available in the upper haze, middle cloud and lower clouds is sufficient to deduce the internal field (see Figure 4.17a:)
- Middle sulfuric acid cloud (see Figure 4.17b:)
- Lower sulfuric acid cloud (see Figure 4.17c:)
- Lower sulfuric acid haze (see Figure 4.17d:)

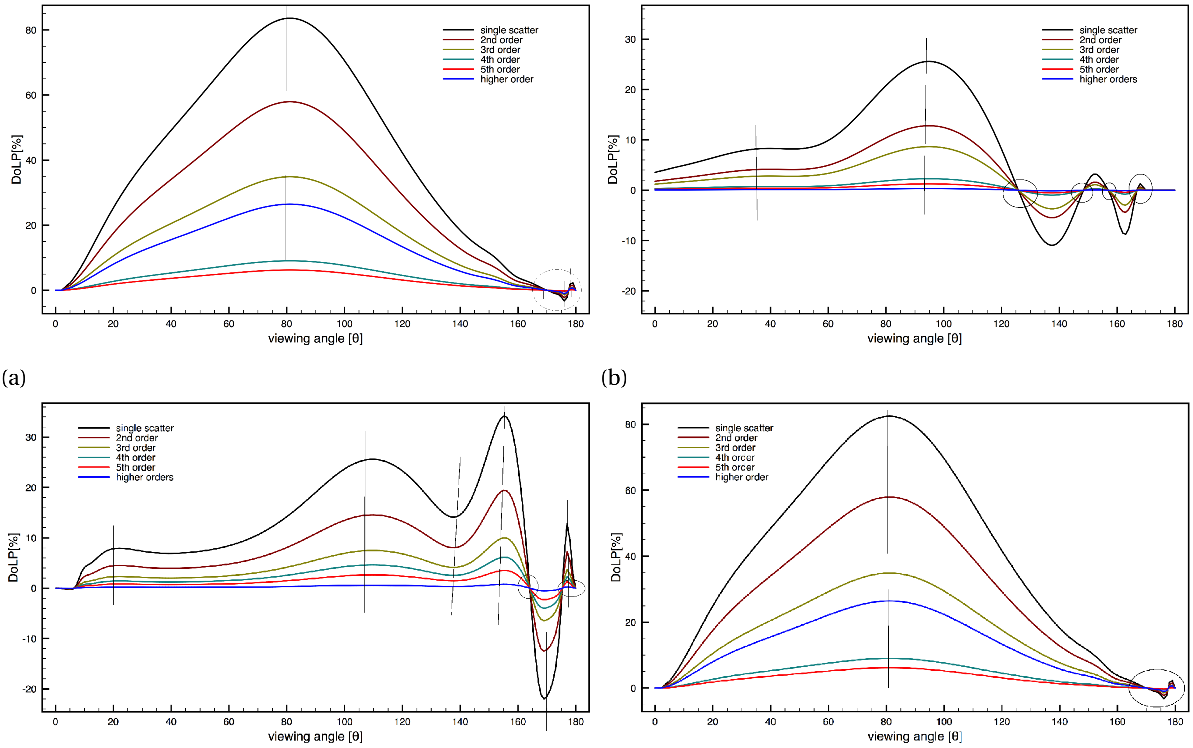

(a)

(b)

(c)

(d)

Figure 4.17: State of linear polarization for ammonia ice cloud layer of Saturn's model atmosphere at $\lambda = 0.6\mu m$

Figure 4.18: Degree of linear polarization P_l for (a) upper sulfuric acid haze layer , (b) middle sulfuric acid cloud , (c) lower sulfuric acid cloud layer , (d) lower sulfuric acid haze layer of Venus's atmosphere at $\lambda = 0.6\mu m$.

5

Instrument Concept Versus Proposal

> Science is a way of thinking
> Much more than it is a body of Knowledge.
>
> ***Carl Sagan***

Introduction

A functional prototype of a space instrument is a complex iterative development step, and purely based on the designer's experience with the science instrument, and confirming with the mission requirements such as mass, power, and costs. The designer makes performance optimization on the initial prototype by altering the properties and assessing the performance. This is repeated for several iterations until it reaches the required performance and confirms to the mission requirements.

In this chapter distinction between two instrument concept designs varied by the measurement techniques implemented are discussed and a trade-off table is developed between these two instrument concepts characteristics and how they confirm with the *HERA* mission requirements are presented. Design concept 1 is derived from the current research, with the instrument measuring the aerosol microphysical properties looking outside and utilizing the natural scattered sunlight for measurement in any planetary atmosphere. Design concept 2 is from the nephelometer instrument proposal presented for Saturn's probe in HERA mission, with this concept the aerosol sample is collected in the instrument and utilizes a source onboard for measurement.

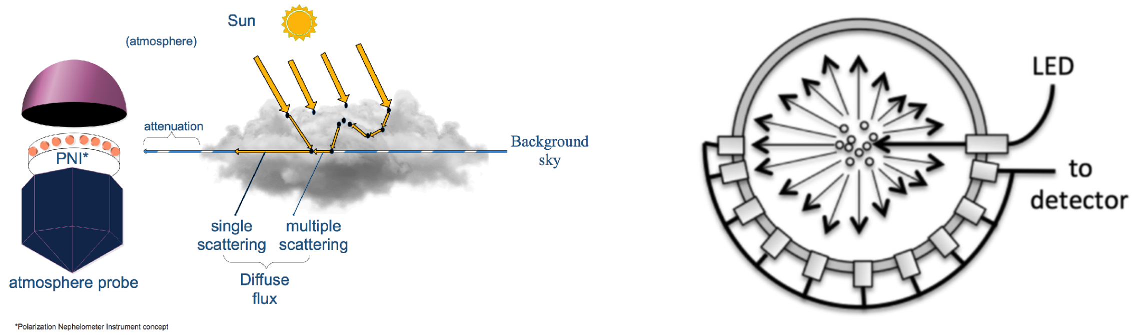

(a)

(b)

Figure 5.1: Polarization Nephelometer, (a) Design concept 1 that derives the aerosol micro-physical properties looking outside and utilizing the natural scattered sunlight for measurement. (b) Design concept 2 where the aerosol sample is collected inside the instrument and utilizes a source on-board for measurement

5.1. HERA Mission Requirement

The *HERA* mission will reveal new insights into the vertical structure of temperature, density, chemical compositions, clouds and hazes during descent in the upper and middle layers of Saturn's atmosphere. According to *HERA* mission, in situ exploration of Saturn's atmosphere addresses two themes that are far beyond the unique knowledge gained about Saturn currently: (1) the solar systems formation history and, by extension, extra-solar planetary systems, and (2) various chemical and dynamical processes in atmosphere that affect the vertical profile of temperatures, clouds and gaseous composition in planetary atmospheres[45].

The HERA mission includes a single entry probe for Saturn. For this objective, the probe consists of two-tier instruments, Tier 1 instruments are for the highest priority science goals, which include a Mass Spectrometer (MS) and an Atmospheric Structure Instrument (ASI). The Tier 2 instruments are for low priority science goals, which include Radio Science Experiment (RSE), Nephelometer, Net-flux radiometer (NFR). In the following section, the mission requirements for the nephelometer in the tier 2 instruments are presented. The general and science requirement of the mission presented here shall be valid for both the concepts.

Derived requirements for the polarization nephelometer concept 1

The above requirements are same for both the concepts, for the design concept 1 with direct measurement by looking outside the probe from the current research, additional interface requirements have to be met. The additional requirements for this concept come from the measurement technique implemented and these are listed below:

***HERA** probe Science Objective: To do an in-situ measurement of Saturn's atmosphere and derive its composition, location, thermal, and dynamical structure beginning from the stratosphere to tropopause and shall continue into the troposphere to pressures of at least 10 bars*	
Entry Probe requirements	
RQ_SR_01	The Hera probe will directly sample the condensation cloud decks and ubiquitous hazes to pressures of at least 10 [bar], whose composition, altitude and structure remain ambiguous due to inherent difficulties with remote sensing.
RQ_SR_02	The single entry location shall be Saturn's Equatorial zone on the dayside of Saturn and Earth-facing side[45].
RQ_SR_03	The launch sequence of the Saturn probe shall be from the basis of Galileo probe Figure 6.19 and the probe shall have a descend time: 75-90[min] (under a parachute)
RQ_SR_04	The probe descent altitude shall be from 100[mbar] (parachute deployment) to pressures at least 10[bar]
RQ_SR_05	The Nephelometer shall measure particle optical properties, size distributions, number and mass densities, opacity, shapes, and composition to derive the vertical structure, composition, and properties of Saturn's cloud and haze layers[45].

Table 5.1: Entry probe requirements from *HERA* mission

Performance requirements (Nephelometer)	
Spectral requirement	
RQ_SP_01	The spectral resolution of the instrument shall be in the range of 500 [nm] in visible to near-infrared wavelength range (0.4 - 1.0 [μm])
RQ_SP_02	The spectral resolution of the spectrometer used in the nephelometer shall be larger than the modulation period of the polarization signal .
RQ_SP_03	The degree of linear polarization accuracy required is 0.005 (0.5%), that shall derive the inbound fluxes within a few t.b.d nm resolution, and degree and angle of linear polarization within 10-20 nm resolution.

Table 5.2: Performance requirements related to the Nephelometer instrument on a Saturn Probe

Budget requirements	
RQ_MS_01	The instrument mass shall be less than or equal to 2 [kg]
RQ_PW_01	The instrument power shall be less than or equal to 2 [W]
RQ_DR_01	The instrument data volume shall be less than 810 kbit, and the data rate per optical head shall be less than or equal to 10 [bps]

Table 5.3: Budget requirements related to the Nephelometer instrument on a Saturn Probe

5.2. Instrument Design Concept from Research

The measurement design concept 1 is to measure the solar irradiance that is scattered in the atmosphere, and the internal field of the scattered light was evaluated in the first part of the current research. In this, the diffused flux is measured by pointing the optical heads outside. In this method, the nephelometer measures multiple scattered light rather than single scattered light. The advantages of this method are that the amount of atmospheric aerosol sample measured over the altitude is higher in comparison to the proposed concept 2 where the sample is restricted to the scatter volume and limited by the integration time of sample collections methods. The disadvantage of measuring direct diffused flux is that the diffused flux available for measurement is less in the middle/lower cloud regions of Saturn, Figure 5.2 shows the measurement techniques followed by the possible mounting configuration of the optical head for measuring the direct flux. The instrument anatomy for the measurement and the nephelometer components are shown in Figure 5.3.

Derived requirements (Nephelometer concept 1)	
Position and orientation requirements	
RQ_PO_01	The probe position along the descent altitude shall be known within an accuracy of TBD [m]
RQ_PO_02	The descent velocity of the probe is known within an accuracy of TBD [m/s]
RQ_PO_03	The probe orientation with the solar zenith angle is known within an accuracy of 0.01°
Coverage requirements	
RQ_CR_01	The number of view angles for the nephelometer shall be not less than 15 (derived from the forward model)
RQ_CR_02	The Field of View (FOV) for each optical head shall not be smaller than 1° × 1° (from FlySpex instrument[[66]])
RQ_CR_03	The viewing direction shall be parallel to the horizontal plane in the direction of the descent
Interface requirements	
RQ_IR_01	To measure the diffused flux from the atmospheric particles the nephelometer shall be located outside of the payload, and situated on the lowest part of the probe
RQ_IR_02	The optical head exposed to the outer atmosphere in the probe shall have thermal insulation to obtain a constant temperature of TBD [K] during the complete operation time

Table 5.4: Derived interface requirements for polarization nephelometer concept 1

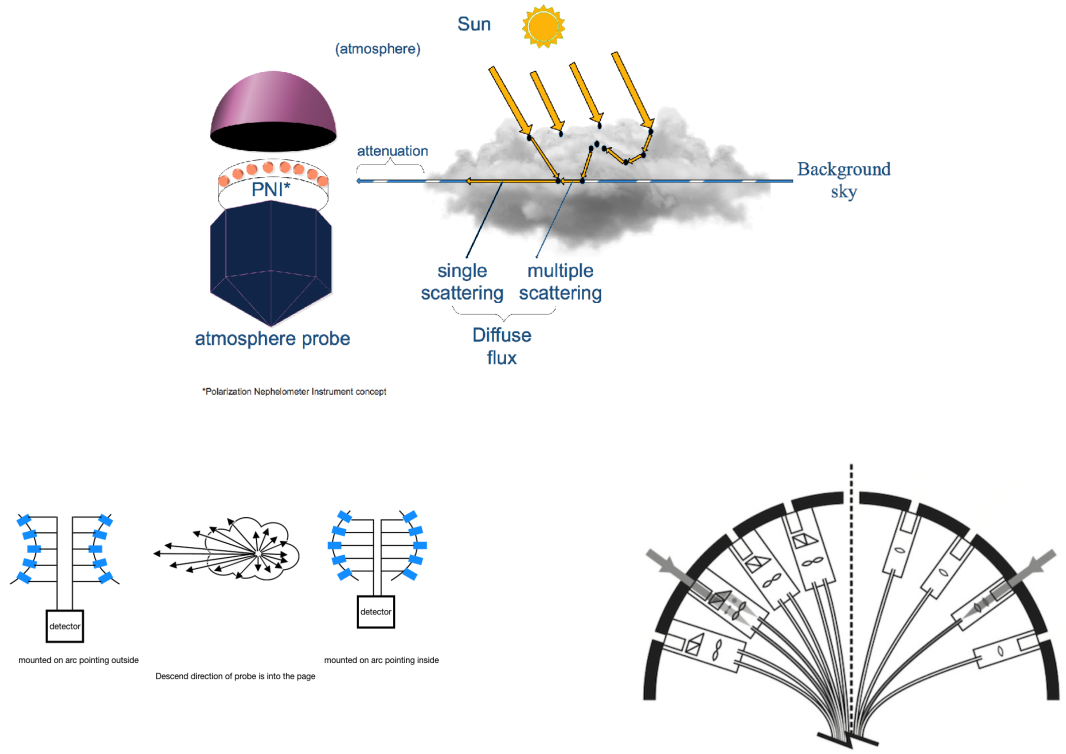

(a)

(b)

(c)

Figure 5.2: Nephelometer measurement design concept 1 with diffused flux as the measurement source and with the optical head measuring the diffused flux directly (a) and (b) possible structural arrangement concept for the optical heads mounting (c) Similar illustration from the FlySpex instrument prototype.[image source: [66]]

Strawman concept 1
The measurement concept 1 of directly sampling the atmosphere aerosol does not require an onboard source and sample acquisition subsystems. The optical head is located outside the probe. An optical fiber setup is used to transmit the modulated flux spectra from the optical head to the spectrograph. The spectrograph then focuses different wavelength on to a detector, the detector converts the incident photon to electrons that the nephelometer computer shall interpret the strengths at different wavelengths. The drawback of this method is for measuring low flux density planetary atmospheres, where the integration times are higher followed by larger background noise. In addition to these, the system throughput accounts for a larger percentage of attenuation, there are several components that contribute to the attenuation on the instrument side both the optical and electrical path, each of these are discussed in Chapter 6.

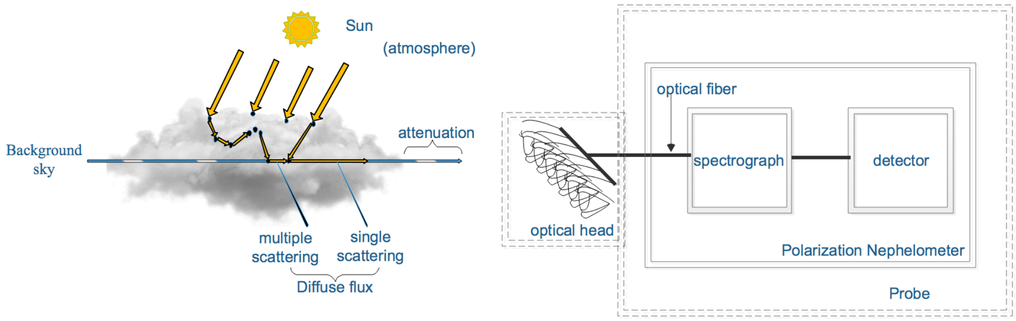

Figure 5.3: Measurement technique of the polarization nephelometer research using Strawman design concept1

- The Solar irradiance at the atmosphere for Saturn is 5.25×10^{19} $[1/(m^2 \cdot s)]$ and Venus 9.2×10^{21} $[1/(m^2 \cdot s)]$ (from Table 4.1). In this method, the Solar irradiance diffused through the dense clouds is used as the source for measuring the scattered light as shown in Figure 5.2. The internal field in Saturn's and Venus's model was evaluated and presented in Chapter 4.
- The FOV of the nephelometer instrument restricts the reconstruction of the linear polarization information. The more angles measured the better the reconstruction is [see Figure 4.9]. Each optical head from FlySpex [66] prototype is 1° × 1° and can be currently considered as the minimum field of view for our analysis. The view angles are derived from the forward model for several particles sizes and composition. The zero crossing points, peaks, and valleys at certain view angles don't change upon multiple scattering, by measuring at these angles the reconstruction is possible with a best-fit method of the current model as elaborated in Chapter 4. The forward model evaluated the minimum view angles to be measured for all the layers according to
  – Venus : 0°, 10°, 50°, 80°, 90°, 110°, 120°, 130°, 140°, 150°, 160°,170° and 180°
  – Saturn : 0°, 10°, 20°, 40°, 60°, 80°, 90°, 103°, 138°, 157°, 160°, 165°, 170° 175°, and 180°
- Two optical fibers are used to transmit the spectral modulated signal on to a spectrograph. Thermal effects on the power transmission efficiency and bend in the optical fibers, connector losses are discussed in Chapter 6.
- A spectrograph is used to obtain the required spectral resolution in the visible wavelength region. The attenuation is higher at fiber spectrograph interface. The attenuation and efficiencies of gratings are discussed in Chapter 6.
- The instrument used in low flux conditions require high integration time as seen in the case of Saturn's atmosphere. The detectors with high quantum well capacity are compared that can provide a good signal to noise ratios budget of >10 that defines the minimum required photons (SNR - value) for reconstruction of the signal.

5.3. Instrument Design Concept from Proposal

The measurement technique in the design concept 2 from the proposal to HERA mission shall collect the aerosol sample inside the instrument and measure single scattered light and uses the onboard source light (a broad bandwidth LED or laser source) for this purpose. The source light is used to illuminate a sample of atmosphere particles collected in the scattering volume, and the so assumed single scattered light is measured by the optical heads mounted on a ring and are located at different scatter angles as shown in the Figure 5.1b. This concept is similar to a scaled version of the test bench laboratory setup of the nephelometer experiment Figure 5.4b done by Muñoz [46].

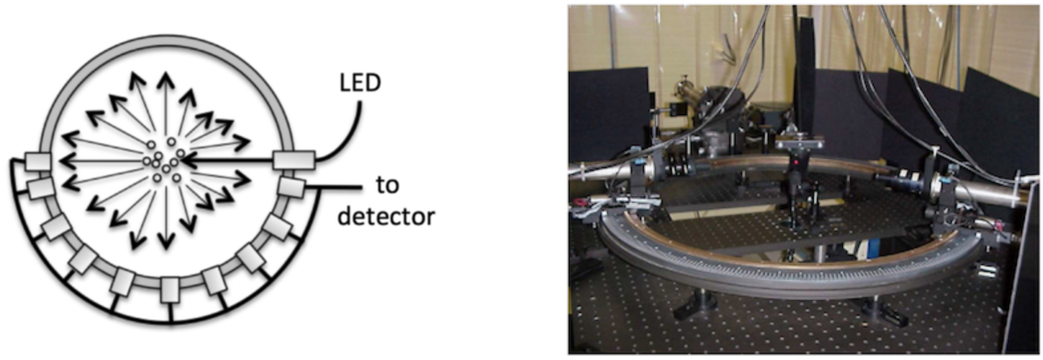

(a)

(b)

Figure 5.4: Nephelometer concept 1 with an on-board broadband source light, (a) Scaled version of the Saturn probe on-board nephelometer concept, (b) Laboratory nephelometer concept

Strawman concept 2

The measurement design concept 2 of measuring single scattered light through a scattering volume, requires a sample acquisition systems to collect the aerosol sample and an onboard light source as depicted in Figure 5.5. This measurement design concept 2 requires orifice that is projected outside to have an in and outflow of the aerosol sample. The nephelometer shall be partially located outside to sample atmospheric particles and on the lowest part of the probe, to avoid any biasing of the samples due to the flow around the probe[45]. The sample is acquired in a scattering volume and a broadband source is used to illuminate this sample. The optical head shall capture the single scattered flux. Two optical fibers are used to transmit the modulated flux spectra to the spectrograph and then to a detector.

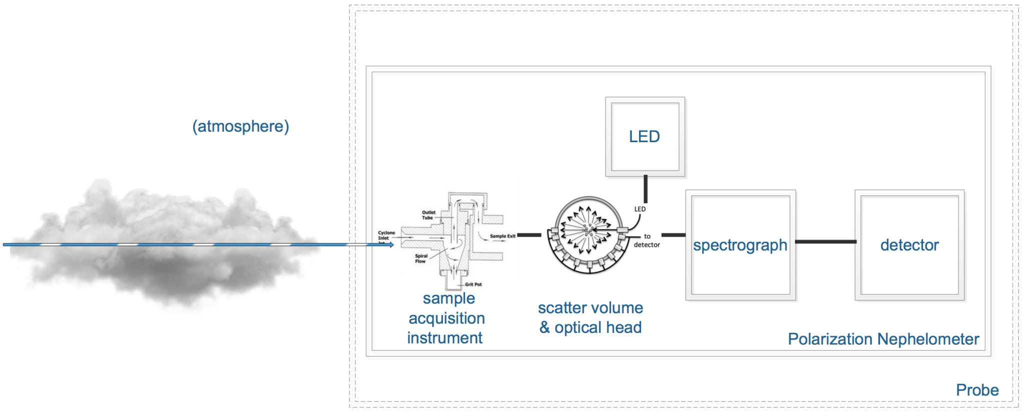

Figure 5.5: Measurement technique of the polarization nephelometer proposal using Strawman design concept2

- Aerosol sample flow to the scattering volume: this is the volume at the center of the arc. The arc has the optical heads mounted on them in a circular fashion as shown in Figure 5.4a. The sample is guided to the scattering volume with the help of a guided tube. The guiding tube consists of a chamber that initially collects the sample through the aperture (orifice) and then is guided to the scatter volume. The sample is collected until measurable density is reached within the scatter volume and then measured. The sample is let out through an exit chamber, and a new sample is collected again as the probe descends to the lower layers. There are several ways to collect the sample, inertial collectors, such as cyclones Figure 5.6a that use vortex spinning that spirals down towards a grit and as it reaches the bottom the spin reverses and smaller size particles spin in the opposite direction and exit. The spiral motion and the grits size can be tuned for the interest of aerosol particle size needed to collect. The other method is using Impactors Figure 5.6b that work on the principle that the airstreams are straight and when an impact plate is inserted in between, the larger particles collide due to inertia and the sample particles can be collected at different impact plates based on the particle size. This inertia based sample acquisition is not suitable for the current mission, due to particle collision with the impactor plate. Using a capillary action, a similar sample collection is done in the MAVEN mission to Mars, mass spectrometer NGIMS instrument [42].

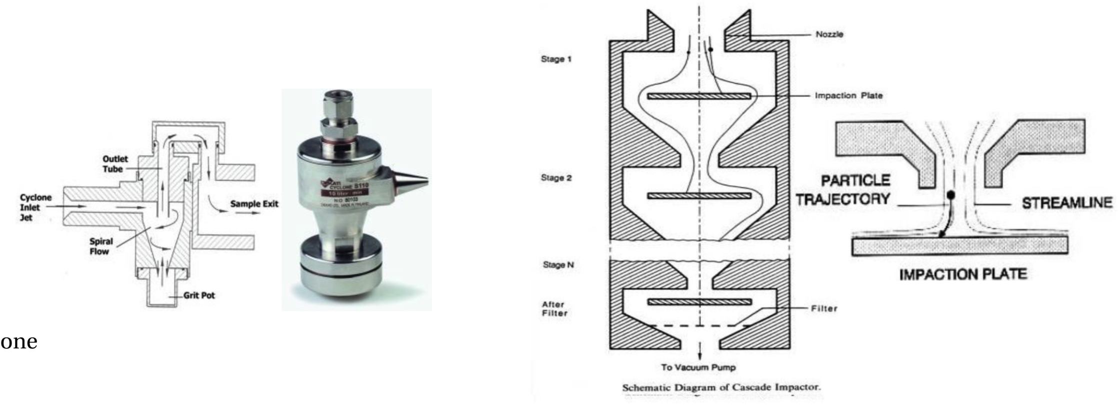

(a) Cyclone

(b) Impactors

Figure 5.6: Aerosol sample acquisition instruments using inertial techniques.[image source: [1]]

- The scattering volume is illuminated by a broadband (400 to 900nm) light source LED/Laser, the stability of this LED source is characterized before launch, and a high coherent light emitting diode is used for calibration using the fixed optical head at 0°.
- The collection optic heads are mounted on an arc that is structured around the scattering volume. The proposal considers measuring the single scattered light from the samples at 10 angles
  – Saturn : 0°, 12°, 30°, 50°, 70°, 90°, 110°, 130°, 150°, 170°
- Two optical fibers are used to transmit the spectral modulated signal on to a spectrograph then on to a detector. The detector sensitivity has less importance as a very high signal to noise ratio can be attained with the source carried onboard. The only background noise that can reach the detector is the instrument noise and the dark current effect.

5.4. Trade-off matrix

Analyzing the weakest parts of the two concepts detailed earlier to confirm the needs of the science requirements. The following comparison shall be drawn using a coarse scoring method to analyze the dissimilarities in both the concepts presented. The baseline for the instrument principle shall remain the same to measure scattered light and the polarization nephelometer shall modulate the flux spectra. These modulated spectra are later used to derive the microphysical properties of the aerosol sample measured. The difference lies with the aerosol sample volume and the source light used.

The trade-off Figure 5.7 is for performance criteria of the concepts for sample volume and the signal and source flux strengths. The concept 1 measures the atmosphere aerosol directly and has the excellent volume or range of various sample to measure, for concept 2 the sample is acquired within the instrument and the volume is limited to system volume, and the range of aerosol particles collected is based on the surroundings and descent path of the probe.

The source used in concept 1 is the natural sunlight and the total flux available at Saturn is low in the upper clouds regions and very low or extinct in the lower cloud regions as evaluated by the forward model in the current research Chapter 4. The concept 2 carries a source on-board and has an excellent source flux strength to measure the sample. The diffused flux strength available for concept 1 is very low due to the multiple scattering of the source light (sunlight). The diffused flux strength is very high as the source light undergoes only a single scatter before it is measured.

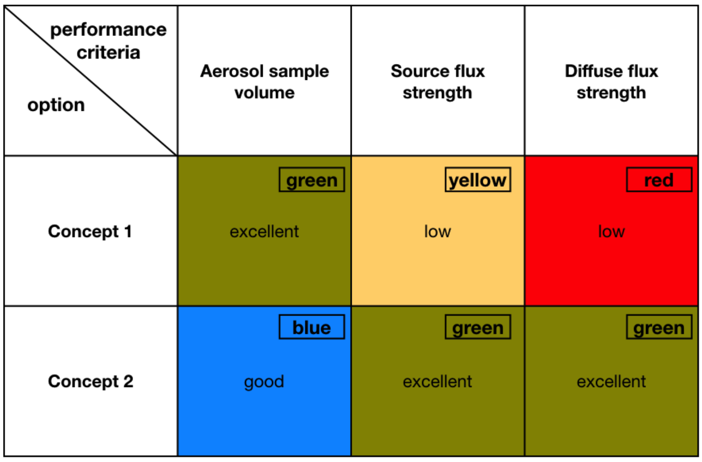

performance criteria option	Aerosol sample volume	Source flux strength	Diffuse flux strength
Concept 1	green excellent	yellow low	red low
Concept 2	blue good	green excellent	green excellent

Figure 5.7: Performance criteria trade-off table of the two polarization nephelometer concepts for Saturn's atmosphere

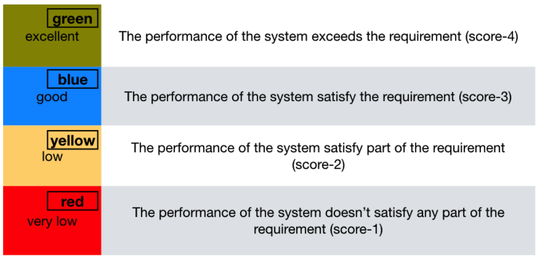

green excellent	The performance of the system exceeds the requirement (score-4)
blue good	The performance of the system satisfy the requirement (score-3)
yellow low	The performance of the system satisfy part of the requirement (score-2)
red very low	The performance of the system doesn't satisfy any part of the requirement (score-1)

The Figure 5.8 contains the design complexity trade-off for implementing the above concept instruments. The complexity of concept 1 is with the location and placement of the optical head outside the probe for measuring the diffused flux, as the design consideration has to take thermal effects, contamination and protection of the optical head and additional electronics for heating. The optical head in concept 2 is placed inside the instrument and complexity in here is with the sample acquisition system. Integration times over the sample volume are much smaller for concept 1, and for concept 2 is limited by the sample acquisition system performance.

The dynamic calibration effort is higher in concept 1 with the optical head-mounted outside. The optical head has to be characterized on the ground for making a good fit from the calibration. Measuring the direct flux and as well the polarization strength at 90° when the Sun makes a solar zenith angle of 0° with the instrument. For concept 2 the calibration is easier with an LED source carried onboard and the optical head is inside the probe. For concept 2 the optical head will be characterized on the ground and as well dynamically calibrated during the measurement. From the above trade-off table, it can be concluded that concept 1 has the drawback of very low flux for Saturn's atmosphere and is limited that is shall not meet the requirement of measuring the lower cloud regions [10bar]. This concept shall have a better performance on Venus's atmosphere as the Solar flux available is much higher than Saturn and concept 1 instrument can outperform concept 2.

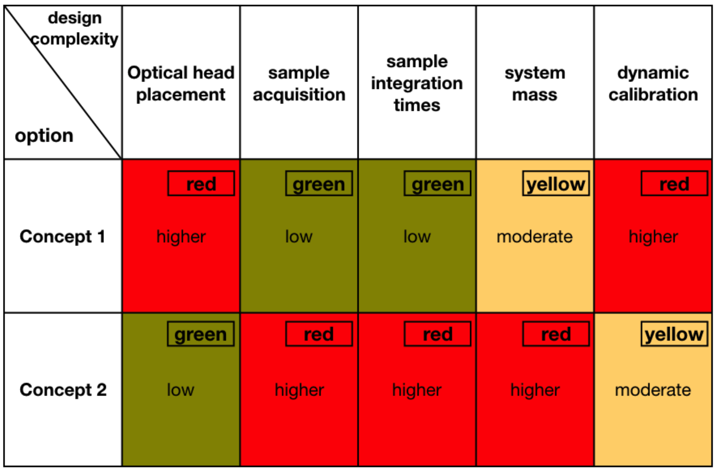

design complexity / option	Optical head placement	sample acquisition	sample integration times	system mass	dynamic calibration
Concept 1	red higher	green low	green low	yellow moderate	red higher
Concept 2	green low	red higher	red higher	red higher	yellow moderate

Figure 5.8: Performance criteria trade-off table of the two polarization nephelometer concepts for Saturn's atmosphere

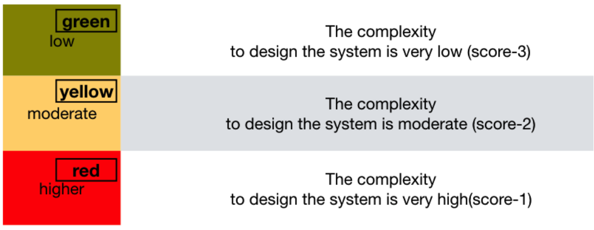

green low	The complexity to design the system is very low (score-3)
yellow moderate	The complexity to design the system is moderate (score-2)
red higher	The complexity to design the system is very high(score-1)

6

System throughput Concept 1

> You can not teach a person anything;
> You can only help him find it within himself.
>
> ***Galileo***

Introduction

System signal to noise analysis is crucial to demonstrate the feasibility of the concept 1. Derive the integration times and justify them using the signal to noise ratio budget. In this chapter, the polarization nephelometer system throughput is presented for the concept 1. An instrument end simulation is described for the measurement of the internal field evaluated in the first part of this research Chapter 4. A theoretical approach is taken in the second part to evaluate the system throughput by analyzing the photon density along the optical and electrical path of the instrument. In the current research, the system throughput analysis is done along with a single channel and a particular view angle, this can be later extended to all the view angles that shall be measured. The analysis is done over S/N, efficiency and various losses that occur in the signal along the various optical and electrical components of the instrument. The various components through which the diffused flux is transmitted to reach detector is presented in Figure 6.1 and each of these components is discussed in detail for their influence on the total system throughput.

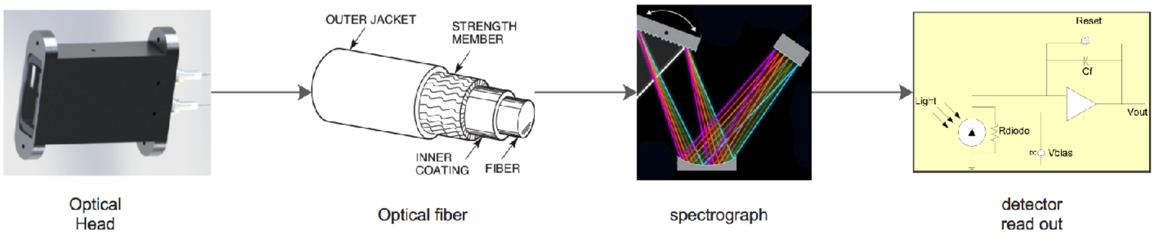

Figure 6.1: Polarization nephelometer component arrangement for measurement

The optical head encodes the polarization information on to the modulating spectrum, the optical fiber transmits the modulated flux to the spectrograph and then to the detector.

6.1. Optical head

The optical head of the Polarization nephelometer includes the optical elements needed for the polarization spectral modulation as defined in Chapter 3. The optical head consists of an achromatic quarter wave retarder, a multiple order retarder, and a polarizer. The retarder is an optical element that alters the polarization state along the propagation of light, introducing phase shift along the two components of the electromagnetic fields that are orthogonal, the phase shift is along the two orthogonal axes the fast (extraordinary n_e) and slow (ordinary n_o) axis. The retardance (Δ) of the optical element is defined as a function of the glass thickness and the refractive index along the extraordinary and ordinary axis according to Equation (6.1). In general optical elements with $\Delta = \pi$ are called the half-wave plate (HWP) and $\Delta = \pi/2$ are called the quarter-wave plate (QWP) retarders. The HWP alters the linear polarization state Q into U the polarization is mirrored along the fast axis, whereas with the QWP the exchange of U with V states and vice versa occurs.

$$\Delta = \frac{2\pi \cdot d}{\lambda}(n_e - n_o) \tag{6.1}$$

6.1.1. Optical head losses

The retarders are constructed using a birefringent material such as quartz or mica material. An effect on the retardance of the material leads to a deviation in the translation of the polarization information. There are several errors identified by G.van Harten in his Ph.D. thesis[33] component vice for the optical head. There are two major classifications of errors static (determined during calibration) and dynamic error (uncertainty in errors after calibration).

Quarter-wave retarder (QWR) - The various static errors in the QWR that mostly affect the polarization states are:

- Deviation in the retardance values as discussed earlier could lead to an incomplete transformation of U into V. This affects the net amplitude of the modulated wave for U by ~ 10^{-4}

- The other major error contributed is due to the stress in the birefringence material, causing a phase retardation and reduction in modulation amplitude of U by ~ 0.02
- The refractive index at the interface leads to differential transmission and introduces instrumental polarization along Q by a factor of $\sim 3 \cdot 10^{-4}$
- The incidence of non-normal angles also introduces different phase shifts. Reducing the modulation amplitude for U of $\sim 10^{-4}$ and instrumental polarization of $\sim 6 \cdot 10^{-3}$

The dynamic errors introduced by the QWR are:

- The highest contribution to the dynamic error is the contamination on the surface, introducing additional polarization. A 10nm layer of contamination can introduce uncertainties at non-incidental angles in the amplitude of Q in the range of $\sim 6 \cdot 10^{-5}$ of the degree of polarization is measured
- the temperature change could lead to stress changes in the birefringence and affecting the Q modulated amplitude by $\sim 2 \cdot 10^{-5}/K$

Multiple-order retarder (MOR) -The various static errors in the MOR that mostly affect the polarization states are:

- The major error contribution, in this case, is the misalignment with the other optical elements in the optical head namely QWP and the polarizer, any joint misalignment leads to a reduction in the amplitude by $\sim 2 \cdot 10^{-4}$ for Q and $\sim 4 \cdot 10^{-5}$ for U
- The refractive index affects the modulation contrast by $\sim 2 \cdot 10^{-4}$ for non-nominal incidence
- The differential transmission also introduces instrumental polarization for the Q modulated amplitude by $\sim 3 \cdot 10^{-3}$

The dynamic errors introduced by the MOR are:

- The MOR is more sensitive to temperature changes than the QWP. The temperature affects the retardance of the birefringent material that introduces errors in the phase shift and also this in-turn introduces error in the linear polarization $\sim 2 \cdot 10^{-4}/K$
- The incidence angle uncertainty is found for in-homogeneous illumination for instantaneous FOV and hence affecting the retardance and the phase shift introducing an uncertainty in the measured polarization state intensity P_L by a factor of $<3 \cdot 10^{-4}$

6.1.2. Optical head efficiency

The incident flux from the atmospheric model is presented in the Stokes formalism. The output signal (photon counts) from beam splitter analyzer is given by (I_+ & I_-) and all the polarization information is stored in the difference of these two signals $I_+ - I_-$ according to [61]:

$$\begin{aligned} I_+ - I_- &= Qf_Q(t) + Uf_U(t) + Vf_V(t) + c(I,Q,U,V) \\ \eta_{lin} &= \langle f_Q(t)^2 + f_U(t)^2 \rangle \\ \eta_{cir} &= \langle f_V(t)^2 \rangle \end{aligned} \tag{6.2}$$

where, $f_Q(t)$, $f_U(t)$, $f_V(t)$ are the functions that are integrated over time during measurements and the value reduces to zero over time, and c is independent of time. The linear and circular polarization efficiency (η_{lin} & η_{cir}) depend on the measurement and the integration time to obtain a required polarimetric precision, by varying the integration time of the measurement a value of $\eta_{lin} = 1$ is possible theoretically. However this is limited by the noise introduced by the instrument, the background source noise and the detector characteristic such as the quantum well efficiency should be large enough for obtaining a high precision over the complete integration time. The circular polarization affect was observed to be very minimal or had no affect, this is neglected for the current research. The linear polarization efficiency defined by the functions $f_Q(t)$ and $f_U(t)$ can be obtained from Chapter 3:

$$I_{\pm}(\theta,\lambda) = \frac{1}{2} I_0(\theta,\lambda)\left[1 \pm Q_0 \cos(\delta_{MOR}(\lambda,T)) + U_0 \sin(\delta_{QWP}(\lambda,T)) \sin(\delta_{MOR}(\lambda,T))\right] \tag{6.3}$$

$$\begin{aligned} &\frac{I_+ - I_-}{I_+ + I_-} T = \left[\frac{Q_0}{I_0} f_Q(t) + \frac{U_0}{I_0} f_U(t)\right] \\ &\text{Where,} \\ &f_Q(t) = \cos(\delta_{MOR}(\lambda,T)) \\ &f_U(t) = \sin(\delta_{QWP}(\lambda,T)) \sin(\delta_{MOR}(\lambda,T)) \\ &T = \text{transmittance of the unpolarized light} \end{aligned} \tag{6.4}$$

From the above equations, it can be concluded that the efficiency of the polarimeter head can be improved by increasing the integration time (photon counts) of measurement. The number of photon required can be deduced from the error budget [61] $\epsilon(Q_0/I_0) = \epsilon(U_0/I_0) = \sqrt{2/N}$. In polarimetry for astronomy, it can be found that if the polarization error is higher than 0.2% it is due to the photon statistics (N photon number). The other factor that influences the efficiency is the retardance of the optical head. The static and dynamic errors discussed earlier are the only major factors that attenuate the efficiency factor. The retardance for a quarter wave retarder (QWR) and a multiple order retarder (MOR) as a function of wavelength using quartz[28] and MgF_2[27] was constructed in the FlySpex prototype instrument for the visible wavelength range from 400-700[nm]. An optimization was done using the theoretical refractive indices of the materials with some tolerances and the plot is presented in Figure 6.2a. This method produces efficiencies that are not optimal, and are fully calibratable. The optical head transmission efficiency is plotted for the wavelength of interest and can be seen that the optical transmission efficiency (η_{lin}) is close to one

$$\begin{aligned} &MgF_2 \\ &n_e^2 - 1 = \frac{0.41344023\lambda^2}{\lambda^2 - 0.03684262^2} + \frac{0.50497499\lambda^2}{\lambda^2 - 0.09076162^2} + \frac{2.4904862\lambda^2}{\lambda^2 - 23.771995^2} \\ &n_o^2 - 1 = \frac{0.48755108\lambda^2}{\lambda^2 - 0.04338408^2} + \frac{0.39875031\lambda^2}{\lambda^2 - 0.09461442^2} + \frac{2.3120353\lambda^2}{\lambda^2 - 23.793604^2} \end{aligned} \tag{6.5}$$

$$\begin{aligned} &Quartz \\ &n_e^2 - 1 = 0.28851804 + \frac{1.09509924\lambda^2}{\lambda^2 - 1.02101864 \cdot 10^{-2}} + \frac{1.15662475\lambda^2}{\lambda^2 - 100} \\ &n_o^2 - 1 = 0.28604141 + \frac{1.07044083\lambda^2}{\lambda^2 - 1.00585997 \cdot 10^{-2}} + \frac{1.10202242\lambda^2}{\lambda^2 - 100} \end{aligned} \tag{6.6}$$

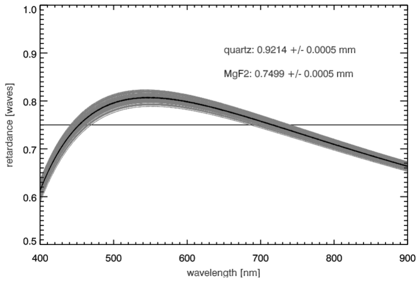

(a) Retardance of 3/4-wave achromatic quarter plate.[image source:[66]]

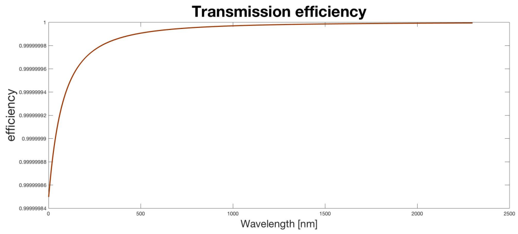

(b) The retardance efficiency for 0.2 to 2.5μm

The spectropolarimetric modulation technique advantage comes in here, in this instrument the polarization optics and spectral optics are separated. The optical head encodes the polarization information on a spectral modulated signal. Hence simplifying the usage of spectral-analysis optics, to just an analysis of the spectral resolution and range required. There are no effects of the instrument polarization after the optical head. As no moving parts are used in the optical head the errors induced due to the thickness and the material can be calibrated. It can operate over a large range of temperature without active control [66]. The encoding of the polarization information is robust for any attenuation of the signal that occurs after the optical head. The decoding could still successfully be done to obtain the Stokes parameters and the polarization information. The throughput of the optical head encoding each inbound photon can be considered close to one, as no information is lost after the optical head. The beam-splitter signals from the optical head are focused into the two optical fibers using lenses. This method maximizes the light that is injected into the optical fiber.

The modulated diffuse flux after the optical head along the two channels $[S_{+}andS_{-}]$ is as shown in Figure 6.3 for various view angles for the Saturn's atmosphere in the ammonia haze layer. The modulated signal in between the max and minimum of the two signal.

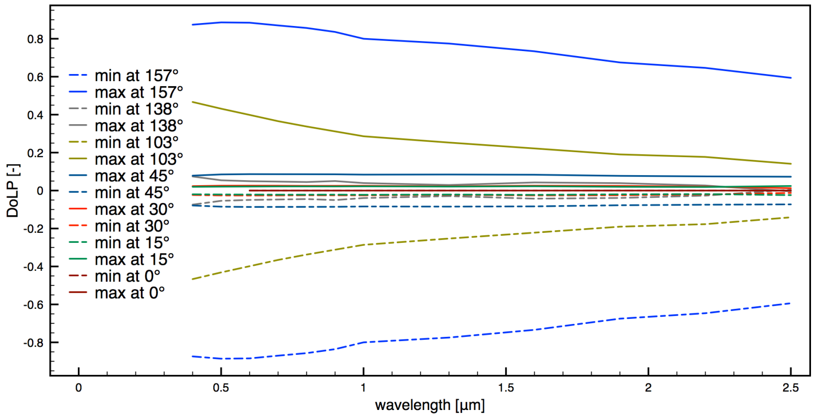

(a) Single scatter case

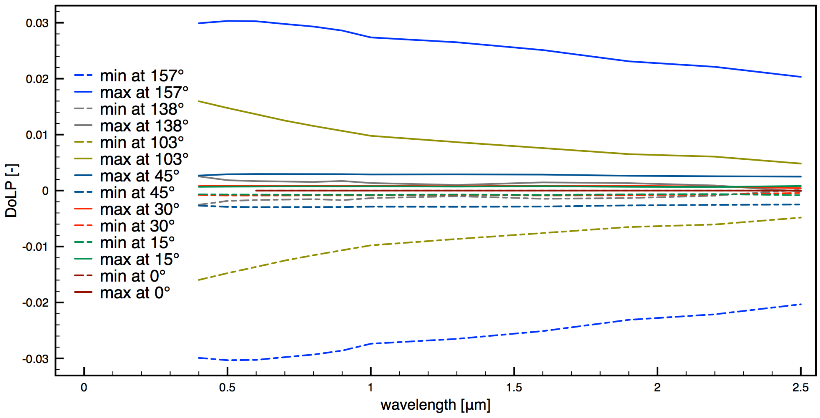

(b) Multiple scattered case

Figure 6.3: Modulated flux signal, maximum and minimum peaks for Saturn's atmosphere (a) Single scatter case and (b) multiple scattering order for the ammonia haze layer at viewing angles of 0°, 15°, 30° , 45° , 103°, 138°, 157°, as measured after the optical head.

6.2. Optical fiber

The optical fiber transmits the spectral modulated signal to the spectrograph, for an efficient transmission the optical fiber has to be checked for their performance in space instruments. There are several factors that influence the attenuation of the optical transmission in the optical fibers. This is mainly classified as the extrinsic and intrinsic attenuation losses. Further, the extrinsic losses due to the geometry and handling of the fiber can be classified as bending, launching and connector losses. The intrinsic losses due to the material type can be mainly classified as absorption and scattering losses and are proportional to the length 'L' of the fiber. Different kinds of intrinsic losses for a silicone based fiber, both theoretical and experimental values are shown in Figure 6.5.

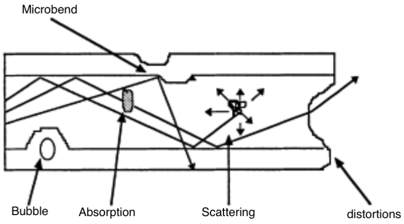

Figure 6.4: Extrinsic and Intrinsic losses in an optical fiber

- **Extrinsic losses**
  - *Bending losses:* The losses due to the distortions in the optical fiber fabrication, such as not having a straight line core. The distortions caused by micro-bends, bubbles in the materials.
  - *Launching losses:* These losses are due to the optical fiber not able to propagate the complete incoming light. The coupling is defined by the acceptance cone of the optical fiber. At the other end of the fiber, this is also defined by the coupling to the target output characteristics, there are losses with how much light is propagated to the target output.
  - *Connector losses:* The losses that occur at the coupling of the optical fiber with other materials and also with itself when extended for obtaining higher lengths. The losses could be due to the inconsistent core diameters, misalignment with the optical axis

    $$a_c(d) = -10dB\ log(\eta(d)) \tag{6.7}$$

    where $\eta(d)$ is the coupling co-efficient, eg: mismatching diameters $\eta(d) = d/D$
- **Intrinsic losses**
  - absorption losses: Theses are the losses due to the material impurities such as metal ions (ex: Cu2+, Fe3+) and hydroxyl (OH–) ions. These losses are the exponential function of length. There are several dehydration techniques used to reduce the amount OH ions. However, these impurities act as band-suppression filters, attenuating the signals at a particular wavelength (peak absorption)
  - scattering losses: These again are due to the impurities and imperfections in the code cladding junctions. These losses are also exponential functions of length Scattering losses arising due to density fluctuation of the impurities

    $$\alpha_{scat} = \frac{8\pi^3}{3\lambda^4}\left(n^2-1\right)^2 k_B T_f \beta_T \tag{6.8}$$

    where k_B is Boltzmann constant, T_f is temperature at which density fluctuations are frozen, β_T is the compressibility of the material.

    $$\begin{aligned}\alpha_{scat} &= \frac{8\pi^3}{3\lambda^4}\left(\delta n^2\right)^2 \delta V \\ \left(\delta n^2\right)^2 &= \left(\frac{\delta n}{\delta\rho}\right)^2 \left(\delta\rho\right)^2 + \sum_{i=1}^{m}\left(\frac{\delta n}{\delta C_i}\right)^2 (\delta C_i)^2\end{aligned} \tag{6.9}$$

    where $\delta\rho$ is the density fluctuation,δC_i is the fluctuation of the concentration of the i^{th} element.

Optical losses of an optical fiber also vary as a function of wavelength, the material property as detailed above due to the OH ion groups, these are observed as the attenuation peaks at 1.24 and 1.39 [μm] due to the absorption from OH group gas molecules as seen in Figure 6.5a.

The total attenuation losses can be evaluated for the instrument by adding up the individual losses in the fiber according to Equation (6.10), following which the total Power budget can be evaluated using Equation (6.11) [13]:

$$a_{TOT} = a_{CL} \cdot N_{CL} + a_{SL} \cdot N_{CL} + a \cdot L + a_{SM} \tag{6.10}$$

(a)

(b)

Figure 6.5: Optical power transmission losses in an optical fiber. (a) various loses measured for a SiO_2 fiber (b) spectral losses against $(1/\lambda^4)$ (c) Transmission losses in the SiO_2 optical fiber for theoretical and experimental evaluation

- a_{CL} is the connector losses and N_{CL} are the number of connectors used in total. Typical allowed value of the connector losses is 0.75dB per connector. For the nephelometer instrument, two connectors are required.

- a_{SL} is the splice losses, N_{Sl} are the number of splicers used in total. Typical allowed value of the splicer losses is 0.2dB per splicer. For the nephelometer instrument, one fusion splicer is required that fuses the fiber from individual optical head to the common fiber that runs to the spectrograph.

- $a{\cdot}L$ is the intrinsic losses from scattering, absorption and bending losses determined from experiments, and L is the length of the fiber
  Single Mode fiber

  - 1310 nm fiber loses 0.5 [dB/km].
  - 1550 nm fiber loses 0.4 [dB/km].

  Multi-Mode fiber

  - 850 nm fiber loses 3.0 [dB/km].
  - 1300 nm fiber loses 1.0 [dB/km].

- a_{SM} is the safety margin included for compensating the losses due to temperature changes and radiation effects. Typical value of 3dB is used.

$$P_{out} = P_{in} \cdot 10^{\left(-\frac{a_{TOT}}{10dB}\right)} \tag{6.11}$$

where P_{in} input optical power coupled to the fiber, P_{output} optical power remaining after propagating length L of the fiber, a_{TOT} = total attenuation losses of the fiber in [dB/km]

The preliminary estimations of the losses in optical fiber for single and multi-mode fibers are presented here.

- For a single mode fiber power budget

$$\begin{aligned} a_{TOT} &= 0.75[dB] \cdot 2 + 0.3[dB] \cdot 1 + 0.5[db/km] \cdot 0.001[km] + 3.0[dB] \\ a_{TOT} &= 4.8005[dB] \\ P_{out} &= P_{in} \cdot 0.3311 \end{aligned} \tag{6.12}$$

- For a multi-mode fiber power budget

$$\begin{aligned} a_{TOT} &= 0.75[dB] \cdot 2 + 0.3[dB] \cdot 1 + 3[db/km] \cdot 0.001[km] + 3.0[dB] \\ a_{TOT} &= 4.803[dB] \\ P_{out} &= P_{in} \cdot 0.3309 \end{aligned} \tag{6.13}$$

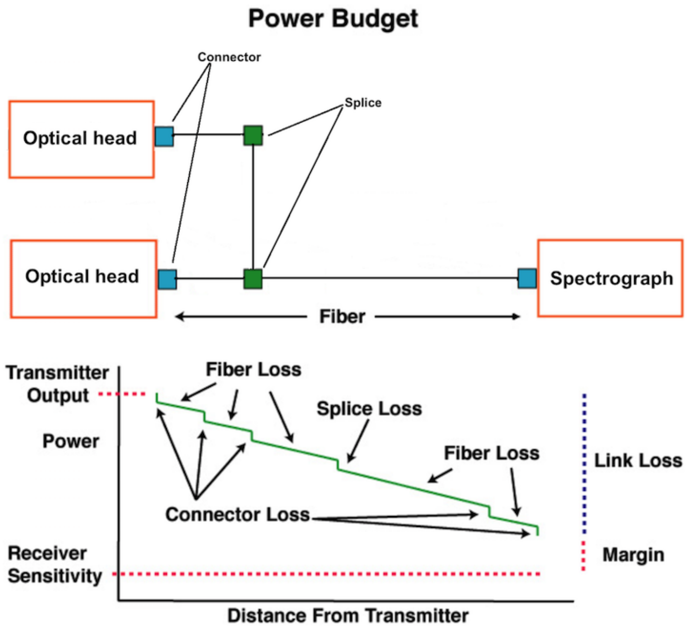

Figure 6.6: efficiency's and losses for an optical fiber

The throughput or efficiency of the optical fiber is 0.33 considering a 3dB noise safety margin budget. The COTS optical fibers can be used and for the nephelometer instrument application and for their qualification in space. The space systems engineering approach can be used to validate the component for space qualification [21]. The first step is to develop system requirement, that define the critical component parameters and that quantify the optical performance. Under this section, the power budget requirements are evaluated for the optical fiber performance considering general fiber losses and various environmental requirements. The second step is the environmental requirements such as the mechanical, thermal, and radiation effects (the worst case conditions). Followed by a failure mode analysis that defines the boundary conditions and parameters for the COTS optical fiber. The final step is to develop the test methods and test plans to experimentally validate the components through the failure modes and boundaries for the COTS fiber taken.

6.3. Spectrograph

Optical spectrometers split the intensity of light as a function of wavelength and frequency. This is done by using the refraction or diffraction property of the light wavefront, and the delay of these wavefronts as they pass through an optical medium such as prism and diffraction grating respectively. There are several optical spectrometers that are used for astronomical observations according to and as detailed in [14]:

- Grating and phased arrays: These type of waveguides, continuously delay a part of the wavefront and these wavefronts interfere constructively onto different location onto a detector. This are the most commonly used in spectrometers due to their simple construction Figure 6.8a

- Fabry-Pérots and cavities, in these the wavefronts are progressively delayed over reflective surfaces and are recombined later Figure 6.8b
  Semi-integrated MEMS-based Fabry-Pérot spectrometers are commercially available. This type of MEMS spectrometer allows for tuning the cavity to the desired wavelength, but have a limited spectral range Figure 6.7. In [76] A second concept is discussed that used 16 Fabry-Pérot on the same chip and a fixed cavity spacing, where the resolution can be reached to a few hundred. These MEMS-based FP can be used in an array for a higher field of view measurements, but are limited for usage due to moderate resolution.

- Fourier transform spectrometers: Using Fourier transformation the wavefront is split into two parts and with a variable delay they form interference fringes that are recombined Figure 6.8c

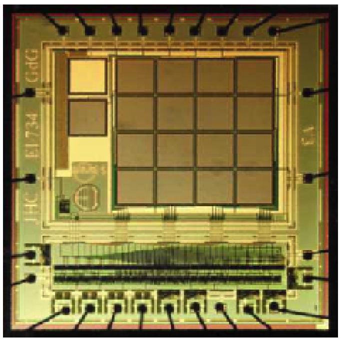

Figure 6.7: MEMS based optical mini spectrometer

- Direct detection: Different detectors can directly measure the photon energy as a function of wavelength

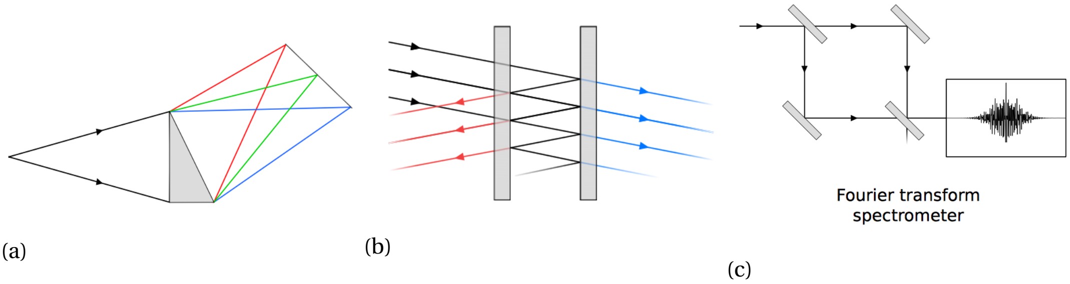

(a)

(b)

(c)

Figure 6.8: (a) Grating and phased arrays, (b) Fabry-Pérots and cavities, (c) Fourier transform spectrometer

The resolution of the spectrometers is directly proportional to the delay caused by each waveguide as a function wavelength according to $R = \frac{\lambda}{\delta\lambda}$. The direct detection is limited to resolution and the current technology shall support only a resolution in the range of 5-100. The advantage of this technique is that they require less number of pixels for detection. However, given this resolution range, it limits its usage for nephelometer instrument. Fourier spectrometers are not used for nephelometer given the limitation from the fringe patterns generated during interference and recombining. This brings us to the high-resolution Fabry-Pérots and diffraction grating spectrometers.

6.3.1. Diffraction efficiency

The efficiency of a grating can be defined as energy flow of the incoming monochromatic source light that is diffracted into the order being measured. The efficiency curve can be defined as the absolute or relative efficiency of diffraction versus the diffracted wavelength at specific diffraction order 'm'. The peak occurs at the blazing wavelength (λ_B) as shown in Figure 6.9a

The diffraction efficiency of a reflection grating depends on the grating profiles factors such as the groove depth, the grating period, the refractive index of the grating material. From theoretical evaluation gratings with 100% efficiency are possible. However, practically this is not the case and there are other losses due to the material construction and the environment surrounding the grating. The diffraction efficiency as a function of various grating profiles is shown in Figure 6.10a.

The transmission diffraction gratings also have good diffraction efficiency. The efficiency for transmission grating was evaluated using rigorous coupled-wave analysis (RWCA) by [44] are presented in figure

The grating efficiency can be fine-tuned and optimized for a particular diffraction mode for a blazed grating, this method produces a good approximation for the diffraction efficiency at a particular order. Blazed grating also known as Echelle grating is a special type of gratings, where the depth of the groves is optimized

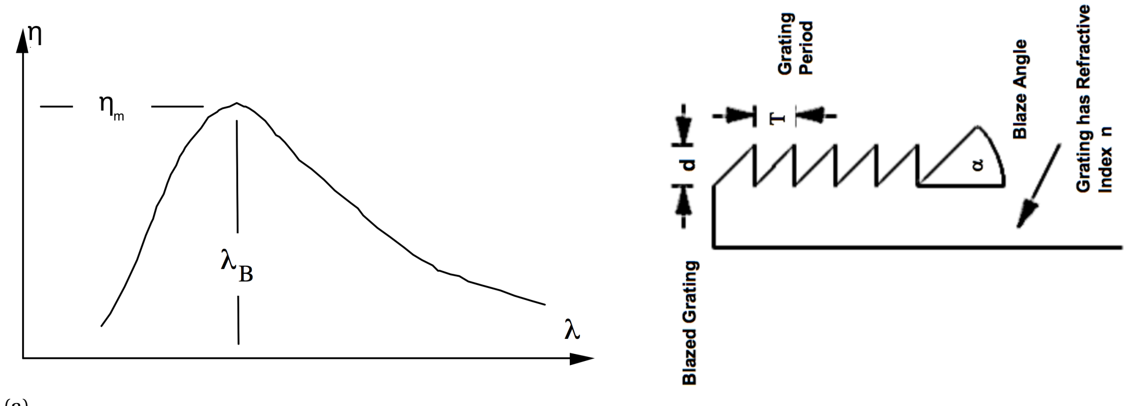

(a)

(b)

Figure 6.9: Diffraction grating efficiency. (a) A simplified efficiency curve E, as a function of diffracted wavelength at specific diffraction order 'm' [48], (b) Blazed grating geometry, where D is the blazed thickness

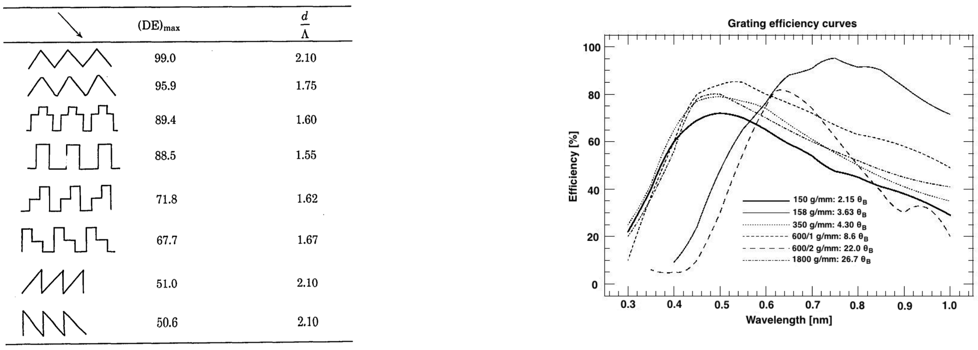

	(DE)$_{max}$	$\frac{d}{\Lambda}$
	99.0	2.10
	95.9	1.75
	89.4	1.60
	88.5	1.55
	71.8	1.62
	67.7	1.67
	51.0	2.10
	50.6	2.10

(a)

(b)

Figure 6.10: (a) Maximum Transmitted First-Order (m=1) Diffraction Efficiency's for Various Grating Profiles. Incidence is at first Bragg angle, $\theta = 30°$ [44], (b) diffraction grating efficiency curves for different grating periods (optimized at specific blazed angle)

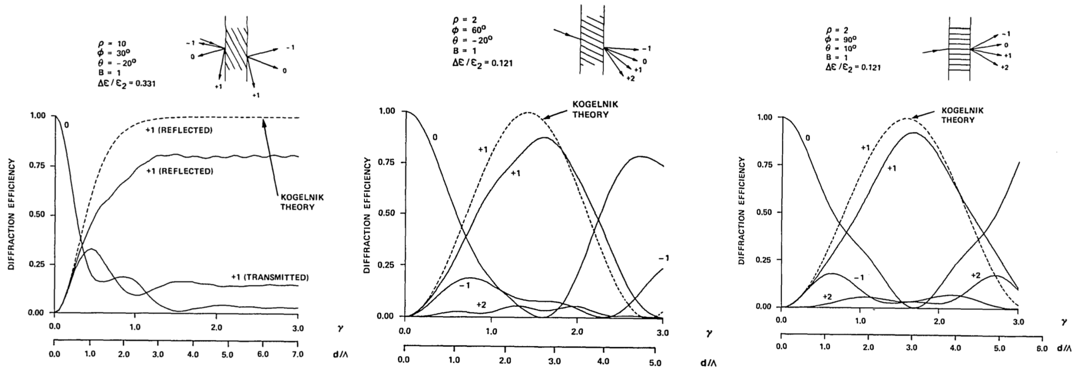

(a)

(b)

(c)

Figure 6.11: The diffraction efficiencies of the transmitted waves for pure transmission grating at (a) $\theta = 30°$, (b) $\theta = 60°$, (c) $\theta = 90°$

to produce maximum grating efficiency at a particular diffraction order. In evaluating the diffraction grating efficiency the following assumptions are considered. The simulation is carried using a monochromatic incident. The corrugated region is considered to be infinitely long and periodic. All the incident waves are taken to be planar wavefront. The classical diffraction analysis is conducted with the plane of incidence perpendicular to the grating grooves source, other incident angles are not considered. The grating surface and the surrounding media are assumed to be isotropic in nature. The grating efficiency of a blazed grating is according to:

$$\eta_m = \left[\frac{sin\left(\pi T\left(\beta - \frac{m}{T}\right)\right)}{\pi T\left(\beta - \frac{m}{T}\right)} \right]^2 \qquad (6.14)$$

$$\beta = \frac{(n-1)\,d}{\lambda T}$$

where η_m is the grating efficiency at diffraction order $'m'$, T is the grating period, $'n'$ is the refractive index of the material, $'d'$ is the blaze thickness, and λ is the wavelength of the light

A performance evaluation of the blazed grating is done for the wavelength range of interest λ = 0 to 1.0 [μm] as a function of the blaze thickness (blaze wavelength) is presented in Figure 6.12. For the first simulations the refractive index of the material is taken as 1.5 and a grating period of 3[μm], it is observed that the blaze wavelength shifts to higher wavelength when the depth of the grooves is increased, also it is seen that the mean efficiency (area under the curve) also increases with groove height. For the second simulation, the refractive index was varied (different material), a grating period of 3[μm] and with a depth of the grating groove as 1[μm] to have the blazed wavelength at the 500[nm] mid-point of the wavelength range of interest. In the second case, a similar observation is seen, it is observed that the blaze wavelength shifts to higher wavelength when the increasing the refractive index, also it is seen that the mean efficiency also increases with refractive index.

An optimized value for the groove depth for different refractive indices is evaluated, to obtain the maximum mean efficiency over the wavelength. It is observed from the simulation that a mean efficiency of 50% can be reached. The groove depth has to be decreased as the refractive index increases to obtain a nice Gaussian distribution around the 500[nm] wavelength range. The optimal groove depth values are found to be, d=1.868[μm] (n=1.3), 1.128[μm](n=1.5), 0.934[μm](n=1.66), 0.56[μm](n=2.0). By utilizing a blazed diffraction grating for the spectrograph, with a blazing angle at 500 [nm] can produce an average efficiency of 0.5 over the visible wavelength of interest.

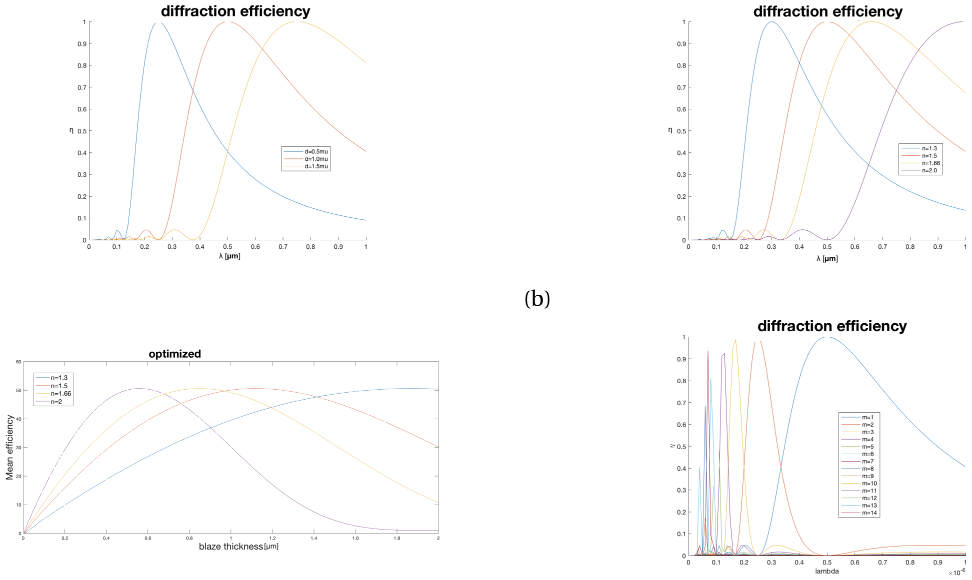

(a)

(b)

(c)

(d)

Figure 6.12: Diffraction grating efficiency optimized for specific mode as a function of blazing angle- (a) with varying the depth of the grooves (n=1.5) (b) with varying the refractive index (the material used) (d=1.0[μm]),(c) Optimized groove depth for various materials (different refractive index), (d) efficiency for different diffraction modes with depth D=1.128μm and refractive index n=1.55

6.4. Detector SNR budget

System throughput of a nephelometer instrument depends on several factors, the first factor is from the optical part of the instrument, which includes the optical head, the optical fiber used for transmission and the spectrograph. This optical setup efficiency provides a factor of how much light is reaching the detector. The second part consists of the electrical part of the instrument a detector, the detector efficiency depends on the amount of charge generated per photon termed as the quantum efficiency, this depends on the type of material used for the detector, such as Silicon (*Si*), Mercury Cadmium Telluride (*HgCdTe*), Indium Antimonide (*InSb*). The second's parameter is the charge collection area, determined by the pixel size definition. The third parameter is the charge transfer, this is the amount of the charge measured per pixel, the maximum charge holding capacity of a detector is defined as the full well capacity $[e^-]$. The fourth factor is the amplification factor and the digitization of the charge collected per pixel (readout). The Figure 6.13 shows a comparison table for various detector types, based on the four factors mentioned earlier. For the comparison theoretically evaluated performance value are taken.

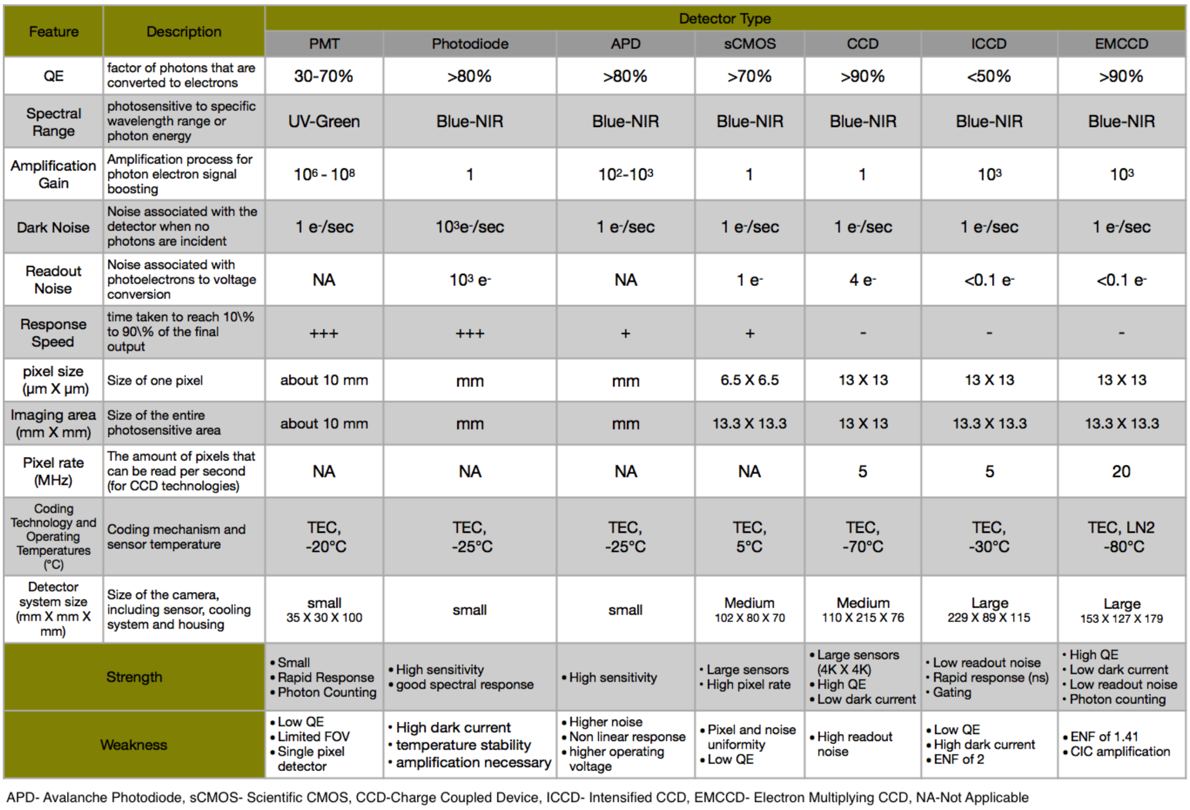

Feature	Description	Detector Type						
		PMT	Photodiode	APD	sCMOS	CCD	ICCD	EMCCD
QE	factor of photons that are converted to electrons	30-70%	>80%	>80%	>70%	>90%	<50%	>90%
Spectral Range	photosensitive to specific wavelength range or photon energy	UV-Green	Blue-NIR	Blue-NIR	Blue-NIR	Blue-NIR	Blue-NIR	Blue-NIR
Amplification Gain	Amplification process for photon electron signal boosting	10^6 - 10^8	1	10^2-10^3	1	1	10^3	10^3
Dark Noise	Noise associated with the detector when no photons are incident	1 e^-/sec	$10^3 e^-$/sec	1 e^-/sec	1 e^-/sec	1 e^-/sec	1 e^-/sec	1 e^-/sec
Readout Noise	Noise associated with photoelectrons to voltage conversion	NA	10^3 e^-	NA	1 e^-	4 e^-	<0.1 e^-	<0.1 e^-
Response Speed	time taken to reach 10\% to 90\% of the final output	+++	+++	+	+	-	-	-
pixel size (µm X µm)	Size of one pixel	about 10 mm	mm	mm	6.5 X 6.5	13 X 13	13 X 13	13 X 13
Imaging area (mm X mm)	Size of the entire photosensitive area	about 10 mm	mm	mm	13.3 X 13.3	13 X 13	13.3 X 13.3	13.3 X 13.3
Pixel rate (MHz)	The amount of pixels that can be read per second (for CCD technologies)	NA	NA	NA	NA	5	5	20
Coding Technology and Operating Temperatures (°C)	Coding mechanism and sensor temperature	TEC, -20°C	TEC, -25°C	TEC, -25°C	TEC, 5°C	TEC, -70°C	TEC, -30°C	TEC, LN2 -80°C
Detector system size (mm X mm X mm)	Size of the camera, including sensor, cooling system and housing	small 35 X 30 X 100	small	small	Medium 102 X 80 X 70	Medium 110 X 215 X 76	Large 229 X 89 X 115	Large 153 X 127 X 179
Strength		• Small • Rapid Response • Photon Counting	• High sensitivity • good spectral response	• High sensitivity	• Large sensors • High pixel rate	• Large sensors (4K X 4K) • High QE • Low dark current	• Low readout noise • Rapid response (ns) • Gating	• High QE • Low dark current • Low readout noise • Photon counting
Weakness		• Low QE • Limited FOV • Single pixel detector	• High dark current • temperature stability • amplification necessary	• Higher noise • Non linear response • higher operating voltage	• Pixel and noise uniformity • Low QE	• High readout noise	• Low QE • High dark current • ENF of 2	• ENF of 1.41 • CIC amplification

APD- Avalanche Photodiode, sCMOS- Scientific CMOS, CCD-Charge Coupled Device, ICCD- Intensified CCD, EMCCD- Electron Multiplying CCD, NA-Not Applicable

Figure 6.13: Comparison of different detector technologies, and advantages and disadvantage of these technologies.

The choice of detector follows from the optical throughput of the instrument and the source signal strength and as well the required signal to noise (SNR). From the earlier section, the efficiencies and losses in the optical signal are evaluated. The optical throughput as a function of wavelength is evaluated from Equation (6.15) and is shown in Figure 6.14. In this section, the efficiency and losses of a detector (electrical signal) are evaluated and finally, the complete system throughput is evaluated according to Equation (6.16)

$$P_S = P_0 \cdot T_{SP} \cdot T_{OF} \cdot T_{DG} \tag{6.15}$$

Where,
P_S = The number of photons from the signal at the detector
P_0 = The number of photons at the entrance of the instrument
T_{SP} = transmission factor from the optical head
T_{OF} = transmission factor from the optical fiber

T_{DG} = transmission factor from the diffraction grating

$$S = P_S \cdot QE \cdot G \cdot t_{int} \tag{6.16}$$

Where,
S = the electrical signal measured $[e^-]$ QE = The quantum efficiency of the detector, the amount of electrons generated per photon collected
G = The amplification stage gain factor
t_{int} = the integration time of detector

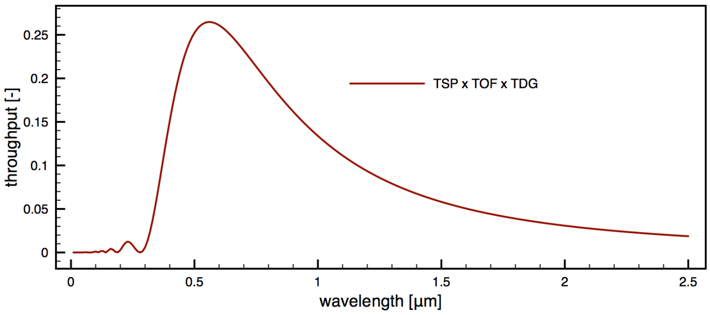

Figure 6.14: Optical throughput as a function of wavelength for the polarization nephelometer concept 1 (direct measurement).

The strengths and weakness of various detectors are compared in Figure 6.13, photodiode, APD (Avalanche photodiode), CCD (Charge coupled device) have a higher sensitivity. However, photodiodes have very less quantum efficiency and less stable with temperature, the higher operating voltage requirement and the non-linear response of APD's makes it not suitable for the low flux density measurement in the current direct measurement concept 1. The sCMOS (scientific Complementary Metal Oxide Semiconductor) are very noisy, less sensitive and have a very low dynamic range than CCD's, the advantage is that each pixel has it's own readout register and have additional electronics on the same pixel. For this case like most of the astronomy observations, CCD is used as the detector for the high QE, sensitivity and linear response over a high dynamic wavelength range.

CCD is currently a standard device to measure and register an optical digital signal from domestic to scientific purposes. The linear response of the CCD over a large wavelength range to the incident light makes CCD a great advantage for using it in astronomy applications [75]. There are several types of CCDs available, such as front0illuminated, back-illuminated, full frame and frame transfer [11]. In general, the characteristic of CCD is known for its linearity, quantum efficiency, gain and with the current advancement in technology readout noise can be reduced and with commercial CCD's a value of $2-3e^-$ is reached. The quantum efficiency for these type of CCD detectors from many studies is shown in Figure 6.15a

The total noise is the sum of the individual noises according to:

$$N_{total} = \sqrt{\left(S + n_{dark}^2 + n_j^2 + n_{th}^2 + n_{reset}^2 + n_{preamp}^2 + n_{ADC}^2\right)} \tag{6.17}$$

The noise contribution from the signal (shown in green) itself doesn't affect the overall signal budget, the noises shown in blue depend highly on the integration time and the errors scale with the increasing integration time. In low flux density measurement the integration time is crucial to have a good signal to noise ratio ($SNR > 10$) that is the minimum requirement to reconstruct with some statistical approach, the noises shown in blue shall be the type of noise that affects the SNR in the current research of direct measurement concept 1. The remaining noises shown in orange are the fixed amount noise per readout and don't change over integration and can be compensated for the error introduced during static calibrations.

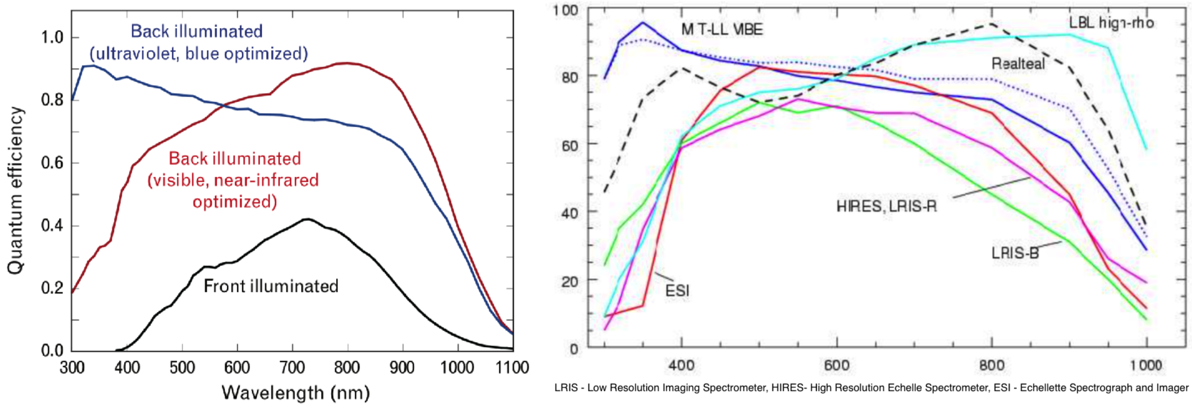

(a)

(b)

Figure 6.15: (a) Quantum efficiencies of front-illuminated CCDs and back-illuminated CCDs optimized for short and long wavelengths [17]. (b) Quantum efficiency of current and future CCD'd used in astronomy at Keck Observatory

6.4.1. SNR evaluation for Saturn's atmosphere

In this section, two commercial detectors in general used for evaluating the signal to noise ratio at test bench set-up for astronomical observations are used to do a comparative study for the current direct measurement concept. The first detector is SBIG STXL6303E, which has a very high linear detector type as demonstrated in [51]. The second detector is been used with SPEX prototype designing, as the current concept uses similar modulation technique for the polarization information as done in SPEX instrument.

$$SNR = \frac{S \cdot t_{int}}{N_{total}} \tag{6.18}$$

CCD detector SBIG STXL6303E is used for the first analysis with a peak quantum efficiency of $QE = 68\%$. The linear response to the incident light of the detector was determined to be (R2 =99.99%), its effective gain is at $1.65 \pm 0.01 e^{-}/ADU$ (ADU: Analog to Digital Units) and its readout noise is $12.2e^{-}$. This detector is precise for astronomical measurements and forms a good choice for baseline evaluation. The noise budget for this CCD detector is in Table 6.1 and evaluated signal to noise ratio as a function of wavelength is shown in Figure 6.16a

The signal to noise analysis using a CCD detector QImaging retiga 4000r[6] for secondary analysis. This detector is similar to that of the COTS detector that was used for the SPEX prototype design [33]. The noise budget is analyzed for the CCD and presented in the Table 6.2. The SNR is evaluated as a function of wavelength and the detector chosen, with an integration time of one second. The SNR budget thus evaluated is presented in the Figure 6.16b

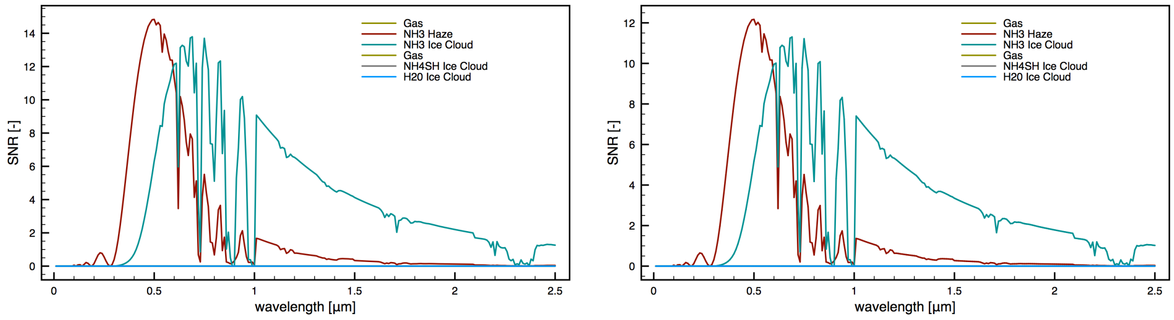

(a)

(b)

Figure 6.16: The SNR budget for each layer as a function of wavelength for Saturn's atmosphere with respect to two CCD detectors (a)using CCD detector SBIG STXL6303E and (b) uisng QImaging Retiga 4000r the integration time taken is t_{int} = 1 milli-sec

Signal Shot noise				
Shot noise	n_{shot}	$\sqrt{P_S}$	451.3 e-	$P_S = 2.0 \cdot 10^5$ $T_{SP} = 0.95, T_{OF} = 0.33$, $T_{DG} = 0.85$ (from simulation)
Detector noise				
Dark current noise	n_{dark}	$\sqrt{I_{dark} \cdot t_{int}/q}$	0.3e-	[5]
Johnson Noise	n_j	$q^{-1}\sqrt{(2 \cdot k_B \cdot T \cdot t_{int}/R_{diode})}$	1.79e-	with $R_{diode} = 10^{17} ohms$ @ 298K
Thermal background signal				
Thermal noise	n_{th}	$\sqrt{I_{th.bq} \cdot t_{int}/q}$	0.73e-	with $I_{th.bq} = 8.6 \cdot 10^{-20}$ @ 298K
Electronics and Digital noise				
Reset noise	n_{reset}	$q^{-1}\sqrt{(k \cdot T \cdot C)}$	13.5e-	@ 20MHz [5]
Digitization noise	n_{ADC}	$\frac{LSB}{\sqrt{16}}$	6.1e-	16 bit ADC, full well 100000e-
Total Noise			473.72e-	

Table 6.1: Noise budget for the reference CCD detector SBIG STXL6303E

Signal Shot noise				
Shot noise	n_{shot}	$\sqrt{P_S}$	451.3 e-	$P_S = 2.0 \cdot 10^5$ $T_{SP} = 0.95, T_{OF} = 0.33$, $T_{DG} = 0.85$ (from simulation)
Detector noise				
Dark current noise	n_{dark}	$\sqrt{I_{dark} \cdot t_{int}/q}$	1.64e-	[6]
Johnson Noise	n_j	$q^{-1}\sqrt{(2 \cdot k_B \cdot T \cdot t_{int}/R_{diode})}$	1.79e-	with $R_{diode} = 10^{17} ohms$ @ 298K
Thermal background signal				
Thermal noise	n_{th}	$\sqrt{I_{th.bq} \cdot t_{int}/q}$	0.73e-	with $I_{th.bq} = 8.6 \cdot 10^{-20}$ @ 298K
Electronics and Digital noise				
Reset noise	n_{reset}	$q^{-1}\sqrt{(k \cdot T \cdot C)}$	12e-	@ 20MHz [6]
Digitization noise	n_{ADC}	$\frac{LSB}{\sqrt{12}}$	9.76e-	12 bit ADC, full well 40000e-
Total Noise			477.22e-	

Table 6.2: Noise budget for the reference detector QImaging Retiga 4000r

Uncertainty analysis

From the SNR budget analysis using the two detectors to have SNR > 10 the integration time is > 1[msec]. The uncertainty in the signal measured can be obtained from the SNR analysis, if the SNR is 100 then the measured signal is excellent and the error in signal is 1%, if the SNR is 10 then the error in the measured signal is 10%, this is the relative errors in the signal measured (1/SNR). A better estimate is the uncertainty estimation for photometric observations done and can be obtained from the Equation (6.19) [41] or alternatively from the magnitude uncertainty estimation Equation (6.20) [16]. The former method usually overestimates the uncertainty by a factor, while the later underestimates the uncertainty. Overestimation is always better and is also a personal preference to have good signal sample at the end of the measurement.

$$\delta q_1 = \sqrt{\sigma_{BS-S}^2 + \left(\frac{1}{SNR}\right)^2} \tag{6.19}$$

where, δq - uncertainty in the signal measured, and σ_{BS-S}^2 = the standard deviation of the flux measured between the background signal and the actual signal being measured. Here the background signal is taken as the unpolarized light intensity (I_{unpol}) while the signal being measured is the polarized light intensity (I_{unpol}), a three sigma value is used for the evaluation here to find the worst case uncertainty value.

$$\delta q_2 = \pm 2.5 \log\left(1 + \frac{1}{SNR}\right) \tag{6.20}$$

The uncertainty analysis for the SNR evaluated earlier in this section for the two detectors compared using both the uncertainty estimation is shown in Figure 6.17

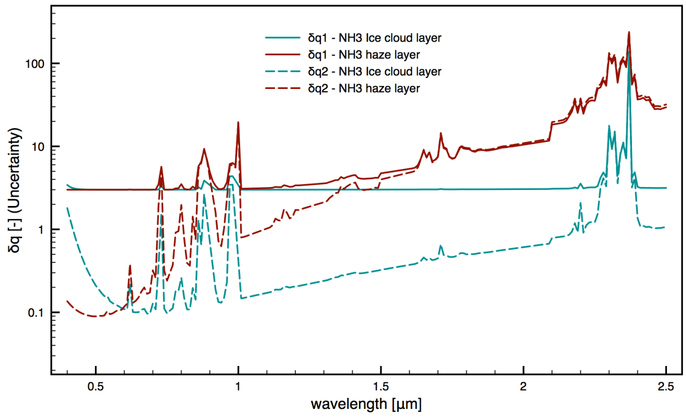

Figure 6.17: Uncertainty in the signal measured with the second detector Table 6.2 from the SNR budget two cases are presented uncertainty estimation method 1 (over estimates- Equation (6.19)), and method 2 (under estimates- Equation (6.20)).

For concept 1 to measure the diffuse/scattered flux, the signal to noise ratio at the detector has to be sufficient enough to meet the requirement RQ_SP_03. From the earlier SNR budget evaluation for integration time $t_{int} = 1[ms]$, it is seen that the uncertainty obtained with such signal to noise ratios is close to 10% for much of the wavelength range and reaches >50% at certain wavelength, as seen at $1.0\mu m$ and wavelength > $2.0\mu m$. The uncertainty has to be improved for the wavelength of interest $\lambda = 0.4 - 1.0\mu m$. This can be done by either by increasing the integration times and/or by using the advanced CCD technologies that are present such as the EMCCD (Electron Multiplying CCD) and the *L3CCD* (LowLight Level CCD). The uncertainties in both the cases are discussed below and how the SNR increases for both the cases.

Scan line displacement and integration times

The nephelometer direct measurement concept is to measure the P_l in the horizontal plane of the descent trajectory. In addition to the detectors noise the viewing geometry and the scanning sequence could induce some misregistration in the signals and lead to errors. For the current nephelometer design the viewing direction geometry doesn't introduce any errors such as the panoramic effect (curved flat effect), that is the sample pixel size ($P_c \times P$) increases when viewed at other than the normal view angle, that is the sample resolution increases as the area viewed by the detector is higher. The viewing geometry changes with the winds that are perpendicular to the probe inducing a drag on the probe along the descent trajectory. This needs actual trajectory reconstructed from the probe data, and later a correction can be applied for reconstructing the vertical structure of the atmosphere along this descent trajectory. The SNR budget is not affected much in this cases. The scanning sequence could affect the SNR and increase uncertainty in the signal measured due to the descent speed and displacement of the instantaneous scan line. The nephelometer detector on the probe scans through the atmosphere in a push-broom mode also know as along-track scanning. The instantaneous scan line time along the descent of the probe should be less than the displacement time of the probe. This instantaneous scan line time gives the upper boundary for the integration time.

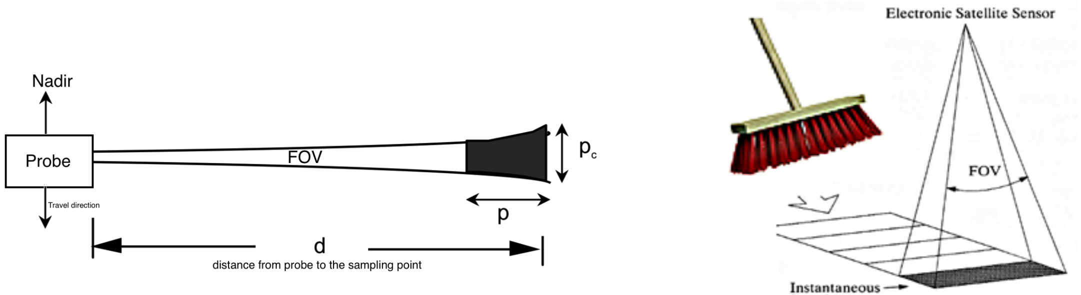

(a) Nephelometer viewing direction along the horizontal plane of the decent trajectory

(b) Galileo probe, descent and deployment sequence. Basis for Saturn's probe

Figure 6.18: The nephelometer direct measurement concept 1 in the horizontal plane using a push broom concept

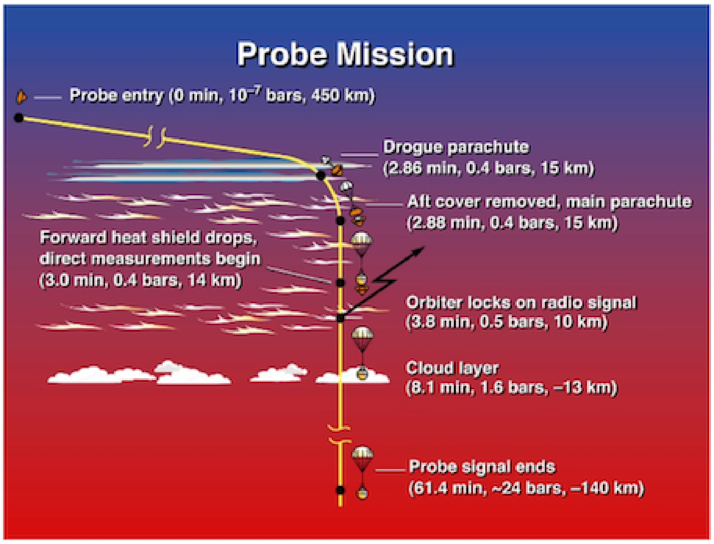

Figure 6.19: Galileo probe, descent and deployment sequence. Basis for Saturn's probe

The probe descent profile for the Saturn's probe shall be designed similar to that of Galileo probe Figure 6.19. From the *HERA* mission, the estimated mass of the probe (descent module) from a dimensional scaling and regression fit analysis is $m_pp = 199 - 215[kg]$, and the deceleration module is 200 [kg], and the preliminary studies give the foreshell with a 1m diameter [45]. The required Saturn's probe descent time to reach 10bar in the atmosphere is 75-90 minutes. The average decent velocity $\overline{v}$ of the probe to reach 10 bar or 550 km (scale height height at Saturn for 10 bar) from the top of the atmosphere can be calculated according to Equation (6.21):

$$\overline{v} = \frac{\int_0^h v(h)dh}{h} \tag{6.21}$$

$$v(h) = \sqrt{\frac{2 \cdot m_pp \cdot g}{\rho_{air} \cdot C_d \cdot S_{Ap}}}$$

where, $\overline{v}$ = average decent velocity, h is the final altitude expected to reach = 550 [km], $v(h)$ parachute terminal velocity at an altitude of h [m], m_pp is the mass of the probe and the main parachute 250 [kg]

$(m_p + 15\% m_p)$, g is the gravitational acceleration of Saturn = $10.44[m/s^2]$, ρ_{air} density of dry air evaluated at Saturn's pressure and temperature, for 1 [bar] and 134 [K] the $\rho_{air} = 0.190 kg/m^3$, C_d is the drag coefficient of the parachute and probe, S_{Ap} is the surface area of the parachute, $C_d \cdot S_{Ap}$ is called as the drag area and from the Galileo probe mission this is $5.921 m^2$[59]. The average decent velocity derived with this configuration was 67.1 [m/s] and a total decent time of 135.34 [min] with the main parachute from 0.5 [bar] to 10 [bar]. This evaluation doesn't consider the wind speeds in the Saturn's atmosphere, which reach upto 400 [m/s]. The decent velocity as a function of pressure is shown inFigure 6.20.

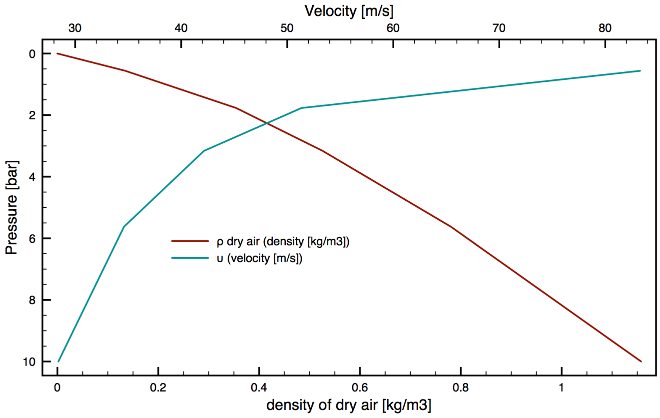

Figure 6.20: axis 1 atmosphere density as a function of pressure in Saturn's atmosphere, axis 2 decent velocity of the probe as a function of pressure

The nephelometer instrument measures the scattered light inside a cloud, the sampling volume shall be very close to the probe. The sampling area for the optical head with a field of view of 1° × 1° is in the range of $0.03 - 3.5[m^2]$ for a sampling distance of $10 - 100[m]$ from the probe. The Nephelometer in general measures a sample of volume. For the current analysis the photons which reach from a sample area of $1 m^2$ is considered. The SNR budget evaluated earlier (see Figure 6.16) is an average value obtained when the signal is integrated for $t_{int} = 1[milli - sec]$ over a sample area of $1 m^2$.

The scan line displacement during the integration time of 1 [milli-sec] can be derived from the average decent velocity, and the displacement is 0.0671 [m]. The probe scan line displacement along the trajectory is proportional to the integration time and given by $t_{int} \cdot \overline{v}$. The time taken by the probe to descend to the next scan area is ≈ 14.9[milli-sec]. This analysis shows that the higher integration time of >1 [milli-second] is possible, but the effective sample area measured reduces and increasing the uncertainty of the sample set integrated before moving to scan the next line. The integration time of 5 [milli-sec] gives a good SNR of >10 over the wavelength range $(0.4 - 1.0 \mu m)$. The improved SNR and reduction in uncertainties for both detectors discussed earlier are shown in Figure 6.21.

Advancements in CCD technology

The CCD technology is used for astronomy observation more than ever as discussed earlier in this chapter. In this section, the advancements in CCD, such as EMCCD and *L3CCD* to do observations of very low flux density objects is discussed. Both technologies increase the signal using amplifiers or gain registers. These processes are stochastic in nature as the individual gain applied per pixel cannot be known exactly, only mean gain is known. This produces additional leaving an uncertainty in the SNR value. Here the *L3CCD* is discussed in detail,

L3CCD stands for low light level CCD's, this type of CCD have an on-chip gain. This type of signal amplification on-chip reduces the readout noise to $< 1e^-$, giving an edge over the other types of CCD's such as intensified CCD and slow-scan CCD's. The thermally generated noise from the dark current and the amplification noise are the major two components for the temporal noise factors in CCD's. The amplification noise can be dealt by adjusting the output node capacitance. Using the current state of the art the amplification noises can reduce to $< 2e^-$ [50]. The dark noise, in general, can be reduced by cooling the detector, the other

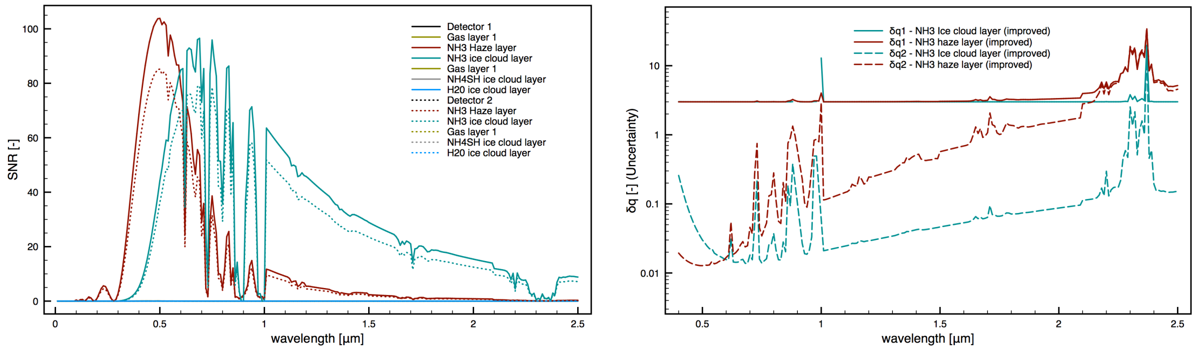

(a) SNR for integration time $t_{int} = 5$ [milli-sec]

(b) Uncertainty improvement with integration

Figure 6.21: The SNR budget for each layer as a function of wavelength for Saturn's atmosphere with respect to two CCD detectors (a) SNR over the integration time of 5 [milli-sec] (b) the uncertainty reduced with the integration over time for the second detector Table 6.2 (for worse case before integration see Figure 6.17)

methods are to use interval mode operation (IMO) and multi-phase pinned (MPP). In this *L3CCD* technology the amplification is applied prior to the output node using on-chip register gain (see: Figure 6.22). With every shift (n) in the register there is a probability of signal multiplication according to the gain $\overline{G} = (1+p)^n$ [22]. The mechanism is that as the photons are shifted along the register and say ϕ_2 the photon multiplication occurs from impact ionization. This amplification makes an effective increase in the signal as if the quantum efficiency of the system has increased. This amplification on-chip reduces the readout noise as well according to Equation (6.22):

$$\sigma_{eff} = \frac{\sigma_{real}}{G} \tag{6.22}$$

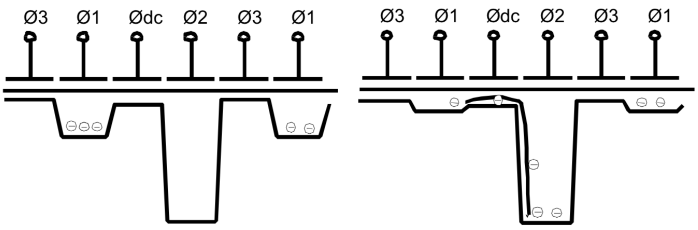

Figure 6.22: *L3CCD* on-chip gain register for photon amplification[50]

This amplification using on-chip gain gives a statistical behavior on the SNR, by introducing additional noise factor as shown in Equation (6.23). When G is very large the noise factor increases to such that the effective SNR is halved. There is a photon counting technique used to overcome this noise factor such as the IMO or MPP methods[50]. The *L3CCD*'s using the photon counting techniques in [22] can read low values at 0.5 $pixel^{-}1$ $readout^{-}1$ using a single threshold processing strategy on the output signal. This threshold value is derived from the mean gain of the output signal and accepting only those above this threshold.

$$\begin{aligned} F &= \sqrt{\frac{2(G-1)}{G^{\frac{N+1}{N}}} + \frac{1}{G}} \\ SNR &= \frac{S}{\sqrt{F^2 S + F^2 T + \frac{\sigma^2_{real}}{G^2}}} \end{aligned} \tag{6.23}$$

where, G is the gain, T is the thermal noise in $[e^-/\text{pixel}]$, σ^2_{real} is the readout noise of the CCD in $[e^-]$

The Figure 6.23 shows the comparison of an image detected by *L3CCD* and image from an intensifier connected CCD (ICCD) for a low flux measurement. It can be seen from the picture taken with *L3CCD* gives no background signal and a very sharp image.

Figure 6.23: Comparison of an image detected by CCD65 (a *L3CCD*) and image from an intensifier connected CCD (ICCD) for a low flux measurement[50].

Evaluating the signal to noise ratio using a L3CCD, with a pixel size of 512x512 (CCD65 [8][19]). This has a 512 (n) shift register, even with a probability of 1% a huge gain of 163.14 can be reached ($\overline{G} = (1+0.01)^{5}12$). The additional noise factor than introduced due to the stochastic multiplication is given by Equation (6.23) and the factor F=1.4054 the thermal noise and readout noise are taken as 1 [e^{-}], even though the paper suggests a value of $\sigma < 0.1$ is possible for the worst case analysis the theoretical values are taken, then the uncertainty in the signal and the SNR evaluated for L3CCD from the forward model is as shown in the Figure 6.24

$$SNR_{L3CCD} = \frac{S \cdot t_{int} \cdot \overline{G}}{\sqrt{N_{total}^{2} + F^{2} \cdot S + F^{2} \cdot T + \frac{\sigma_{real}^{2}}{G^{2}}}} \tag{6.24}$$

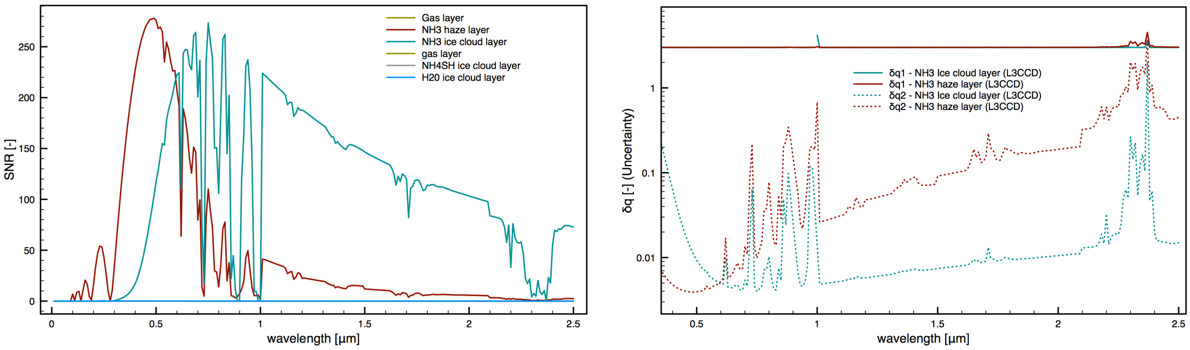

(a) SNR for integration time $t_{int} = 1$ [milli-sec]

(b) Uncertainty improvement with L3CCD

Figure 6.24: The SNR budget for each layer as a function of wavelength for Saturn's atmosphere with respect to L3CCD (a) SNR over the integration time of 1 [milli-sec] (b) the uncertainty of L3CCD (for worse case before integration see Figure 6.17)

The L3CCD gives an excellent signal to noise ratio at integration times $t_i nt = 1$ [milli-sec] and the uncertainty is reduced to less than 2% for the visible wavelength region. The SNR for the two CCD's was on average <10 at an integration step of 1 [milli-sec], and improved with the increase in integration times and from the model a minimum of 5 [milli-sec] integration time is needed to increase the average SNR value to >10. Later the SNR was re-evaluated using a low light level CCD and an average SNR of >50 is obtained for the visible wavelength range. From the optical and electrical path throughput analysis for the visible wavelength range, it can be observed that the signal to noise strengths of >10 is achievable and it may be possible to measure the upper and middle layers of the Saturn's atmosphere (1-2[bar]) for certain. However, for the lower clouds layers(>2[bar]), the L3CCD can be used to boost the low flux for a possible measurement. Though the current L3CCD are used as ground-based observation of very faint stars. This gives the possibility of higher integration times (>1000 [sec]) and a data set to be evaluated from statistics. The L3CCD needs a feasibility study to determine the possibility of measuring the lower cloud region <2[bar]. From a theoretical approach of worst-case analysis, an average system throughput of 0.2 was estimated, and this value shall improve from here as more systems are tested for the polarization concept 1 of direct measurement.

6.4.2. SNR evaluation for Venus's atmosphere

The available Solar flux at Venus is ~ 200 times higher than that of Saturn's atmosphere. The SNR budget analysis also confirms with this, the SNR budget evaluation for the two CCD's (see :Table 6.1 and table 6.2) is shown in the Figure 6.25. The uncertainty with the higher estimation method is <3% for Venus's atmosphere. From the forward radiative transfer model and the SNR analysis, it can be concluded that the direct measurement concept 1 can be used for Venus's atmosphere at all altitudes.

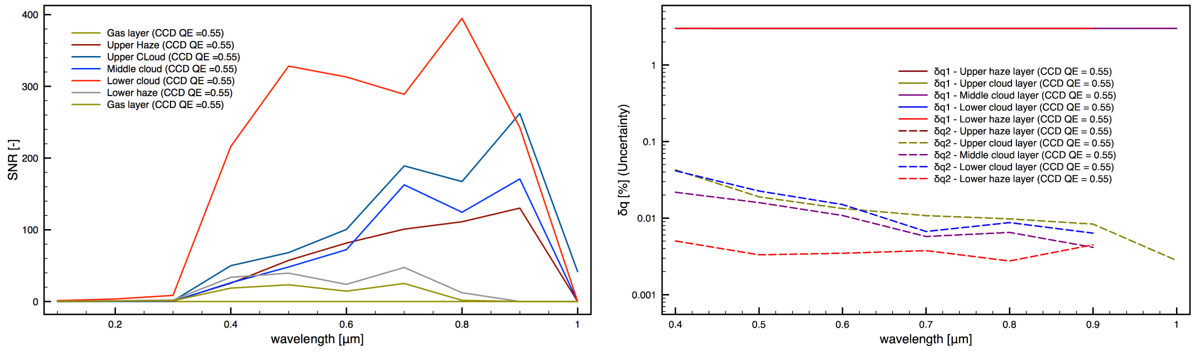

(a) SNR for integration time $t_{int} = 1$ [milli-sec] for CCD specified in Table 6.1

(b) SNR for integration time $t_{int} = 1$ [milli-sec] for CCD specified in Table 6.2

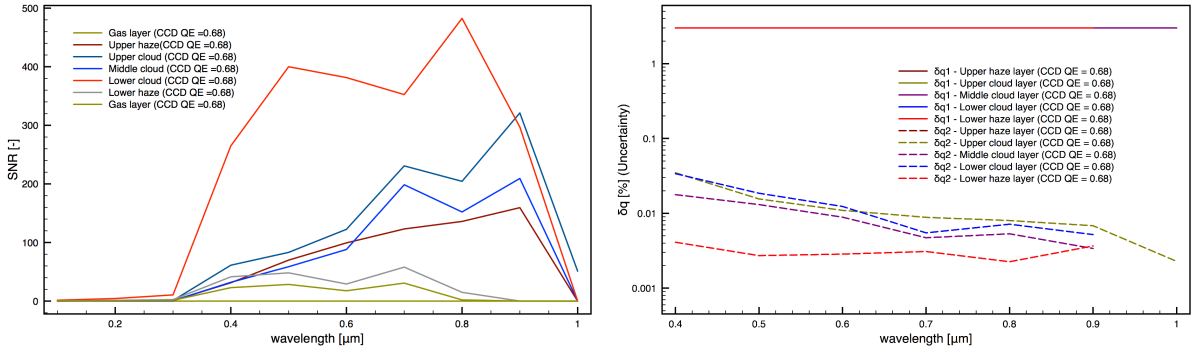

(c) Uncertainty for CCD specified in Table 6.1

(d) Uncertainty for CCD specified in Table 6.2

Figure 6.25: (a) & (c) The SNR budget for each layer as a function of wavelength for Venus's atmosphere over the integration time of 1 [milli-sec], (b) & (d) the uncertainty values with the two CCD's for Venus.

7

Conclusion

Look up at the stars and not down at your feet.
Try to make sense of what you see, and wonder
about what makes the universe exist.
Be curious.

Stephen Hawking

This chapter brings us to the end of the current thesis research work. The research objective was to evaluate the feasibility of the new direct measurement technique for a nephelometer, in low flux density atmospheres. For this the current research was conducted in two parts, first part was to develop a radiative transfer model for Saturn's and Venus's atmosphere, and evaluate the internal field along the vertical structure of the aerosol and haze layers in the atmosphere. The second part consisted of analyzing the instrument throughput in measuring this internal field. For this, the optical throughput was evaluated with a theoretical approach, and the electrical throughput was done with theoretical values and a comparative study with CCD detectors was done.

7.1. Conclusion

The conclusion consists the summary of the results derived from the two parts of the current research, internal field evaluation and system throughput analysis of the signal to noise ratio,

Internal field

From several fly-by and remote observation of Saturn, gives us a top-cloud topographical understanding of its atmospheric composition. There exists uncertainty with the composition of Saturn, as there is no in-situ data available yet. From several theoretical and experimental approach, three major layers are predicted in Saturn's atmosphere. To evaluate the internal field the radiative transfer model for Saturns atmosphere was constructed in detail for upper, middle and lower clouds layers up to 10 bar as a function of wavelength, from the molecular and aerosol scattering and absorption thicknesses that are derived. Following this the internal field was evaluated, the internal field evaluation scheme was unique in the sense giving a detailed internal field as seen from the inside of the clouds and hazes. Which was not possible with double-adding and other methods that evaluated the field on the top-cloud topographical approach. With this research model the internal field was generated in the detector view and evaluated as the detector descends inside a cloud/hazes along the horizontal view plane. The Saturn's atmosphere is limited to only 14.91 [w/m2] of Solar flux reaching the top of the atmosphere. The penetration of the Solar flux is limited due to thick clouds and the flux reaches close to zero at 2[bar] as predicted from the atmosphere radiative model developed in this research. The internal field evaluated in the multiple scattering cases is still measurable with a lower precision of 5% in DoLP maybe possible to measure the diffuse flux in the middle layers of the Saturns atmosphere to ~ 2 [bar] as seen from the forward model evaluation. For lower layers, the diffused flux is very minimal for measurement. The *HERA* mission planned to deliver a probe inside the Saturn's atmosphere can reveal more insights of the internal field. Then a revisit to this research model can be done for a comparative analysis on Saturn's model. The in-situ measured data can be used to reduce the uncertainty in the atmosphere model that currently exists. This forward radiative transfer model developed in this research is new as it evaluates the internal polarization field structure as seen inside a cloud/haze and there exists no such model yet for a comparative analysis and/or as a validation to the model developed here.

System throughput analysis

In the second part of the thesis, the direct measurement concept using a nephelometer was studied. The feasibility of the concept for Saturn's atmosphere in terms of signal to noise ratio was developed, for this the input signal was taken from the earlier radiative transfer model developed for Saturn with the multiple scattering cases. The advantage of this direct measurement technique is the higher sample volume that can be attained, as the instrument measures looking outside the probe. For this purpose, the system throughput for the optical and electrical part was considered. Firstly the optical throughput was evaluated for the instrument using a theoretical approach. The optical throughput of *0.2* was obtained considering the worst case losses in the optical components. Following this, the electrical output was evaluated using theoretical quantum efficiency's and a comparative study with commercial CCD's was done.

The direct measurement technique measure in the horizontal plane of the decent trajectory. For Saturn, the flux available is very small (14.91 [W/m2]), and the decent profile of the probe with the viewing angle of the nephelometer instrument limits the integration time of a sample volume. This limitation on integration time is due to the radial velocity errors of the probe introducing scan line displacements for the nephelometer. That is the probe moves to the next scan line before the detector could scan the current line. Excluding the geometrical errors, the scanning error was evaluated and the upper boundary for the integration times is 7.45 [milli-sec] to integrated the sample over 50% of the same scan area. The SNR improvements with a minimum integration time of 5 [milli-sec] were evaluated to obtain an average SNR of >10. This needs a further study on the predicted probe trajectory and probe trajectory under wind-speeds. The SNR was further improved to >200 with the aid of L3CCD's that can detect low flux levels, however, the photon counting method employed in these type of CCD's have a stochastic signal amplification, and leads to uncertainty as only mean gain is known and individual pixel gain is unknown. However, the L3CCD is efficient when the on-chip gains are tuned for lower values.

From the two-part research analysis, the direct measurement technique developed in this research, for Saturn's atmosphere demonstrates a possibility to derive the vertical structure up to 2[bar] pressure and for Venus's atmosphere at all altitudes as the available solar flux at this planet is 200 times more than that of Saturn. The research also produces internal field evaluation model that can be used for any planetary atmospheres.

7.2. Future Work and Recommendations

The master thesis research was focused on solving one central question that revolved around and led to a development of radiative transfer model for evaluating internal polarization field. The forward model has no validation possible, as there exist no similar models on internal polarization field. This internal field was used to evaluate the SNR for a nephelometer instrument for measuring in the low flux density planetary atmosphere. The research leads to further research questions on developing the instrument at sub-component level.

Forward model validations

The current thesis work paved a way for a new technique of measuring internal field in a planetary atmosphere using a nephelometer. The measurement technique discussed in this thesis exists on a test bench [46]. However, this measures the single scattered light, while the current research focuses on multiple scattered case as in a planetary atmosphere. The radiative transfer model developed in this research generates an internal field inside a cloud/haze. The existing polarization measurement is based on ground or space-based techniques and measures the polarization as a function of phase angle for Earth's atmosphere. There are future instruments planned such as, airborne experiments that have on-board polarization nephelometer to measure polarization data in Earth's atmosphere. These future concepts were discussed in Chapter 2. The forward model can be used to evaluate the internal field, where the airborne experiment shall be conducted. Following the experiment, a validation, and comparative analysis can be done with the model results and the actual measured experimental data.

Optical head:

The optical head chosen for the current research is from FlySPEX prototype experiment. This may not be suitable for measurement at Saturn's. The concern with the 1° × 1° field of view form FlySPEX proved to be challenging in terms of SNR (integration times). The FlySPEX optical head was optimized for Earth's atmosphere, the contamination levels in Saturn are different from Earth, and need a feasibility study in terms of understanding the tolerance levels for contamination on the optical head are required.

Spectrograph

From the theoretical specification, the major losses in the optical fiber for transmitting a signal occur at the connector coupling. Improving on the attenuation losses can be done by developing optical head, the optical fiber, and grating as one unit, which is the aim of improvement of the current FlySPEX prototype [66]. The investigation into spectrographs that have a larger shelf life and dynamic operating temperatures is recommended.

Studying internal field of Earth

The current model can be used to evaluate the internal field in Earth's atmosphere. Earth's atmosphere is a well known vertical structure, the current research model uses Monte-Carlo techniques to evaluate internal field, for Earth a more deterministic approach can be taken. In this case, the current model needs to be adapted for the atmosphere model with more defined data, and not rely on the indirect prediction of optical properties of the aerosol or molecular absorption or scattering coefficient as done in this research for Saturn's atmosphere.

Definitive-fit model

In order to make the current research model more efficient, validation of measured data is required. For which an experiment in a planetary atmosphere such as Venus is required, that could measure using our direct measurement technique. The forward model could also be adapted to measured optical thicknesses data in an atmosphere and produce a database of possible degree of linear polarization for this measured data, and act as a database, reusing the model for the definite-fit case and derive the microphysical properties such as complex refractive index and size distribution.

Bibliography

[1] Ground based aerosol measurement techniques, 1994. URL `https://www.gfdl.noaa.gov/wp-content/uploads/files/user_files/pag/lecture2008/lecture9.pdf`.

[2] Saturns presumed layer composition (picture courtesy), 2017. URL `https://stellersaturn.weebly.com/weather.html`. Last access: 1 February 2018.

[3] Tsi 3563 nephelometer schematic courtesy of tsi incorporated., 2017. URL `https://www.esrl.noaa.gov/gmd/aero/instrumentation/neph_desc.html`. Last access: 1 February 2018.

[4] Venus atmosphere pressure and temperature profiles., 2017. URL `http://www.datasync.com/~rsf1/vel/1918vpt.htm`. Last access: 19 November 2017.

[5] Stl-6303e ccd typical specifications, 2017. URL `https://www.virtualtelescope.eu/wordpress/wp-content/uploads/2012/10/STL6303_specs_7.12.11.pdf`. Last access: 1 February 2018.

[6] Qimaging retiga 4000r data sheet., 2017. URL `https://www.qimaging.com/products/datasheets/Retiga4000R.pdf`. Last access: 15 November 2017.

[7] Data from american society for testing and materials (astm) g-173-03 reference spectra., 2017. URL `http://rredc.nrel.gov/solar/spectra/am1.5/astmg173/astmg173.html`. Last access: 23 January 2017.

[8] C. A. Haniff A. G. Basden and C. D. Mackay. Photon counting strategies with low-light-level ccds. 38: 115–120, 2003.

[9] Ralph A Anl, D O E. Kahn. *Atmospheric Aerosol Properties and Climate Impacts*. Number June 2014. 2007. ISBN 9789401796484. doi: 10.1007/978-94-017-9649-1.

[10] Geografiska Annaler. On the Atmospheric Transmission of Sun Radiation and on Dust in the Air Author (s): Anders Ångström Published by : Wiley on behalf of Swedish Society for Anthropology and Geography Stable URL : http://www.jstor.org/stable/519399 ON THE ATMOSPHERIC TRANS. 11(1929):156–166, 2017.

[11] Gualtieri P. Barsanti L. *CCD Arrays, Cameras and displays, Second edition*. 2014. ISBN 9781439867334. doi: 10.1007/s007690000247.

[12] S. Bianchi, A. Ferrara, and C. Giovanardi. Monte Carlo Simulations of Dusty Spiral Galaxies: Extinction and Polarisation Properties. *ApJ*, 1, 1996. ISSN 1098-6596. doi: 10.1017/CBO9781107415324.004.

[13] R Black and C Pask. Optical Waveguides. *1st European Microwave Conference 1969*, 2:249–292, 1975. ISSN 15561534. doi: 10.1007/978-4-431-55148-5_3. URL `http://www.ncbi.nlm.nih.gov/pubmed/22330441`.

[14] N. Blind, E. Le Coarer, P. Kern, and S. Gousset. Spectrographs for astrophotonics. 25(22):719–726, 2017. URL `http://arxiv.org/abs/1707.01669`.

[15] Barry A. Bodhaine, Norman B. Wood, Ellsworth G. Dutton, and James R. Slusser. On Rayleigh optical depth calculations. *Journal of Atmospheric and Oceanic Technology*, 16(11 PART 2):1854–1861, 1999. ISSN 07390572. doi: 10.1175/1520-0426(1999)016<1854:ORODC>2.0.CO;2.

[16] Mike Bolte. Signal-to-Noise in Optical Astronomy CCDs: Some Details. *Techniques*, pages 4–19, 2008. URL `http://www.ucolick.org/{~}bolte/AY257/ay257.html`.

[17] Barry E Burke, James a Gregory, Michael Cooper, Andrew H Loomis, Douglas J Young, Thomas a Lind, Peter Doherty, Peter Daniels, Deborah J Landers, Joseph Ciampi, Kay F Johnson, and Peter W O Brien. CCD Imager Development for Astronomy. *Lincoln Laboratory Journal*, 16(2):393–412, 2007.

[18] F W. Taylor S B Calcutt, C A Nixon, P G J. Irwin, P L. Read P J C Smith, and T J Vellacott. Investigation of Saturn's atmosphere by Cassini. pages 204–213.

[19] CCD65. CCD65 Series Ceramic Pack Electron Multiplying CCD Sensor, 2004. URL `https://www.ast.cam.ac.uk/research/instrumentation.surveys.and.projects/lucky.imaging/l3ccd.technology`.

[20] S Chandrasekhar. Radiative Transfer, 1960.

[21] Space Flight-Space Systems Engineering course. Space systems engineering - lecture notes. Faculty of Aerospace Engineering TU Delft, March 2015-16.

[22] Olivier Daigle, Jean-Luc Gach, Christian Guillaume, Claude Carignan, Philippe Balard, and Olivier Boissin. L3CCD results in pure photon-counting mode. *SPIE Optical and Infrared Detectors for Astronomy*, 5499:219–227, 2004. ISSN 0277786X. doi: 10.1117/12.552411. URL `http://link.aip.org/link/?PSI/5499/219/1{&}Agg=doi`.

[23] J V Dave. Using Scattered Radiation Data. *Applied Optics*, 10(9):2035–2044, 1971.

[24] W.a. de Rooij and C. C. a. H. van der Stap. Expansion of Mie scattering matrices in generalized spherical functions. *Astron. Astrophys.*, 131:237–248, 1984. ISSN 0004-6361.

[25] A. Di Noia, O. P. Hasekamp, G. van Harten, J. H. H. Rietjens, J. M. Smit, F. Snik, J. S. Henzing, J. de Boer, C. U. Keller, and H. Volten. Use of neural networks in ground-based aerosol retrievals from multi-angle spectropolarimetric observations. *Atmospheric Measurement Techniques*, 8(1):281–299, 2015. doi: 10.5194/amt-8-281-2015. URL `https://www.atmos-meas-tech.net/8/281/2015/`.

[26] Environmental Chemistry Division. The whitehouse effect- shortwave radiative forcing of climate by anthropogenic aerosols: an overview. 27(3):359–382, 1996.

[27] Marilyn J. Dodge. Refractive properties of magnesium fluoride. *Appl. Opt.*, 23(12):1980–1985, Jun 1984. doi: 10.1364/AO.23.001980. URL `http://ao.osa.org/abstract.cfm?URI=ao-23-12-1980`.

[28] Gorachand Ghosh. Dispersion-equation coefficients for the refractive index and birefringence of calcite and quartz crystals. *Optics Communications*, 163(1):95 – 102, 1999. ISSN 0030-4018. doi: https://doi.org/10.1016/S0030-4018(99)00091-7. URL `http://www.sciencedirect.com/science/article/pii/S0030401899000917`.

[29] H. Grassl. Determination of aerosol size distribution from spectral attenuation measurements. *Applied optics*, 8(2):2534–2538, 1969. ISSN 0003-6935. doi: 10.1364/AO.8.000447. URL `http://www.ncbi.nlm.nih.gov/pubmed/18259449`.

[30] S. Guerlet, A. Spiga, M. Sylvestre, M. Indurain, T. Fouchet, J. Leconte, E. Millour, R. Wordsworth, M. Capderou, B. Bézard, and F. Forget. Global climate modeling of Saturn's atmosphere. Part I: Evaluation of the radiative transfer model. *Icarus*, 238:110–124, 2014. ISSN 10902643. doi: 10.1016/j.icarus.2014.05.010. URL `http://dx.doi.org/10.1016/j.icarus.2014.05.010`.

[31] J. E. Hansen and J. W. Hovenier. Interpretation of the polarization of venus. *J. Atmos. Sci.*, 31:1137–1160, 1974. doi: 10.1175/1520-0469(1974)031<1137:IOTPOV>2.0.CO;2.

[32] James E. Hansen and Larry D. Travis. Light scattering in planetary atmospheres. *Space Science Reviews*, 16(4):527–610, Oct 1974. ISSN 1572-9672. doi: 10.1007/BF00168069. URL `https://doi.org/10.1007/BF00168069`.

[33] Gerard Van Harten. Phd thesis : Spectropolarimetry for planetary exploration. 2014.

[34] C. van der Stap W.J. Wiscombe J.F. de Haan P.B. Bosma H.C. van de Hulst, W.A. de Rooij and adapted by D.M. Stam J.W. Hovenier, V.L. Dolman. Meerhoff mie program version 3.1.

[35] Benjamin M Herman, Samuel R Browning, and John A Reagan. *Determination of Aerosol Size Distributions from Lidar Measurements*, volume 28. 1971.

[36] J.W. Hovenier. Scattering matrix elements, Astronomical Institute. University of Amsterdam. 11:22–23.

[37] Carly J. A. Howett, Robert W. Carlson, Patrick G. J. Irwin, and Simon B. Calcutt. Optical constants of ammonium hydrosulfide ice and ammonia ice. *Journal of the Optical Society of America B*, 24(1):126—-136, 2007. ISSN 0740-3224. doi: 10.1364/JOSAB.24.000126.

[38] Michael D. King, Dale M. Byrne, Benjamin M. Herman, and John a. Reagan. Aerosol Size Distributions Obtained by Inversions of Spectral Optical Depth Measurements. *Journal of the Atmospheric Sciences*, 35:2153–2167, 1978. ISSN 0022-4928. doi: 10.1175/1520-0469(1978)035<2153:ASDOBI>2.0.CO;2.

[39] R. Knollenberg, L. Travis, M. Tomasko, P. Smith, B. Ragent, L. Esposito, D. Mccleese, J. Martonchik, and R. Beer. The clouds of Venus - A synthesis report. *Journal of Geophysical Research*, 85:8059–8081, 1980. ISSN 0148-0227. doi: 10.1029/JA085iA13p08059.

[40] R. G. Knollenberg and D. M. Hunten. The microphysics of the clouds of Venus: Results of the Pioneer Venus Particle Size Spectrometer Experiment. *Journal of Geophysical Research*, 85(A13):8039, 1980. ISSN 0148-0227. doi: 10.1029/JA085iA13p08039. URL `http://dx.doi.org/10.1029/JA085iA13p08039`.

[41] Michael Koppelman. *Society for Astronomical Sciences, pages = 107–110, title = Uncertainty Analysis in Photometric Observations, url = http://adsabs.harvard.edu/full/2005SASS...24..107K, year = 2005.*

[42] Paul R. Mahaffy, Mehdi Benna, Todd King, Daniel N. Harpold, Robert Arvey, Michael Barciniak, Mirl Bendt, Daniel Carrigan, Therese Errigo, Vincent Holmes, Christopher S. Johnson, James Kellogg, Patrick Kimvilakani, Matthew Lefavor, Jerome Hengemihle, Ferzan Jaeger, Eric Lyness, John Maurer, Anthony Melak, Felix Noreiga, Marvin Noriega, Kiran Patel, Benito D. Prats, Eric Raaen, Florence Tan, Edwin Weidner, Cynthia Gundersen, Steven Battel, Bruce P. Block, Ken Arnett, Ryan Miller, Curt Cooper, Charles Edmonson, and J. Thomas Nolan. The Neutral Mass Spectrometer on the Mars Atmospheric and Volatile Evolution Mission. *Space Science Reviews*, pages 49–73, 2014. doi: 10.1007/s11214-014-0091-1. URL `http://link.springer.com/article/10.1007/s11214-014-0091-1{#}`.

[43] J V Martonchik, G S Orton, and J F Appleby. Optical properties of NH3 ice from the far infrared to the near ultraviolet. *Applied optics*, 23(4):541, 1984. ISSN 0003-6935. doi: 10.1364/AO.23.000541.

[44] M. G. Moharam and T. K. Gaylord. Diffraction analysis of dielectric surface-relief gratings. *Journal of the Optical Society of America*, 72(10):1385, 1982. ISSN 0030-3941. doi: 10.1364/JOSA.72.001385. URL `https://www.osapublishing.org/abstract.cfm?URI=josa-72-10-1385`.

[45] O. Mousis, D. H. Atkinson, T. Spilker, E. Venkatapathy, J. Poncy, R. Frampton, A. Coustenis, K. Reh, J. P. Lebreton, L. N. Fletcher, R. Hueso, M. J. Amato, A. Colaprete, F. Ferri, D. Stam, P. Wurz, S. Atreya, S. Aslam, D. J. Banfield, S. Calcutt, G. Fischer, A. Holland, C. Keller, E. Kessler, M. Leese, P. Levacher, A. Morse, O. Muñoz, J. B. Renard, S. Sheridan, F. X. Schmider, F. Snik, J. H. Waite, M. Bird, T. Cavalié, M. Deleuil, J. Fortney, D. Gautier, T. Guillot, J. I. Lunine, B. Marty, C. Nixon, G. S. Orton, and A. Sánchez-Lavega. The Hera Saturn entry probe mission. *Planetary and Space Science*, 130:80–103, 2016. ISSN 00320633. doi: 10.1016/j.pss.2015.06.020.

[46] O. Muñoz and J. W. Hovenier. Laboratory measurements of single light scattering by ensembles of randomly oriented small irregular particles in air. A review. *Journal of Quantitative Spectroscopy and Radiative Transfer*, 112(11):1646–1657, 2011. ISSN 00224073. doi: 10.1016/j.jqsrt.2011.02.005.

[47] M.; Yamauchi T. Nakajima, T.; Tanaka. Retrieval of the optical properties of aerosols from aureole and extinction data. *Applied optics*, 8(2):447–53, 1969. ISSN 0003-6935. doi: 10.1364/AO.22.002951. URL `http://adsabs.harvard.edu/abs/1983ApOpt..22.2951N`.

[48] Christopher Palmer. Diffraction Grating Handbook. *Journal of the Optical Society of America*, 46(1): 20–23, 2005. ISSN 0030-3941. doi: 10.1364/JOSA.46.000050. URL `http://www.opticsinfobase.org/abstract.cfm?URI=josa-46-1-50`.

[49] K F Palmer and D Williams. Optical constants of sulfuric Acid; application to the clouds of Venus? *Applied optics*, 14(1):208–219, 1975. ISSN 0003-6935. doi: 10.1364/AO.14.000208. URL `http://dx.doi.org/10.1364/AO.14.000208`.

[50] Ray Bell David J. Burt Steve Bowring Simon Spencer Mike Hazelwood Ian Moody Neil Catlett Philip S. Heyes Paul Jerram, Peter J. Pool. The llccd: low-light imaging without the need for an intensifier, 2001. URL `https://doi.org/10.1117/12.426953`.

[51] Antonio Pereyra, Julio Tello, Erick Meza, William Cori, and Geof. Observatorio Astrońomico de la UNI - OAUNI: primera luz. 18(1):4–9, 2015.

[52] Santiago Pérez-Hoyos, José Francisco Sanz-Requena, Agustín Sánchez-Lavega, Patrick G.J. Irwin, and Andrew Smith. Saturn's tropospheric particles phase function and spatial distribution from Cassini ISS 2010-11 observations. *Icarus*, 277:1–18, 2016. ISSN 10902643. doi: 10.1016/j.icarus.2016.04.022.

[53] L. W. Pinkley and D. Williams. The infrared optical constants of sulfuric acid at 250 K*. *Journal of the Optical Society of America*, 66(2):122–124, 1976.

[54] B Ragent and J. E. Blamont. Preliminary Results of the Pioneer Venus Nephelometer Experiment. *Science*, 203(4382):790–792, 1979. ISSN 00368075. URL `http://www.sciencemag.org/content/203/4382/790.short`.

[55] B. Ragent, C. A. Privette, P. Avrin, J. G. Waring, C. E. Carlston, T. C D Knight, and J. P. Martin. Galileo Probe Nephelometer experiment. *Space Science Reviews*, 60(1-4):179–201, 1992. ISSN 00386308. doi: 10.1007/BF00216854.

[56] B Ragent, D S Colburn, P Avrin, and K a Rages. Results of the Galileo probe nephelometer experiment. *Science (New York, N.Y.)*, 272(5263):854–856, 1996. ISSN 0036-8075. doi: 10.1126/science.272.5263.854.

[57] Boris Ragent, Thomas Wong, Jacques E. Blamont, Alan J. Eskovitz, Laurence N. Harnett, and Arpad Pallai. Pioneer Venus Sounder And Small Probes Nephelometer Instrument. *IEEE Transactions on Geoscience and Remote Sensing*, GE-18(1):111–117, 1980. ISSN 0196-2892. doi: 10.1109/TGRS.1980.350292.

[58] Jessica C. Ramella-Roman, Scott A. Prahl, and Steve L. Jacques. Three Monte Carlo programs of polarized light transport into scattering media: part I. *Optics Express*, 13(12):4420, 2005. ISSN 1094-4087. doi: 10.1364/OPEX.13.004420. URL `https://www.osapublishing.org/oe/abstract.cfm?uri=oe-13-12-4420`.

[59] R. RODIER, R. THUSS, and J. TERHUNE. Parachute design for Galileo Jupiter entry probe. *7th Aerodynamic Decelerator and Balloon Technology Conference*, 1981. doi: 10.2514/6.1981-1951. URL `http://arc.aiaa.org/doi/10.2514/6.1981-1951`.

[60] M. Semel, J.-F. Donati, and D. E. Rees. Zeeman-Doppler imaging of active stars. 3: Instrumental and technical considerations. *Astronomy and Astrophysics*, 278:231–237, 1993. ISSN 0004-6361. URL `http://adsabs.harvard.edu/abs/1993A{%}26A...278..231S`.

[61] K. Serkowski. Optical polarimeters in astronomy, 1977. URL `TheUniversityofArizonaPres,Tucson,Arizona,1974`.

[62] G E Shaw. Inversion of optical scattering and spectral extinction measurements to recover aerosol size spectra. *Applied optics*, 18(7):988–993, 1979. ISSN 0003-6935. doi: 10.1364/AO.18.000988. URL `http://www.ncbi.nlm.nih.gov/pubmed/20208864`.

[63] Frans Snik and Christoph U. Keller. Astronomical polarimetry: Polarized views of stars and planets. *Planets, Stars and Stellar Systems Volume 2: Astronomical Techniques, Software, and Data*, pages 175–221, 2013. doi: 10.1007/978-94-007-5618-2_4.

[64] Frans Snik, Julia Craven-Jones, Michael Escuti, Silvano Fineschi, David Harrington, Antonello De Martino, Dimitri Mawet, Jérôme Riedi, and J. Scott Tyo. An overview of polarimetric sensing techniques and technology with applications to different research fields. *Spie*, 9099:90990B, 2014. ISSN 1996756X. doi: 10.1117/12.2053245. URL `http://proceedings.spiedigitallibrary.org/proceeding.aspx?doi=10.1117/12.2053245`.

[65] Frans Snik, Julia Craven-Jones, Michael Escuti, Silvano Fineschi, David Harrington, Antonello De Martino, Dimitri Mawet, Jérôme Riedi, and J Scott Tyo. An overview of polarimetric sensing techniques and technology with applications to different research fields. *Spie*, 9099:90990B, 2014. ISSN 1996756X. doi: 10.1117/12.2053245. URL `http://proceedings.spiedigitallibrary.org/proceeding.aspx?doi=10.1117/12.2053245`.

[66] Frans Snik, Christoph U. Keller, Merijn Wijnen, Hubert Peters, Roy Derks, and Edwin Smulders. FlySPEX: a flexible multi-angle spectropolarimetric sensing system. 985308(May 2016):985308, 2016. ISSN 1996756X. doi: 10.1117/12.2223824. URL `http://proceedings.spiedigitallibrary.org/proceeding.aspx?doi=10.1117/12.2223824`.

[67] D. M. Stam, J. W. Hovenier, and L. B. F. M. Waters. Using polarimetry to detect and characterize Jupiter-like extrasolar planets. *Astronomy & Astrophysics*, 428(2):663–672, 2004. ISSN 0004-6361. doi: 10.1051/0004-6361:20041578. URL `http://www.aanda.org/10.1051/0004-6361:20041578`.

[68] Fredric W. Taylor. Venus before Venus Express. *Planetary and Space Science*, 54(13-14):1249–1262, 2006. ISSN 00320633. doi: 10.1016/j.pss.2006.04.031.

[69] H B Twomey, S .Howell. Some aspects of the optical estimation of microstructure in fog and cloud. *Applied Optics*, 6(12):2125–2131, 1967. ISSN 0003-6935. doi: 10.1364/AO.6.002125.

[70] S. Twomey. On the Numerical Solution of Fredholm Integral Equations of the First Kind by the Inversion of the Linear System Produced by Quadrature. *Journal of the ACM*, 10(1):97–101, 1963. ISSN 00045411. doi: 10.1145/321150.321157.

[71] G. Van Harten, J. De Boer, J. H H Rietjens, A. Di Noia, F. Snik, H. Volten, J. M. Smit, O. P. Hasekamp, J. S. Henzing, and C. U. Keller. Atmospheric aerosol characterization with a ground-based SPEX spectropolarimetric instrument. *Atmospheric Measurement Techniques*, 7(12):4341–4351, 2014. ISSN 18678548. doi: 10.5194/amt-7-4341-2014.

[72] Stephen G Warren and Stephen G Warren. Optical constants of ice from the ultraviolet to the microwave. *Applied Optics*, 1984.

[73] R A West, K H Baines, A J Friedson, D Banfield, B Ragent, and F W Taylor. Jovian Clouds and Haze. *Jupiter: The Planet, Satellites and Magnetosphere*, (1997):79–104, 2004.

[74] W. J. Wiscombe and G. W. Grams. The Backscattered Fraction in two-stream Approximations, 1976. ISSN 0022-4928. URL `http://journals.ametsoc.org/doi/abs/10.1175/1520-0469{%}281976{%}29033{%}3C2440{%}3ATBFITS{%}3E2.0.CO{%}3B2`.

[75] Ford WK. Digital imaging techniques, ann. rev. astron. astrophys. (17):189–212, 1979.

[76] R. F. Wolffenbuttel. MEMS-based optical mini- and microspectrometers for the visible and infrared spectral range. *Journal of Micromechanics and Microengineering*, 15(7), 2005. ISSN 09601317. doi: 10.1088/0960-1317/15/7/021.

[77] G Yamamoto and M Tanaka. Determination of aerosol size distribution from spectral attenuation measurements. *Applied optics*, 8(2):447–53, 1969. ISSN 0003-6935. doi: 10.1364/AO.8.000447. URL `http://www.ncbi.nlm.nih.gov/pubmed/18259449`.